CONSTRAINTS ON ERUPTION DYNAMICS, MOUNT ST. HELENS, WA, 2004-2008

by

ANDREW DANIEL SCHNEIDER

A THESIS

Presented to the Department of Geological Sciences
and the Graduate School of the University of Oregon
in partial fulfillment of the requirements
for the degree of
Master of Science

September 2009

"Constraints on Eruption Dynamics, Mount St. Helens, WA, 2004-2008," a thesis prepared by Andrew Daniel Schneider in partial fulfillment of the requirements for the Master of Science degree in the Department of Geological Sciences. This thesis has been approved and accepted by:

_____

Alan Rempel, Chair of the Examining Committee

25 August 2009
Date

Committee in Charge: Dr. Alan Rempel, Chair
                         Dr. Katharine Cashman
                         Dr. David Schmidt

Accepted by:

_____

Dean of the Graduate School

An Abstract of the Thesis of

Andrew Daniel Schneider   for the degree of   Master of Science

in the Department of Geological Sciences   to be taken   September 2009

Title: CONSTRAINTS ON ERUPTION DYNAMICS, MOUNT ST. HELENS, WA,

2004-2008

Approved: _____
Alan Rempel

Different models have been proposed for the "drumbeat" earthquakes that accompanied recent eruptive behavior at Mount St. Helens. Debate continues as to whether seismicity is related to brittle failure during the extrusion of solid dacite spines or is the result of hydrothermal fluids interacting with a crack buried in the volcanic edifice. My model predictions of steady-state conduit flow confirm the strong control that degassing exerts on eruptive behavior. I discuss the necessary role of degassing for extruded material to attain the high density (low vesicularity) of the observed spine material and discuss the implications for generating seismicity. A brittle-failure source of seismicity requires that the gouge elastic properties accommodate some strain, since the magma compressibility in the upper conduit is too low to do so on its own. I also report

on a novel method for generating high-resolution digital elevation models of fault surface textures.

CURRICULUM VITAE

NAME OF AUTHOR: Andrew Daniel Schneider

PLACE OF BIRTH: Springfield, MA, USA

DATE OF BIRTH: September 8, 1982

GRADUATE AND UNDERGRADUATE SCHOOLS ATTENDED:

    University of Oregon, Eugene, OR
    Amherst College, Amherst, MA

DEGREES AWARDED:

    Master of Science, Geology, 2009, University of Oregon
    Bachelor of Arts, Geology, 2004, Amherst College

AREAS OF SPECIAL INTEREST:

    Numerical Modeling of Geophysical Processes
    Conduit Dynamics of Silicic Systems

PROFESSIONAL EXPERIENCE:

    Research Assistant, Department of Geological Sciences, University of Oregon, Eugene, OR, 2008-2009

    Graduate Teaching Fellow, Department of Geological Sciences, University of Oregon, Eugene, OR, 2007-2009

    Investigator, Civilian Complaint Review Board, Office of the Mayor, New York, NY, 2005-2007

    Teaching Assistant, Department of Geology, Amherst College, Amherst, MA, 2002

ACKNOWLEDGMENTS

There are many people to whom I am grateful. John Donovan was very helpful in providing technical assistance while using the SEM and MeX software. I am especially grateful to John Pallister of the USGS for his support in planning and leading field work during the summer of 2008. UCORE Fellow Naomi Mecham provided considerable assistance during the summer of 2009 with generating fault surface DEMs.

I am incredibly grateful to my friends both in and out of the department, and in and out of Eugene for their ongoing support and love. There are too many of you all to name but I want to specifically acknowledge Max, Nick, Alicia, Trish, Amanda, Laura, Ashley, Steph, Sidney, Fraser and Shannon for their friendship over the last two years. I am also incredibly grateful for the support of my family throughout both this project and all of my endeavors, past, present and future.

I would like to thank David for sparking my interest in geophysics, a relatively novel concept to a liberal arts student. I owe much recognition to Kathy for introducing me to the world of physical volcanology and for her overall enthusiasm for science. Finally, I am indebted to Alan, whose guidance allowed me to develop my appreciation for geophysical processes and numerical modeling. Without his patience and insight much of this project would not have been possible. I am also grateful for his financial support through research assistanceships and for the ability to attend conferences.

TABLE OF CONTENTS

LIST OF FIGURES

LIST OF TABLES

CHAPTER I

INTRODUCTION

Renewed eruptive activity at Mount St. Helens from 2004-2008 was characterized by extrusion of a series of solid spines ~200 m in diameter and several hundred meters long, mantled in fault gouge (Scott et al., 2009; Cashman et al., 2009). Petrologic investigations indicate that magma solidified at a depth of about 500 m (Cashman et al., 2009). A nearly constant linear extrusion rate on the order of 10s of μm/s from December 2004 to December 2005 (Vallance et al., 2009) implies the time for total slip of several hundred meters is on the order of about 13 weeks. The cylindrical bounding fault between the plug and the conduit wall is well constrained spatially and temporally and offers a unique opportunity to study the mechanics involved.

Repetitive "drumbeat" earthquakes were detected while the spine extrusion was ongoing (Moran et al., 2009). A debate ensued as to whether the source of seismicity was linked to seismogenic slip during spine extrusion (Iverson et al., 2006; Harrington and Brodsky, 2007; Iverson, 2009) or was unrelated to extrusion and instead caused by the flux of gases through a venting crack (Waite et al., 2008; Matoza et al. 2009). The fundamental question about the seismic source guided much of the work in this project. Chapter 2 discusses the details of the eruption, fully introduces prior models of the

seismic source, and presents my own modeling results. Chapter 3 introduces the results

of smaller scale projects, such as isotopic analysis, that add pieces of information relevant

to the larger project. Chapter 4 introduces the dynamics of silicic systems in general, in

which the role of volatiles are highly important. The second section of Chapter 4

describes prior numeric models for conduit dynamics in silicic volcanoes and provides

the necessary background before introducing the conduit model I established. The model

was designed to constrain magma properties from the chamber to the base of the plug

because the thermo-mechanical conditions at the plug base ultimately control extrusive

behavior. Chapter 5 presents the results of sensitivity tests conducted with the model and

discusses these results and the implications for the eruptive style and the generation of

seismicity. Chapter 6 contains the concluding remarks.

CHAPTER II

BACKGROUND

Background of the 2004-2008 eruption

Mount St. Helens has existed as a broad eruptive center since at least 300,000 years ago, characterized by dacitic lava domes surrounded by pyroclastic and volcanoclastic material (Clynne et al., 2009; Scott et al., 2009). About 2,500 years ago the formation of a more prominent cone coincided with the eruption of basalt and andesite between eruptions of dacite. This style of growth persisted until the 18th century, after which eruptions continued but did not change the shape of Mount St. Helens. Precursory activity to the May 1980 eruption began in mid-March of that year, first with seismic swarms, then increased frequency of seismicity and steam explosions, and finally intrusion of a cryptodome, as evidenced by the bulging north flank of the volcano. Activity culminated on May 18 of that year when the north flank failed, triggering a debris avalanche and decompression of the magmatic system, which itself generated a lateral explosion and pyroclastic density currents. Five smaller explosions that summer were followed by approximately six years of intermittent episodes of dome growth, producing an edifice 270 m high (the 1980-1986 dome). Activity at Mount St. Helens between 1986 and mid-2004 was minimal, but included deep earthquakes and small explosions that ejected ash and occasionally blocks of volcanic material. There was no deformation detected at the surface to suggest an increase in either the volume or pressure of the magma chamber during these 18 years.

Precursory activity to the 2004 eruption began on September 23 with the detection of shallow earthquakes with magnitudes of duration (M_d) < 2.0 (Scott et al., 2009). After about a week of this behavior, an increase in both the frequency and magnitude (M_d < 3.0) of seismicity coincided with the visual detection of a welt of uplifted glacier south of the 1980-1986 dome that was being displaced vertically at a rate of meters per day. The first explosion occurred on October 1, an event that produced a 2 km-high ash cloud and coincided with M_d ~ 4.0 earthquakes. Helicopter-mounted infrared detecting equipment recorded a maximum temperature of about 160 °C near the welt that same day. Explosions continued over the next few days but ended on October 5, coincident with a permanent decrease in seismic frequency and magnitude. Infrared measurements on October 10 recorded maximum temperatures of 270 °C. Total uplift of the welt resulted in a maximum cumulative volume change measurement on that day of about $10^7 \, m^3$. October 11 marked the first sight of lava - a 30 m-high dacite fin, later known as spine 1. Infrared measurements recorded its maximum surface temperature at 560 °C, with a maximum of 730 °C detected in cracks on its surface. At around this time seismicity settled into a steady "drumbeat" pattern with small (Md < 1.0) events occurring at a rate of about 1 per minute (Moran et al., 2009). Spine 1 continued to extrude nearly vertically for the next four days, reaching a maximum height of about 100 m before growth stopped and spine 2 emerged (Schilling et al., 2009). Spine 2 extruded at a similar rate for about nine days (~200 m) at a lesser angle to the crater floor than spine 1, leading to a southward component of motion. Spine 3 emerged in late October and grew

continuously for nearly 2 months. Spine 3 also extruded sub-vertically and reached a length of ~500 m before colliding with the south crater wall, forming substantial cracks at its base and apparently decoupling from the vent before spine 4 emerged in early January 2005. Spine 4 had a trajectory similar to that of spine 3, although it extruded for more than 3 months before stopping at the crater wall. The extrusion of spine 4 pushed spine 3 to the east, which accelerated disintegration of that spine. Spine 5 actively grew from mid-April to mid-July, though at a steeper angle (~70°) to the crater floor than the previous two spines (Poland et al., 2009). At the end of its growth its summit stood 450 m above the crater floor. Spines 3-5 are grouped as the "whaleback" spines. Their diameters were typically between 150-200 m (Vallance et al., 2009) and their surfaces coated in several meters of powdery gouge owing to crystallization at depth (~500 m) and abrasion of the plug with the conduit wall during its final ascent to the surface (Cashman et al., 2009). During late July motion of spine 5 ceased and it began to rapidly disintegrate. The growth of spine 6 occurred from August to October 2005 and represented a change in extrusive behavior. Spine 6 extruded to the west, marking a change from the southward extrusion of spines 1-5. Furthermore, the form of spine 6 was more dome-like and its dimensions were roughly equant (Vallance et al., 2009). Spine 7 emerged in October 2005 and also extruded to the west, although with a more elongate form characteristic of earlier spines. Spine 7 thrusted over spine 6 and continued to grow until January 2008 when extrusion ceased, seismicity greatly diminished and there was no discernible ground deformation (Scott et al., 2009). Growth of spine 7 through 2006

and 2007 was generally characterized by it broadening and the growth rate was an order of magnitude less than the steady rate of extrusion of 1.0-2.0 m^3/s that occurred during 2005.

<div align="center">Proposed sources of seismicity</div>

Several researchers have worked to constrain the source of seismicity that accompanied renewed eruptive activity. Iverson et al. (2006) introduced the SPASM (Seismogenic Plug of Ascending Solidifying Magma) model, which was explained in more detail by Iverson (2009). This model draws from the earthquake literature and accounts for dome growth by repetitive stick-slip events. Reasonable values for magma, conduit and dome properties result in stick intervals consistent with drumbeat earthquake periods. Analysis of the seismic record by Harrington and Brodsky (2007) is also consistent with SPASM in that they find similar scaling between signal properties of the drumbeat earthquakes and tectonic earthquakes. On the other hand, Waite et al. (2008) and Matoza et al. (2009) measured seismic and acoustic signals, respectively, and found dilatational first motions that are inconsistent with failure of a vertical strike-slip fault and are instead best modeled with a resonating, fluid-filled crack buried in a shallow structure beneath the crater floor.

SPASM solves for the short term (tens to hundreds of seconds) evolution of magma pressure at the base of the plug and the velocity and displacement of the plug. The magma ascends the conduit at a constant rate, and applies a driving force (magma pressure times the conduit cross sectional area) to the base of the plug (Figure 2.1).
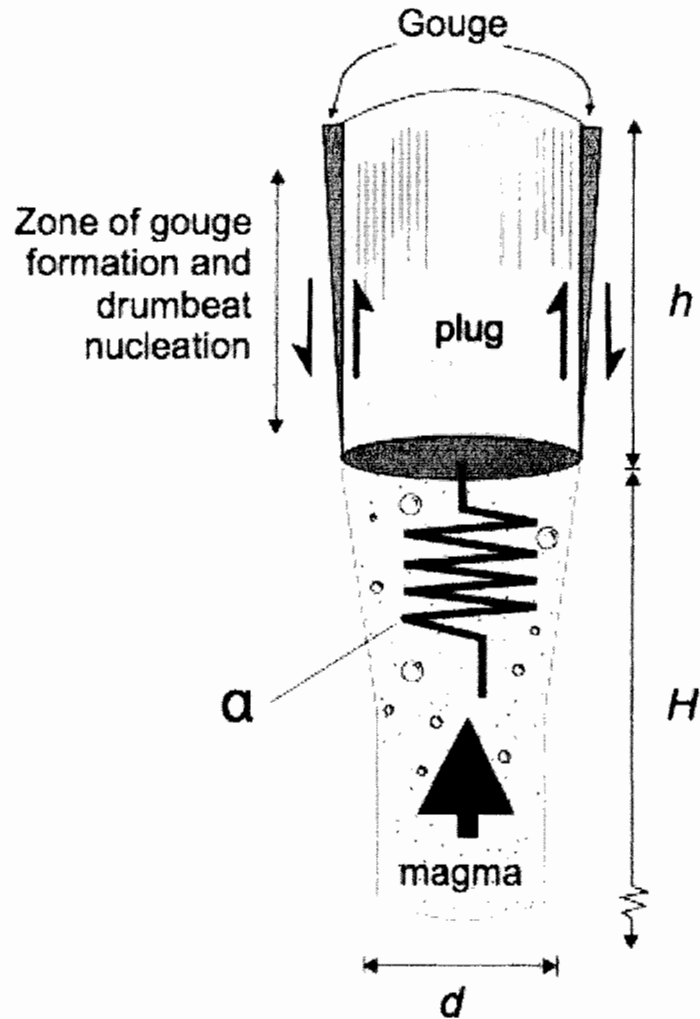
Figure 2.1. The layout of the model of Iverson et al. (2006) and Iverson (2009). Those models predict that drumbeat earthquakes nucleate along the plug-conduit wall margin during spine extrusion. Figure from Moore et al. (2009).

Elastic energy is stored in the magma in the form of compressible bubbles and, to a lesser extent, the conduit wall rock. In quiescent periods, the driving force at the base of the plug is resisted, or balanced, by the weight of the overlying plug and the friction generated along the conduit boundary. The nature of the boundary is constrained by field observations, which documented meter-scale-thick layer of gouge mantling the extruded spines. Iverson et al. (2006) and Iverson (2009) assign a rate-weakening rheology to the gouge (in which the frictional resistance diminishes with increasing slip rate) using laboratory experiments by Moore et al. (2009), which were conducted at room temperature and under low confining stresses. Using reasonable values for magma and plug parameters, the SPASM model shows that constant magma flux increases pressure at the base of the stationary plug until the driving force exceeds the weight of the plug plus the frictional resistance. The plug begins to slip and accelerate, and frictional resistance decreases according to the law governing gouge rheology. The magma expands into the volume generated by the extruding plug and magma pressure decreases. Plug motion ceases when the driving force of the magma is again balanced by the weight of the plug plus friction. This stick-slip cycle repeats with constant stick periods and slip displacements for a given magma ascent rate. For stick times of ~100 s, the period of the drumbeat earthquakes, the plug slips 5 mm per slip event, reaching a maximum extrusion velocity of ~1.5 mm/s. The slip events correspond to force drops of 7.0×10^7 N (pressure drops of 2 kPa) and a time-averaged extrusion rate of 6.7×10^{-5} m/s, consistent with the roughly constant volumetric extrusion rate of 2 m^3/s measured by Schilling et al. (2009).

Waite et al. (2008) recorded seismic activity during summer 2005 using an array of 19 seismic stations. They interpreted the hybrid events as two discrete waves - a higher frequency long period (LP) event followed by a lower frequency very long period (VLP) event lasting 5 to tens of seconds. In this framework, the drumbeat events are represented only by the LP events. They argue that the first motions are inconsistent with stick-slip, or double-couple, failure. Such failure would generate a mix of compressional and dilatational first motions distributed at station locations. Waite et al. (2008) observe a dilatational first motion in addition to a vertical single force and detect very little shear wave energy. They detect similar waveforms relating to the VLP source and attribute the source mechanism for both the LP and VLP events to a net volume decrease partially on the basis of the dilatational first motions. Moreover, the principal eigenvalues of the LP moment tensor are consistent with a steam-filled tensile crack in a Poisson solid (defined by a Poisson ratio of 0.25) and those of the VLP source are consistent with a magma-filled tensile crack, also in a Poisson solid.

Waite et al. (2008) constrain the source of the LP and VLP events using a 3-D model of the crater region created from aerial photographs and topographic maps, respectively. They impose a simple density and velocity structure wherein the values of both are lower near the surface and near the volcanic edifice. The inversion locates the LP source directly beneath the emerging spine (during July 2005) at a depth of about 250 m below the base of the spine. They do not determine a formal uncertainty but note that a

reasonable uncertainty would be about ±100 m in the vertical coordinate. They conclude that the source of the VLP events is about 300 m directly below the 1980's dome.

Using these findings, Waite et al. (2008) minimized the error between their modeled and observed results with an LP source as a crack shallowly dipping to the NNW that undergoes volume changes of between 600 and 770 m^3 during collapse events (Figure 2.2). These volume changes produced the observed dilatational first motions; the resulting motion of the overlying dome is responsible for the vertical force.

Waite et al. (2008) suggest the source of VLP events is a more complicated structure, requiring a sill dipping to the SW intersected approximately perpendicularly by a dike of similar dimensions. In their model, the dike and sill are out of phase; that is, while one is inflating the other is deflating, but net volume change during VLP events is a decrease of about 1000 m^3. The dilatational motion detected they attribute to this volume change and the single vertical force they attribute to the mass advection of magma.

Matoza et al. (2009) perform a similar analysis using measurements of acoustic energy taken from 13.4 km to the northwest of the crater. Their infrasound record the LP events, as defined by Waite et al. (2008), but lack the long duration VLP events. They also determined dilatational source mechanisms. Matoza et al. (2009) were able to match the observed acoustic onset and a very weak or absent coda using simplified model structures. For example, they tested the effect of topography, an isotropic moment tensor, by imposing a low velocity layer for the upper ~500 m instead of a homogenous velocity structure. They conclude that the source structure is too complex to model but can be
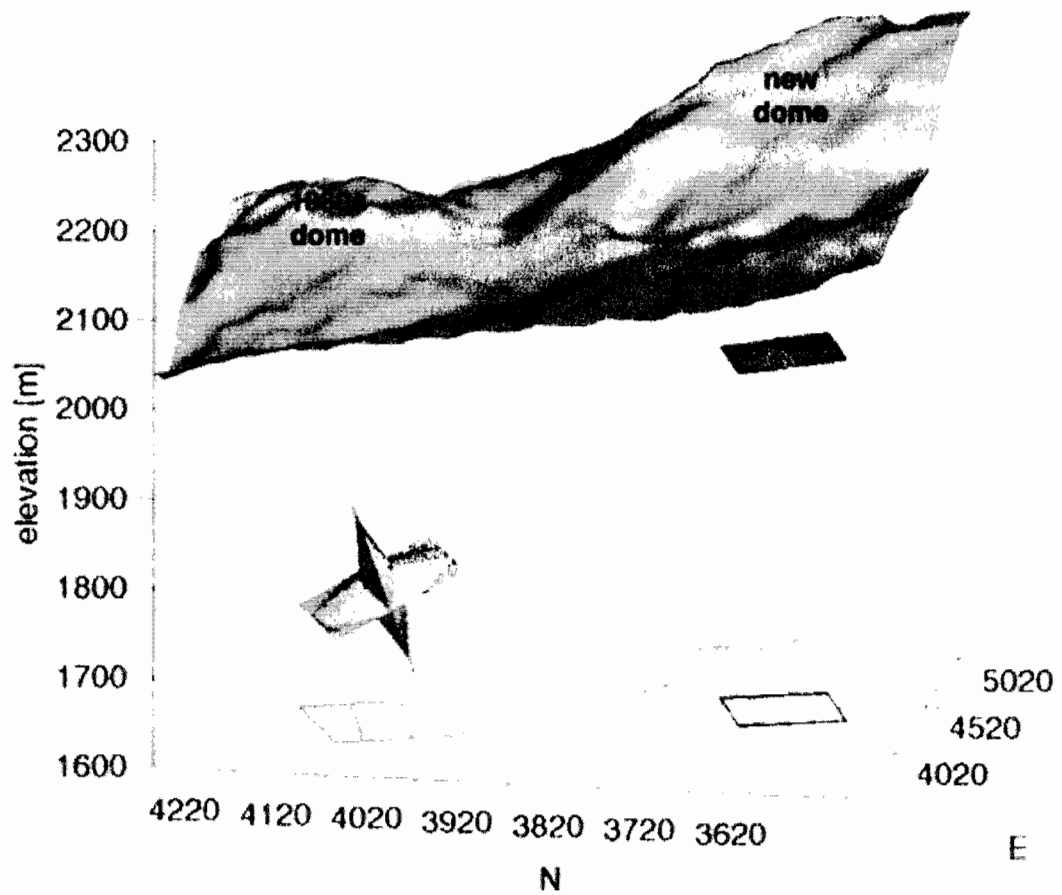
Figure 2.2. The layout of the model of Waite et al. (2008). The subhorizontal crack below the new dome to the right is their proposed source of drumbeat seismicity. Figure from Waite et al. (2008).

approximated as a 200 m-deep, sub-horizontal crack that couples predominately to the elastic medium, but at one tip vents into a highly porous and permeable zone of fractured rock and/or ice. Their understanding of the repetition is similar to that of Waite et al. (2008) - pressure inside a steam/water-filled crack increases over time until a threshold is exceeded and the "valve" regulating escape is opened. The crack collapses under the volume change and initiates the broadband seismic onset. The sudden flux of gas into a saturated pathway that is acoustically permeable to infrasonic wavelengths produces the infrasonic signal. Meanwhile, the resonant response of the fluid is detected seismically as the long duration coda, but such deformation is poorly transmitted to the atmosphere through the overlying elastic medium, resulting in the weak or absent long duration acoustic signal.

Harrington and Brodsky (2007) reexamined the source of the hybrid earthquakes detected at Mount St. Helens during spine extrusion using an array of 5 seismic stations, 3 of which were also used by Waite et al (2008). Hybrid earthquakes have a high-frequency onset followed by a low-frequency coda that lasts orders of magnitude longer than codas for tectonic earthquakes of equivalent magnitudes. This type of earthquake has been observed in other volcanic environments. Harrington and Brodsky (2007) propose a brittle failure event as the seismic source based on the scaling of station distance to coda duration and moment magnitude to corner frequency. Because the earthquakes are generally known to occur near the vent, they attribute them to stick-slip extrusion of the spines, consistent with the SPASM model.

Prior work on hybrid earthquakes has suggested that the high-frequency event initiates resonance within a fluid-filled conduit, triggering the low-frequency and long duration coda (Neuberg et al., 2006), but also that the same source is responsible for both events on the basis of continuity between the high- and low-frequency signals (Neuberg et al., 2000). Harrington and Brodsky (2007) use seismic data collected from stations positioned between 110 m and 6 km from the vent. They define the duration of the events as the length of time from onset until amplitude decays to e^{-1} of the peak amplitude, and find a linear relationship between distance of the station to the vent and the event duration. They then extrapolate this trend to the vent and constrain the duration of events there at 0.9 s. They argue that, had the seismicity been the result of a resonating fluid, the duration of the codas should not be much greater than 0.8 s at any of the seismic stations. They note a duration of 25 s at a distance of 6 km, and propose that a complicated path through loosely consolidated volcanic material in the upper edifice is the cause of the long durations.

Moreover, they find that the logarithm of moment magnitude scales to the corner frequency with a slope of -3.3 ± 0.3, which is consistent with the model of a standard 2-D fault with constant stress drops, in which case moment magnitude scales with corner frequency taken to the power -3. The corner frequencies observed, however, are roughly an order of magnitude smaller than those detected for tectonic earthquakes of comparable magnitudes. Harrington and Brodsky (2007) attribute this to a low rupture velocity,

which they constrain at approximately 650 m/s (about 1/4 that of tectonic faults) based on average S-velocity.

This section serves to illustrate that there are compelling arguments for both stick-slip spine extrusion generating the drumbeat earthquakes and for the resonance in a fluid-filled cavity at depth. This was a fundamental question throughout the work presented in this thesis. The modeling extensions made to the SPASM model (discussed in section 2.3) and the conduit modeling (discussed in section 4.3 and in chapter 5) were guided by this problem and sought new ways of answering it.

<u>Extensions to the SPASM model</u>

The SPASM model is easily reproduced using MATLAB, which allowed me to investigate the system response to conditions different from those considered by the original authors. One of the parameters tested by Iverson et al. (2006) was the volumetric rate of erosion from the top of the spine. They used a nominal value of 2.0 m^3/s, which matches the set volumetric rate of accretion of magma to the base of the plug, in which case the plug mass remains constant. They used a range of values for the erosion rate of the same order as the accretion rate and found no discernible difference in extrusive behavior and, therefore, a typical model run considered plug mass as constant. In cases where erosion exceeded basal accretion, the plug mass gradually decreased over time. However, the maximum erosion rate considered was 4000 kg/s, which, over a model run of a few hundred seconds, corresponds to change in mass of order 10^6 kg, whereas a typical mass value for the entire plug was of order 10^{10} kg. Because the relative amount

of mass lost was small, and because it occurred gradually, there was little discernible change in modeled behavior. Generally, the model parameters such as magma pressure and volume would evolve to reflect the change in mass, but those changes were also small and gradual.

During the 2004-2008 eruption the spines experienced larger scale collapse events that involved substantial volumes of material (10^4 - 10^5 m^3; Scott et al., 2009). The largest events occurred on spine 5, likely owing to its steep extrusion angle and resulting prominent height. Smaller rockfall events involving less than 10^4 m^3 also occurred frequently throughout spine extrusion. The large rockfall events were simulated by imposing an instantaneous change in mass consistent with the volume losses reported by Scott et al. (2006) and the dome rock density value used in SPASM (2400 kg/m^3). Rockfalls involving 10^4 m^3 and 10^5 m^3 represents decreases in mass by 2.4 x 10^7 kg and 2.4 x10^8 kg, or 0.07% and 0.7% of the original plug mass, respectively. The results from modeling the lower limit case of 10^4 m^3 are shown in Figures 2.3 and 2.4. Figure 2.3 shows the evolution of pressure with a simulated rockfall occurring at t = 400 s, which disrupted steady state SPASM behavior. A pressure drop of ~20 kPa occurs, representing roughly 10 times the amount of pressure lost during a slip event in the steady state. The magma repressurizes at a rate similar to that during stick periods in the steady state, until the critical pressure needed to initiate slip is once again attained. Because of the change in mass, this critical value is less than the critical pressure prior to the drop in mass (by about 10 kPa). Once the magma repressurizes to the new critical pressure after ~750 s,
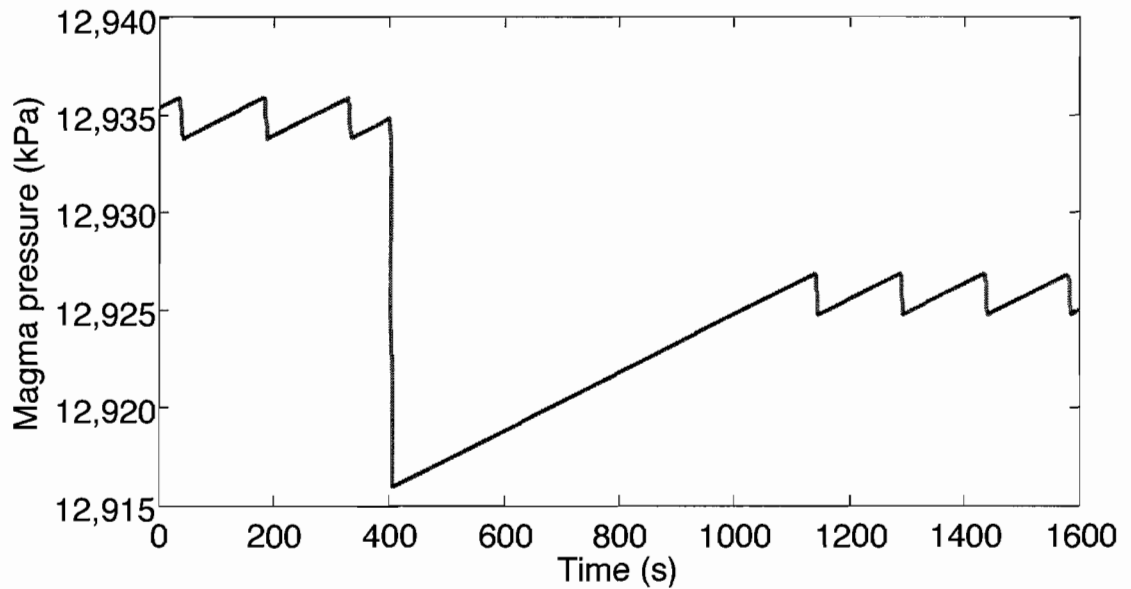
Figure 2.3. Magma pressure over time with a simulated rockfall event with a size of 10^4 m^3 occurring at $t = 400$ s. Steady state behavior occurring from $t = 0$ to $t = 400$ s is disrupted. A prominent pressure drop of ~20 kPa occurs, and a repressurization period of ~750 s follows. At $t \approx 1150$ s steady state behavior resumes, with no apparent change in stick interval or pressure drop per slip event.
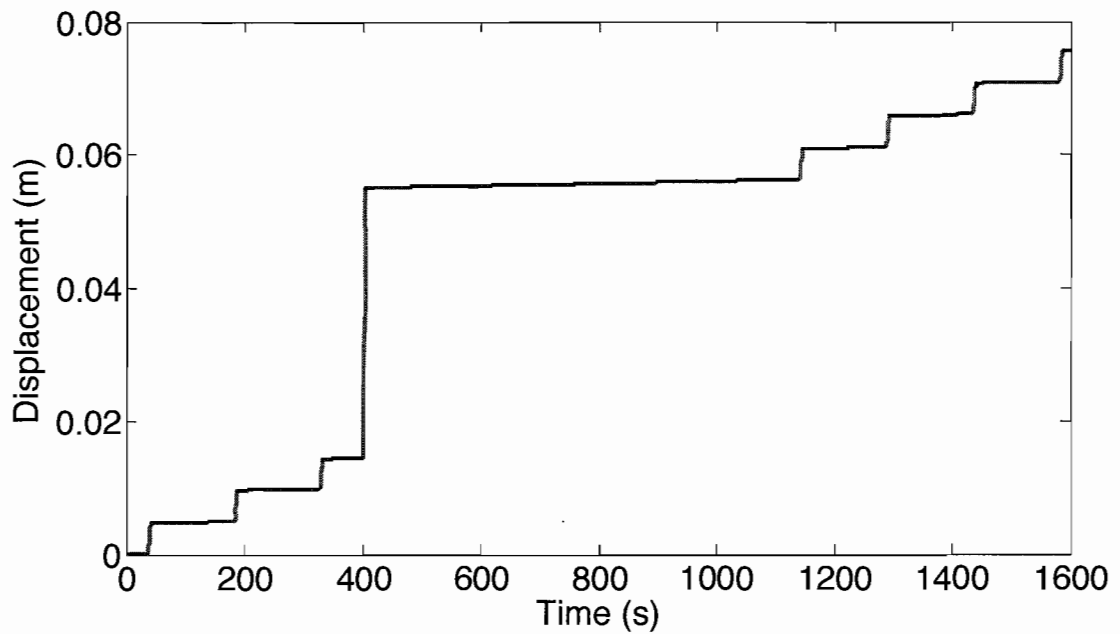
Figure 2.4. Spine displacement over time with a simulated rockfall event with a size of 10^4 m^3 occurring at $t = 400$ s (same as that in Figure 1). Steady state behavior occurring from $t = 0$ to $t = 400$ s is disrupted. A prominent slip of ~4 cm occurs, and a prolonged stick period of ~750 s follows. At $t \approx 1150$ s steady state behavior resumes, with no apparent change in slip distance per event of stick interval.

steady state behavior resumes with no change in slip recurrence interval. Therefore, from the change in magma pressure, the only perceivable deviation from steady state behavior is the lack of slip events (earthquakes) during the repressurization period.

Figure 2.4 shows spine displacement from the same model run. Steady slip of ~5 mm occurs every ~120 s until the drop in mass at t =400 s, at which point the spine suddenly slips ~4 cm. An extended stick time of ~750 s follows, coincident with magma repressurization. Slips events then resume with no apparent change in slip distance per event. From the analysis of spine displacement, the only detectable change in behavior is the slip of several cm. The expected change in the seismic record would therefore be an extended pause in drumbeats. It is unclear whether 4 cm of slip would have been detectable with the observation equipment in use at the time.

To fully examine the effect of large rockfalls it is useful to consider the upper bound of volume loss, 10^5 m^3. The results follow a similar pattern to those of the smaller event and differ only in scale. In the larger event the spine slips ~40 cm immediately after the change in mass. The repressurization time is also an order of magnitude longer, at 6150 s. Again, as it is unclear whether slip of 40 cm would have been detectable, the prolonged stick period is a more likely to have been detected. The increase in stick period with necessary volume loss is shown in Figure 2.5 for volume changes of 10^2 - 10^6 m^3. In log-log space, the plot is linear for volume changes greater than about 5 x 10^4 m^3, whereas for volume changes less than this value the time interval approaches the stick period for normal SPASM behavior.
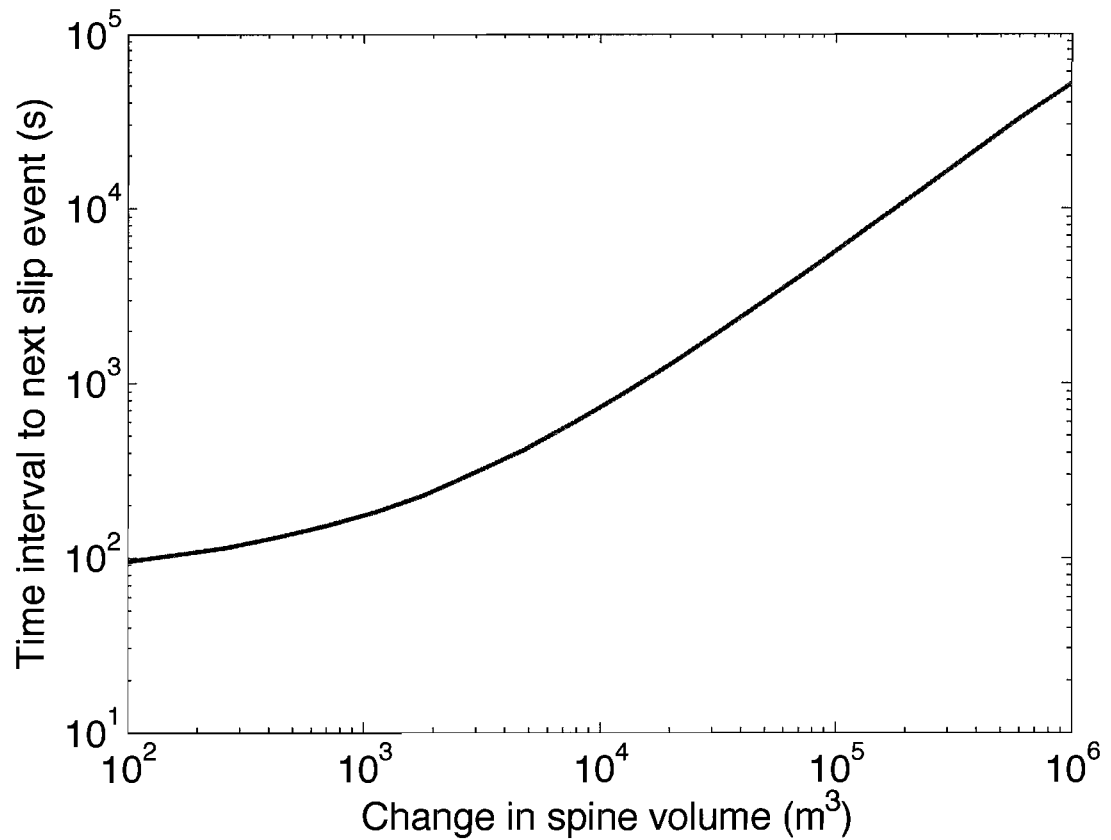
Figure 2.5. The change in spine volume refers to the amount lost during rockfall events.
The largest events were estimated at between 10^4 and 10^5 m^3. The resulting time interval
to the next slip event corresponds to the repressurization time, during which no plug slip
or earthquakes occur. For the aforementioned bounds on rockfall volume, the
repressurization, or aseismic, periods range from about 12 minutes to 1.5 hours.

The stick period is determined by finding the ratio between the difference of the new critical slip pressure and the minimum pressure following a drop in mass to the time derivative of pressure. The critical slip pressure is defined as that necessary to equal the frictional resistance when the plug is stationary (F_0), and depends on the static friction coefficient μ_0, the new plug mass m^*, gravitational acceleration g and a parameter that relates lithostatic pressure to normal stress, λ. The minimum pressure following a simulated rockfall event was found for various changes in mass through modeling, as no analytical method to determine that value exists. In the case where the plug is stationary and the rate of erosion equals the rate of basal magma accretion, the rate of pressure change dp/dt takes a simplified form and depends only on the lumped compressibility of the magma and conduit wall rock $\alpha_1 + \alpha_2$, the volume, the cross sectional area A, the volumetric flux rate Q, and the basal rate of accretion B scaled by a term R that relates the difference between densities of the magma and dacite. (Although the volume decreases as the magma repressurizes, it changes by only a few percent in the case of the large rockfall and so this value is treated as a constant, and the initial volume V_0 is used.) The equation to solve for the prolonged stick period takes the form:

$$\Delta t = - [((\mu_0 \lambda m^* g)/A - P_{min}) (\alpha_1 + \alpha_2) V_0] / (RB - Q) \qquad (2.1)$$

Figure 2.3 shows that for rockfalls of 10^4 and 10^5 m^3, the expected stick periods are about 12 minutes and 1.5 hours, respectively. These results are inconclusive as

aseismic periods of time in this range are long enough to be detected, though no reports

of such could be found.

Another problem with the SPASM model is the rate-weakening rheology assigned

to the bounding fault. Experimental data show that higher temperatures tend to favor

rate-strengthening rheology, while rate-weakening rheology is applicable only at lower

temperatures. This rheological change has been used to explain the finite depth

of the seismogenic zone in tectonic strike-slip faults. For example, Blanpied et al. (1991)

found a transition from stick-slip failure to steady sliding at a temperature of about 300

°C for experiments on granite. He et al. (2007) found similar results using gabbro

samples, and an intermediate composition of dacite would be expected to follow the

pattern of these two end member compositions. Although those experiments were

conducted using solid slabs (without gouge) at atmospheric pressures, it is clear that the

base of the plug must be above the solidus (>800 °C). This implies that at least some

portion of the bounding fault at depth would be at these elevated temperatures and

expected to exhibit steady sliding. Schneider et al. (2009) report temperatures of about

730 °C inside cracks of the spine at the surface. The role of escaping gases in the

generation of these elevated observed temperatures is unclear, but, if those measurements

faithfully record the temperature of the extruded dacite, it would suggest a slow diffusion

of heat and that temperatures high enough to generate rate-strengthening rheology exist at

shallow depths. That is not to say that elevated temperatures are strictly necessary to

produce stable sliding. Fault rheology depends on the combined influence of many

factors, including normal stress, the presence of pore fluid pressure, the presence of, and thickness and grain size characteristics of fault gouge.

It is useful to consider another explanation that is consistent with earthquake rupture theory but unfortunately untestable with the current version of the SPASM model. In this scenario, which is purely theoretical, the plug steadily extrudes aseismically in bulk but fails seismogenically in discrete slip patches to produce the observed seismicity. This is consistent with the calculations of Pallister et al. (2009), who suggest that failure along a slip patch of ~300 m^2 could generate the seismic moment detected. That in itself is more consistent with rupture theory, rather than slip occurring simultaneously over ~300,000 m^2, as suggested by the SPASM model. I note that changing from a rate-weakening to a rate-strengthening regime in the SPASM model does not change the time-averaged slip but does eliminate slip events (drumbeat earthquakes). Therefore I conclude that extrusion is characterized primarily by stable sliding but that periodic seismogenic failure along discrete patches is not incompatible with the SPASM model.

The SPASM model may be further evaluated by modeling conduit dynamics and constraining the properties of the magma close to the base of the plug. For example, SPASM requires a magma compressibility of 10^{-7} Pa^{-1}, which, according to Iverson (2009), corresponds to an average gas volume fraction of ~12%. This is higher than porosity measurements of extruded dome material of Cashman et al. (2009) and those made herein, suggesting that magma degassing and the evolution of the gas volume fraction in the conduit should be examined. The flow and evolution of magma properties

in the conduit is modeled because it is the dynamic interactions in this three-phase system

that set the thermo-mechanical conditions at the interface between the viscous magma

and the solid plug. This modeling is described in section 4.3 and chapter 5.

CHAPTER III

SAMPLE-BASED RESEARCH

Summary of field work

Two days of field work were scheduled for late August, 2008 thanks to the assistance and thorough organization of several USGS staff members led by John Pallister. A low cloud ceiling on the first day persisted well into the afternoon and dashed plans of safely flying into the crater. After a morning of uncertain weather on the second day, however, the cloud ceiling lifted high enough to allow the short flights from the staging area ~5 km away into the site of recent dome extrusion. At that time there were only two remaining coherent sections of collapsed spine large enough to accommodate the landing skids of the helicopter, a four-passenger Bell 206. Weathering and erosion had crumbled the surfaces of the other spines (Figure 3.1). Spines 4 and 5 each had a potential landing site and we opted for the better-preserved surfaces on spine 4. Data collection took two forms. First, using a standard electric drill outfitted with a coring attachment, we collected approximately 20 cores of various length (< 15 cm). Cores drilled from the spine surface (through the gouge) tended to break into a few pieces whereas cores drilled from the more intact dacite closer to the spine interior remained coherent and permitted oriented sample collection. The cored samples were used for measuring permeability and for analysis with a scanning electron microscope. The results of these analyses are described in detail in section 3.5. Secondly, we acquired images of the spine surface using an image acquisition apparatus that was designed to

Figure 3.1 The view north from the top surface of spine 4 in late August 2008. The visible vapor is a mix of steam and gases venting through the ground surface and atmospheric water vapor. Preserved sections of the spine surface are visible in the center foreground but much of the extruded material has eroded to rubble.
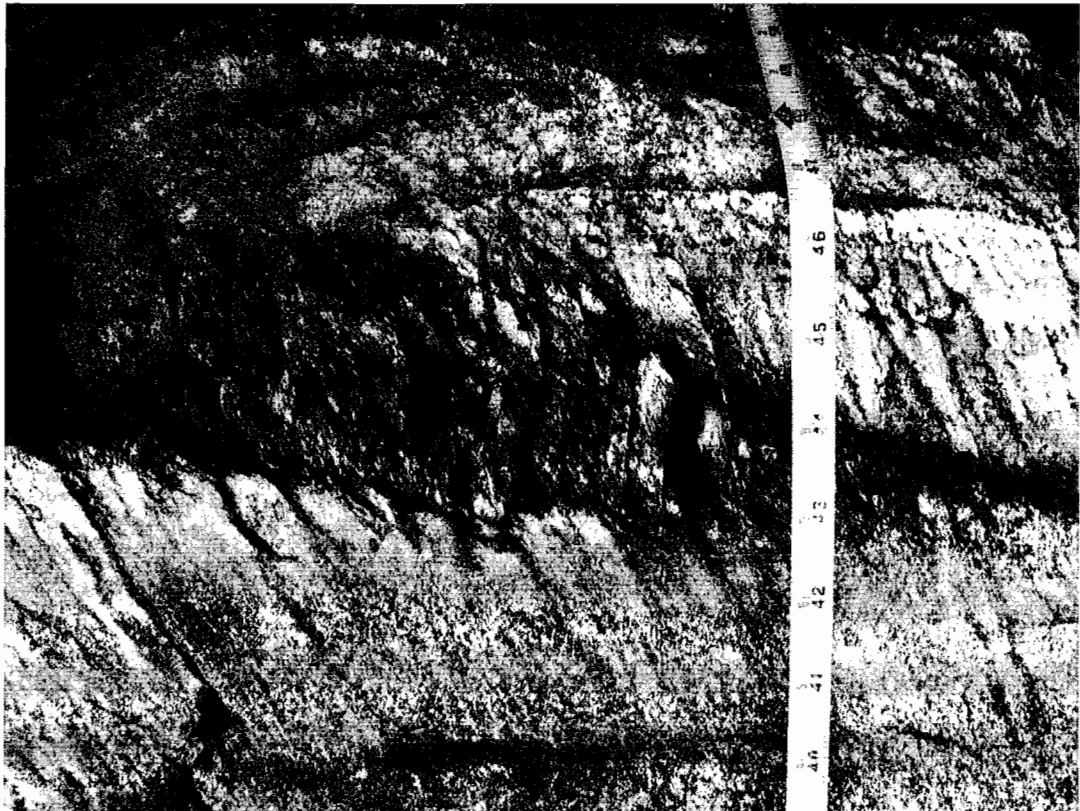
Figure 3.2 Field photo showing a cross section of outer damage zone on spine 4. Sense of shear is top to the right. There were 3-4 additional structures similar to this one identified on the ~100 m section of spine we worked on. Note: measuring tape for scale is in inches.

obtain photographs with a standard "point and shoot" camera from equal but opposite angles to the surface normal. The photographs are shot from a range of ~30 cm and have been used to generate digital elevation models of ~100 cm² sections of spine surface with a resolution limited by pixel size, typically 10s of μm. This technique and the results are described in detail in section 3.4.

Isotopic analysis

The presence of pore fluids in a fault decreases the normal stress σ_N by an amount equal to pore fluid pressure p_f. Fault shear strength τ is equal to the effective normal stress scaled by the coefficient of friction μ. This is represented mathematically as:

$$\tau = \mu(\sigma_N - p_f). \tag{3.1}$$

The effect of pore fluids is to decrease the shear strength, thereby increasing the likelihood of slip. Because the magnitude of the effective normal stress controls slip behavior, pore fluids have the potential to induce either stick-slip failure or stable sliding.

As it relates to the fault bounding the extruding plugs at Mount St. Helens, the presence of pore fluids is of interest because the slip behavior is not well understood. Pore fluids, if present, could have originated as exsolved gas that escaped the conduit and rose through the gouge layer. Alternatively, elevated temperatures may have reached the glacier base, inducing melting and the release of water, some of which may have

migrated into the gouge layer. This latter hypothesis, in fact, was proposed by Iverson (2009) as a mechanism for initiating plug extrusion.

Gouge samples were tested at the University of Oregon's Stable Isotope Lab for oxygen isotope concentrations. The samples were found to have $\delta^{18}O$ concentrations ranging from 6.9 to 7.3 per mil. These values are more consistent with results from prior analyses performed on 1980 eruption material (6.8 per mil) than with meteoric water (~14 per mil). This suggests that any water present in the gouge layer during plug extrusion had a magmatic, rather than glacial, source.

Quantifying fault surface textures

This section introduces a new technique used to generate digital elevation models (DEMs) of hand sample size portions of fault surfaces and to quantify the surface textures. UCORE Fellow Naomi Meacham provided considerable support with this project. The method relies on using MeX software (Alicona) to generate DEMs from images of the surface captured from equal angles but opposite directions from the surface normal. This software has been used to generate DEMs from SEM images, in which the SEM stage is rotated by precise amounts and the working distance (camera to sample length) is small. Here I use the software with gray scale digital images obtained using a standard digital camera. The camera attaches to the underside of a tripod and photographs the fault surface from a distance of 30 cm and an angle of 15° from the fault surface normal. A second image is subsequently captured from an orientation of 15° from the surface normal in the opposite direction. A working distance of 30 cm allows

imaging areas that are approximately 25 cm by 25 cm. The DEM is constructed from a smaller area located in the center of those images because the fringes of the images tend to be slightly out of focus. Some images were also obtained in situ of fault surfaces from spine 4. The environmental lighting while those images were taken was variable due to passing clouds, and the best DEMs were produced from images acquired in the lab under controlled lighting conditions from hand samples collected from spine 4.

Figure 3.3 shows a typical DEM constructed using this method. The vertical exaggeration is set to 3x in this image to enhance the structure of the striations on the surface. The surface itself is a highly coherent and extremely fine-grained layer of fault gouge that is widely exposed on the spine surfaces and I take to represent the slip surface. These surfaces are characterized by striations that are elongated parallel to the direction of slip and have a vertical relief of < 1 mm.

After successful construction of a DEM, a series of profiles were obtained and the lateral coordinates (either x or y) and the heights (z coordinates) were exported to MATLAB to perform discrete Fourier transform analysis. Figures 3.4 and 3.5 show the power spectral density of a series of profiles in the x- and y-directions, respectively. The power spectra for profiles normal to the slip direction show less variation in power for a given wavelength. This may be a result of the orientation of pits on the fault surface, which tend to be elongate in the x- direction and would therefore tend to skew the results for profiles parallel to slip. In both cases, the slope of the power spectra curves
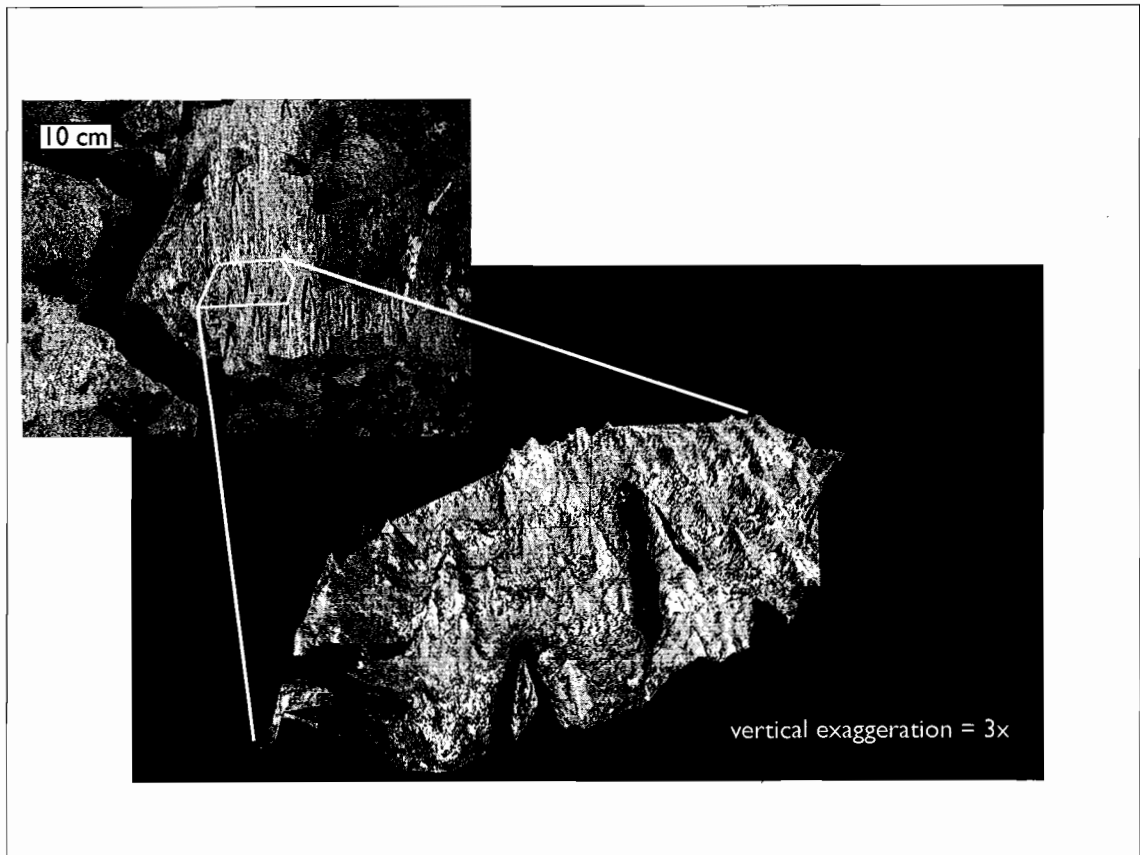
Figure 3.3. A typical DEM constructed using the method described in the text. The DEM is approximately 10 cm wide. The vertical exaggeration is 3x. The back markings were made with a marker to highlight the striations and to label the sample.
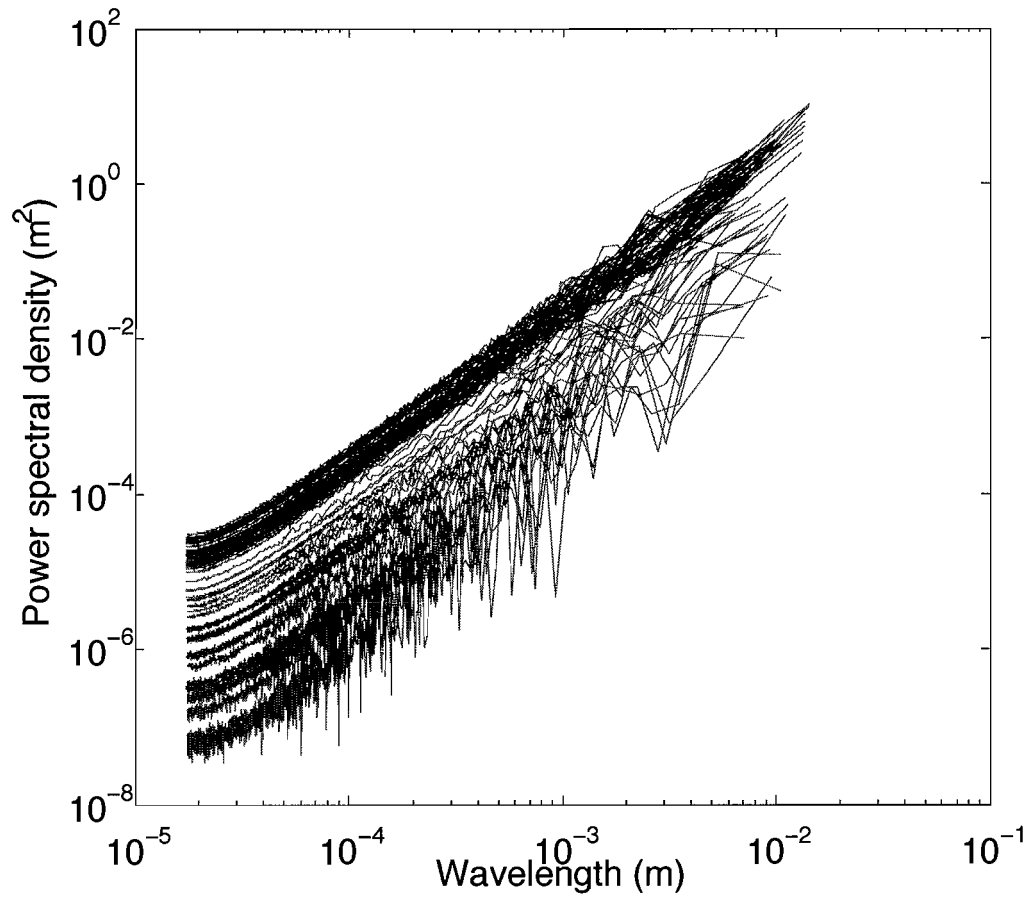
Figure 3.4. Power spectral density for ~40 profiles normal to slip direction. The profiles all follow a power law.
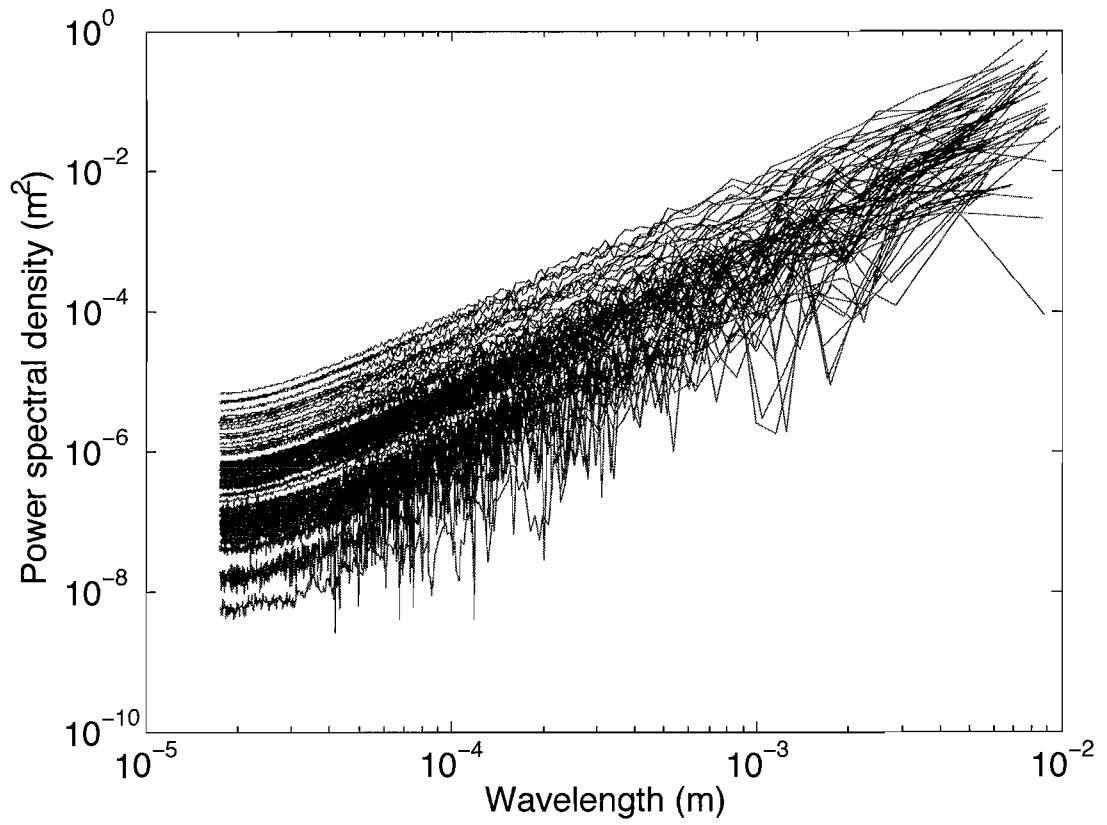
Figure 3.5. Power spectral density for ~40 profiles parallel to slip direction. The profiles all follow a power law.

concavely at the lower wavelength limit. This represents the limit of resolution for this technique of a few tens of microns.

Sagy et al. (2007) and Sagy and Brodsky (2009) have performed Fourier transform analysis on fault surfaces. Those studies used ground-based light detection and ranging (LiDAR) to scan outcrops and a profilometer to scan hand samples in the laboratory. Those studies examined both large-slip (10s to 100s of m) and small-slip (<1 m) faults and found that small-slip fault surfaces tend to be rougher than the surfaces of large-slip faults, which they found were polished over distances of meter scale. At large scales they exhibit an undulating topography. They found the power spectra of small-slip faults to follow a power law but that the large-slip faults did not exhibit such behavior because they smooth and geometrically simplify with increasing displacement.

The results from Sagy et al. (2007) and Sagy and Brodsky (2009) suggest that the power law striations on the spine surfaces from Mount St. Helens were produced by small amounts of total fault slip. This seems to be inconsistent with the concept of a crystalline plug extending about 500 m below the crater surface. One explanation is that localized slip is small, and that slip relocalizes every meter of total plug slip. This, however, seems implausible given the coherence and lateral continuity of the upper layer of fault gouge.

While the results from this technique offer inconclusive interpretation based on the limited amount of prior work, it nonetheless showcases the high resolution available

with relatively low cost equipment. This technique will likely show increasing potential as data from other surface scanning projects become available.

<div align="center">SEM results</div>

A total of five samples collected during the field operation were analyzed at the University of Oregon's Micro Analytical facility with a scanning electron microscope (SEM). The goal of this analysis was to examine the microstructure and to constrain porosity measurements. All samples were drilled from the outer 2 m of the spine surface and accordingly represent the fault gouge or brecciated damage zone. Image analysis calculated porosities of 3.47 - 8.18%. These values are representative of the gouge layer and brecciated zone are not taken as measurements of the intact dacite. Dilation is a common process in granular shear zones and therefore the intact dacite is expected to have a lower porosity than these values. Figures 3.8 and 3.9 show photomerged images obtained from sample 13 and 16, respectively. Both samples are characterized by elongated microcracks oriented in the same direction. This suggests that the fault gouge may be relatively permeable and four samples were successfully tested in a permeameter. The calculated viscous permeability measurements ranged from 1.1×10^{-13} m^2 to 6.4×10^{-15} m^2. The texture of the cracks may reflect shear strain accommodation near the brittle-ductile transition. This seems an almost necessary process for the case at Mount St. Helens with a rheological transition at depth and steady extrusion. The structure is also similar to the cross section scale cracks pictured in Figure 3.2 and both types of features may represent similar processes acting over different length scales.
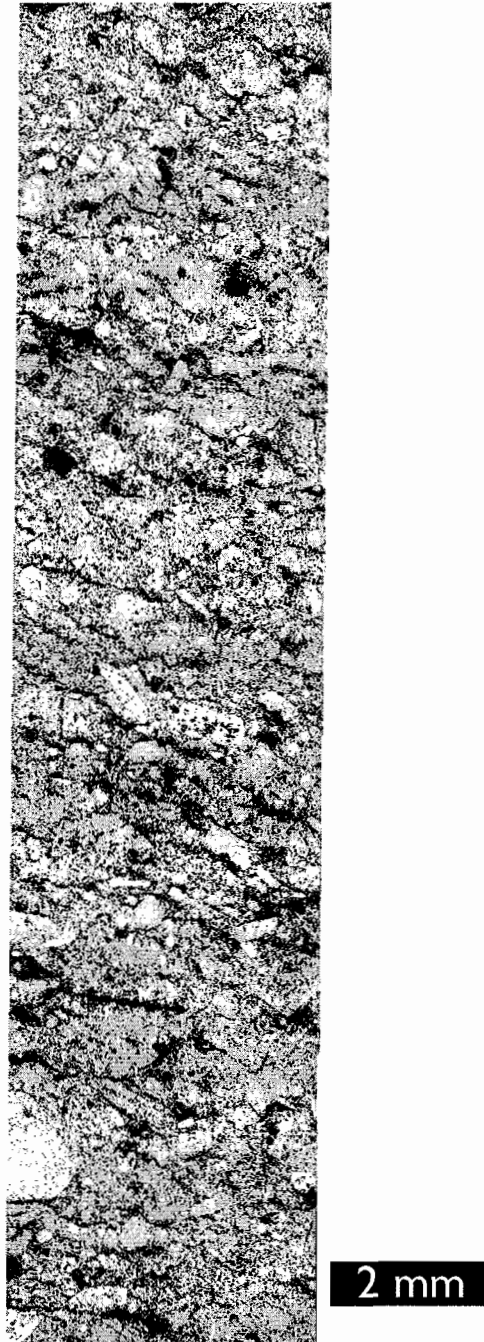
Figure 3.6. Photomerged composite image of sample MSH_16 at 90x magnification.

The pore spaces are oriented in elongate microcracks.
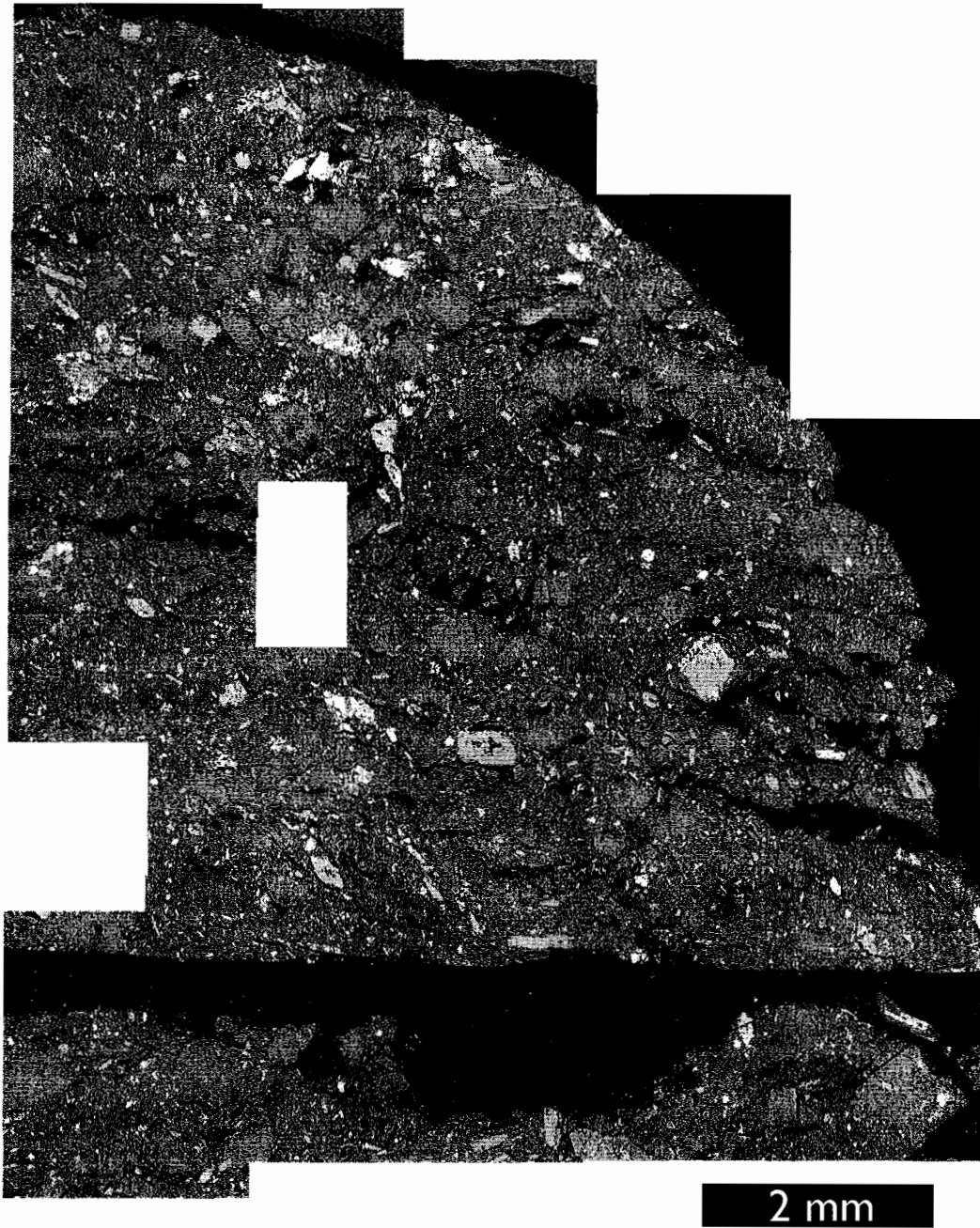
Figure 3.7. Photomerged image of sample MSH_13 at 90x magnification. Note the alignment of pore spaces in elongate microcracks.

CHAPTER IV

MODELING BACKGROUND

Silicic volcanism

Silicic volcanoes have a highly varied range of eruptive styles and products

compared to basaltic systems. This can be explained by the large range in properties of

silicic magmas that result from pressure drops of at least three orders of magnitude and

environmental temperature changes of several hundred degrees Celsius from magma

storage conditions (e.g. Eichelberger, 1995). Highly explosive plinian eruptions represent

the most violent end member of silicic eruptions, whereas effusive dome growth produces

much less erupted material and poses little threat as a hazard to aviation or to

communities living nearby. A single volcano is capable of producing both explosive and

effusive eruptions, which in part supports the understanding that the magma flux rate,

rather than chemical composition, volatile concentration, or conduit geometry, all

parameters that may be volcano-specific, control the eruptive style. At Soufrière Hills

volcano, Montserrat, Watts et al. (2002) found that extrusion rates of 0.5 - 2 m^3/s resulted

in the extrusion of spines, rates of 2 - 9 m^3/s produced lava lobes, and rates > 9 m^3/s

resulted in Vulcanian explosions. (From December 2004 - December 2005 the

volumetric flux rate during spine extrusion at Mount St. Helens was ~1.5 m^3/s, consistent

with the findings of Watts et al., 2002)

As silicic magma ascends it decompresses. Pressure changes that accompany

transport from chamber to surface generally have a greater control over magma properties

than the corresponding changes in temperature. This is a consequence of the presence of dissolved water in the source magma (water being the dominant volatile compound), the ability of melt to retain dissolved water until low pressures compared to other volatiles, such as CO_2, the strong influence of dissolved water on magma solidification, and the strong influence of crystallization on magma viscosity. Silicic source magmas contain at least several weight precent dissolved water. Whitney (1975) measured the solidus temperature of an anhydrous silicic magma at 1200 °C, whereas a second magma of the same composition but with 6.6 weight percent water added had a solidus of 835 °C. This not only highlights the strong influence of dissolved water on solidification, but also raises the issue of identifying an environment capable of generating silicic magma at the elevated temperatures required in the anhydrous case. Magma chamber temperatures typically range from about 750° C to 950° C. This requires the presence of at least a few weight percent water in the magma. This represents a small mass fraction of the overall magma, but because of increased exsolution at shallower depths and the expansion of bubbles due to decreasing pressure, a few weight percent water would comprise more than 99% of the magma by volume at atmospheric pressure.

Insight into the end member cases of silicic eruptive styles can be gained by considering the amount of exsolved water that is erupted with the lava. Magma with greater than 75% bubbles by volume is classified as a "dusty foam," and models of explosive eruptions successfully treat ash plumes as a fluid. Explosive eruptions are essentially the release of overpressured gas with entrained crystals and melt or ash.

Sparks et al. (1977) found that pumice samples typically do not exceed 70-80%

vesicularity, and he proposed that for magmas with > ~75% gas volume fraction the

bubbles become overcrowded. If magma at this threshold continues to decompress,

further expansion may be achieved only by fragmentation that results in an explosion.

The fragmentation depth is thought to propagate downward, evacuating the conduit until

the conduit walls respond to the loss in confining stress by collapsing and sealing the

conduit. This process must occur at a range of scales given the range in magnitude of

eruptions. Effusive eruptions, on the other hand, tend to produce dense eruptive products

with little vesicularity despite evidence that the magma at some point contained enough

dissolved water to eventually reach the fragmentation threshold. The two mechanisms

that allow the release of gas from magma in the conduit are bubble rise and permeable

flow laterally and/or vertically out of the conduit. Ignoring the path effect of crystals,

considering that the Stokes rise velocity for a bubble of radius 10 mm is $< 10^{-5}$ m/s for

typical silicic magma viscosities of $> 10^7$ Pa s, it seems clear that permeable flow of gas

must dominate when significant gas transport takes place. Jaupart and Allegre (1991)

proposed that the importance of ascent velocity on eruptive style is a direct consequence

of competing time scales of magma flow and permeable flow of gas out of the conduit.

Magmas rising at sufficiently high rates will transport bubbles vertically before extensive

lateral degassing can occur. Retention of bubbles lowers the overall magma density and

requires faster flow velocities to balance mass flux, reinforcing the process. Slow ascent

velocities, meanwhile, permit sufficient degassing and keep the bubble volume fraction

low. This keeps the density high and the velocity low. Bulk magma viscosity also controls the magma flow velocity. High viscosity magmas flow slowly, allowing for degassing, high density magma and, therefore, large pressure gradient magnitudes. The result is increased decompression crystallization and an increase in bulk viscosity because of the rheological stiffening that accompanies an increasing volume fraction of solids.

Quantifying gas escape by permeable flow requires knowledge of the conduit geometry, wall rock permeability, and magma permeability and its dependence on porosity. For the relationship between porosity and permeability, magma is generally considered impermeable until bubble connectivity occurs at ~60% porosity. Moreover, Rust and Cashman (2004) proposed, on the basis of various experimental studies, a hysteretic permeablity-porosity relationship. This suggests that once bubbles are connected, it is difficult for the magma to immediately isolate them again following gas loss. Michaut et al. (2009) introduced a numerical model to capture the effect of bubble connectivity maintained at porosities below the threshold for connectivity. Regardless, permeable gas escape remains difficult to quantify.

Previous conduit models

Modeling the dynamics of silicic magma systems has been given much attention in recent years, beginning with the work of Melnik and Sparks (1999). Their model, like most that focus on conduit dynamics, does not consider magma chamber dynamics, but instead defines a source magma with an initial pressure, temperature and water content.

They used properties appropriate for the 1995-1999 dome-building and vulcanian eruption of Soufrière Hills, Monserrat. The basic components of the model are: (1) steady-state conditions, (2) fixed conduit height and uniform conduit radius, (3) water exsolution proceeding according to a solubility law governed by pressure and empirical constants, (4) vertical gas flux governed by Darcian flow, with magma permeability dependent on gas volume fraction, (5) Poiseuille flow of magma, implying no-slip boundary conditions, a parabolic velocity profile in the radial direction and viscous flow resistance, and (6) mass conservation of both magma and gas. Magma effusion produces a dome that increases the lithostatic load on the underlying magma, thus decreasing its overpressure. Their model initially assumed an isocrystalline magma with a constant viscosity, but these conditions predicted implausibly large dome heights for given volumetric extrusion rates. Their final model incorporated empirically-derived relationships for increasing crystal content with decreasing depth and for bulk magma viscosity that increases logarithmically with crystal content. These improvements produced good agreement with data relating dome height to extrusion rate. They found that maximum overpressure, defined as magma pressure in excess of lithostatic pressure, occurred at depths of a few hundred meters, rather than deeper in the conduit or at the top of the magma chamber. This was consistent with both ground deformation patterns, which can be explained by magma overpressures at depths of between 400 and 700 m, and with the presence of shallow seismicity. Moreover, the identification of shallow magmatic overpressures is consistent with assumed processes leading to vulcanian

eruptions, in which shallow gas overpressures exceed magma strength, fragmentation occurs, and relatively small amounts of material erupt on account of the shallow source.

Barmin et al. (2002) and Melnik and Sparks (2005) subsequently developed transient models of magma flow in the conduit and resultant effusive behavior. Their focus on time-dependency of conduit dynamics was motivated by observed transitions from dome-building to explosive eruptions, such as at Pinatubo in 1991, or from explosive to dome-building eruptions, as occurred at Mount St. Helens during 1980-1986. Competition between the time scales for crystallization and magma ascent is thought to be the dominant control on eruptive behavior (e.g., Eichelberger, 1995). When magma ascent is slow relative to crystal growth kinetics, crystallization proceeds largely in equilibrium, which results in higher crystal volume fractions, and, therefore, higher bulk viscosities. This, in turn, keeps magma ascent rates low, thus reinforcing the process. Gas exsolution occurs largely in equilibrium with slow changes in pressure and thus promotes outgassing from the conduit. On the other hand, a transition to a higher magma flux rate depresses crystal volume fractions, lowers bulk viscosity, increases ascent rates and limits opportunities for escape of gas from the conduit, thus setting the stage for an explosive eruption.

Barmin et al. (2002) use the same Poiseuille flow law as Melnik and Sparks (1999) in addition to their empirical equation for evolution of crystal content. They ignore gas exsolution and changes in density and impose a bimodal viscosity law in which it instantaneously increases by several orders of magnitude once a critical crystal

content is attained. They advance the model of Melnik and Sparks (1999) by incorporating magma chamber dynamics. They allow magma chamber pressure to change over time, they evaluate the influence of magma chamber volume on eruption rate, and they account for elastic response of rock surrounding the chamber. Their calculations for transient changes in volumetric extrusion rate are in good agreement with existing data over time scales of several years at Mount St. Helens from 1980-1986, as well as over several decades at Santiaguito, Guatemala from 1915 to 2000.

Melnik and Sparks (2005) advance their prior work primarily by incorporating a complex treatment of crystal growth. In this model, evolution of crystallization takes account of the further growth of phenocrysts supplied from the magma chamber and the nucleation and growth of microlites in the conduit. Temperature change is also considered in that crystallization releases latent heat. Crystal growth depends on undercooling such that kinetic effects during crystallization are accounted for. The laws governing crystal growth are ultimately calibrated with results from decompression experiments on magmas of similar composition to those at Soufrière Hills (Couch et al., 2003a). As earlier, gas exsolves and flows vertically according to Darcy flow governed by the local pressure gradient and the magma permeability. They use the empirical viscosity relationship derived from their earlier work and explore the effects of magma chamber size and temperature on extrusion rate. Melnik and Sparks (2005) identified three regimes of conduit flow. In the first, the flow rate is high and the magma viscosity is low. The second regime is characterized by slow magma ascent, extensive

crystallization and the eruption of nearly solid magma with a very high viscosity. The third regime is unstable and involves oscillation between the former two stable regimes. They found that small changes in any parameter they focused on could result in eruptive behavior under any of the three regimes because of the non-linear and sensitive nature of conduit dynamics. They also found that changes in some parameters could produce a transient change in periodicity for oscillations in the unstable regime.

A recent model of Diller et al. (2006) uses many of the principles of Melnik and Sparks (1999) in that it is steady-state, assumes Poiseuille flow of magma in the conduit and allows for vertical Darcian flow of gas. A major departure, however, is that they allow lateral flux of gas after Jaupart and Allegre (1991), where gas flux is governed by a lumped-parameter Darcy's law controlled by the permeability of the wall rock and a psuedo-pressure gradient defined as the difference between magma pressure and lithostatic pressure normalized by a characteristic length scale (in this case, the conduit radius). For lateral flux to occur they impose a bubble connectivity threshold of 60% and define vertical permeability following Klug and Cashman (1996). Their model is isothermal and isocrystalline and focuses largely on vertical variations in density resulting from changes in gas volume fractions. They found that lateral outgassing produced a dense plug at the top of the conduit that varied in thickness depending on parameter values but was typically a few hundred meters thick. Increased volumetric flux of magma and increased bubble connectivity thresholds decreased the thickness of the plug, while lower wall rock permeability values and higher water concentrations in

the source magma decreased the density of the plug. They defined end-member cases, the first of which involves a dense magma plug several hundered meters thick residing at the top of the conduit; in such a case eruptions would proceed effusively. The second end member case involves a thin (< 100 m) cap of high density magma overlying highly vesicular magma; this situation was expected to generate periodic explosions of relatively low intensity (vulcanian eruptions). Diller et al. (2006) set model parameters appropriate for Soufrière Hill Volcano and use their results to explain the observations of both dome-building eruptions and vulcanian explosions.

Vitturi et al. (2008) use the ingredients of the model of Diller et al. (2006) to investigate the influence of variable conduit geometry on magma flow. They focus on conduits that expand at depth over a small vertical distance. Physically, this could represent either accretion along the lower conduit or erosion of the upper conduit. Changes in conduit geometry are defined by the ratio of the upper radius to the lower radius and the depth of conduit expansion. They found that conduit geometry has a strong influence on both volumetric extrusion rate and the formation of dense magma plugs in the upper conduit. High radius ratios (> 2) tended to generate denser, thicker magma plugs, which would be expected to produce effusive eruptions. They also concluded that, all other properties remaining constant, changes in conduit geometry over time would generally cause changes in eruption rate, and hence possibly also in eruptive style.

Taisne and Jaupart (2008) developed a model that captures a relationship between dome-building and the lateral permeability in the upper conduit. They assume that magma enters the conduit with a pressure and water concentration and ascends, thereby exsolving gas. Bubbles are outgassed continuously until the depth in the conduit equals the radius of the overlying dome. At that critical depth the weight of the overlying dome closes cracks, on the basis that small increases in pressure are needed to do so, and the conduit is sealed from that depth and above. They investigated a range of critical depths, from 0.5 to 2 times the dome radius, but found that a factor of 1 gave the best fit to the dome geometry data. This model is relatively simple in that it assumes that density depends only on the amount of exsolved gas present and ignores crystallization, thereby ignoring the fact that increasing crystal content accelerates gas exsolution. However, the model captures several observations simply by considering the effect of dome height and radius on wall rock permeability. First, when dome-building initiates, the dome is small, and cracks are sealed off only to shallow depths. Nonetheless, because of accelerated gas exsolution at shallow depths, a highly vesicular magma can result. It is overlain by a thin dome with limited resistance to a pressurized magma. This would be expected to generate a dome explosion, which is in fact consistent with observations at Mount St. Helens during the summer of 1980 when dome building began. The model can also account for intermittent dome growth, a commonly observed characteristic. Once a dome is established, it can generate a substantial load on the underlying magma column. This increase in lithostatic load can impede ascent of magma, thereby stalling further dome

growth. During this time of no extrusion the dome viscously relaxes over a time scale dependent on the dome dimensions, viscosity, and density. Once sufficient mass of the dome has spread off of the magma column magma flow can restart and will continue until the weight of the dome stalls further extrusion.

Finally, the model of Lensky et al. (2008) addresses the importance of disequilibrium degassing. Their interest was in understanding cyclic dome extrusion at Soufrière Hills Volcano. The uppermost portion of the conduit was occupied by a dense plug of magma. They impose a rate-weakening rheology of the cylindrical fault between the plug and the conduit wall. In their model the exsolution of gas into existing bubbles lags behind decompression, resulting in a difference between gas pressure - the pressure inside the bubbles - and the pressure of the surrounding magma. Plug motion begins when the gas pressure reaches a critical threshold. The period between slip events is therefore strongly dependent on the time scale of gas pressurization. As the plug extrudes the bubbles expand, thereby increasing the volume fraction of gas and increasing the permeability of the magma for gas escape. Gas pressure decreases with outward flux of gas and once a critical pressure for plug arrest is attained, motion of the plug ceases. This sets the stage for the now underpressured gas to pressurize and repeat the cycle. While the extrusive behavior is ultimately dependent on the time scales of gas pressurization and on the rheology of the bounding faults, both poorly-constrained parameters in practice, their model nonetheless highlights the potential importance of disequilibrium degassing on eruptive style.

Components of the model

General model setup and initial conditions

Figure 4.1 shows the general schematic setup of the model space. A vertical conduit of height H and radius R delivers magma from the top of the chamber at $z = 0$ to the base of the plug at $z = h$. The plug occupies the uppermost portion of the conduit, a thickness equal to $H - h$, and extends above the crater floor to some height equal to the height of the spine z_s. The conduit radius R is constant for the entire height of the conduit. The focus of this model is the flux of magma out of the crater floor and changes in its properties The plug is of interest only insofar as it sets constraints of pressure, porosity and velocity on the magma directly below it and represents a substantial barrier to vertical gas flow. Measurements of spine extrusion rate and porosity of the dacite provide constraints on the magma velocity V and gas volume fraction α at $z = h$.

From lubrication theory, the rate of lateral flow of magma is of order (R/H) times the ascent velocity. Because $H \gg R$, it is assumed that lateral flow of magma is negligible. The high magma viscosity ensures that the Reynolds number Re is much smaller than 1, and so turbulence is neglected and flow is assumed to be laminar in the z direction. A one dimensional treatment for the conduit is therefore appropriate, with the exception of the region within one radius length of the plug base. Because this project is focused largely on the dynamics of the entire conduit, the exceptions to one dimensional flow close to the plug are ignored. From December 2004 - December 2005 the volumetric extrusion rate was nearly constant (Schilling et al., 2009) and I consider
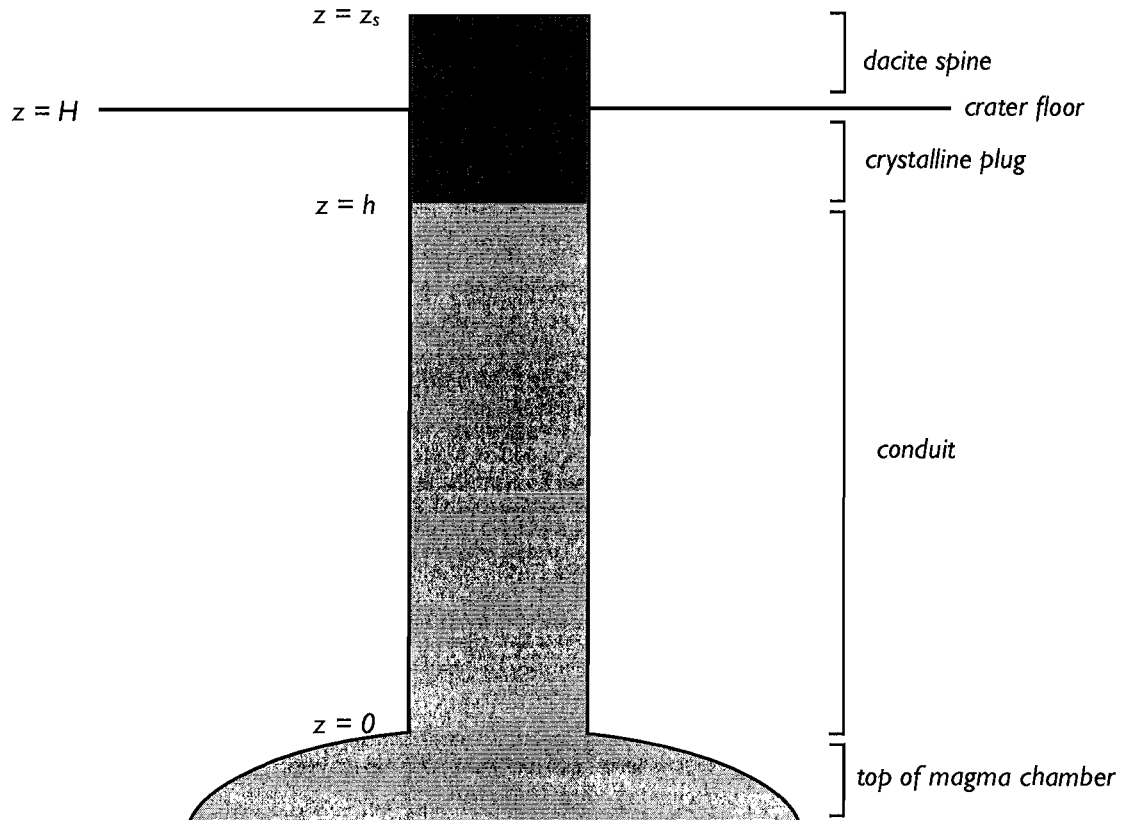
Figure 4.1. The schematic layout of the model. Magma flux and properties are calculated over the height h. The magma-plug transition is at a depth $H\text{-}h$. Porosity of extruded material constrains a low magma porosity at the transition depth and the low extrusion rate suggests small overpressures, or magma pressure at $z=H\text{-}h$ near lithostatic values.

steady state conditions using the extrusion rate during that year-long period as a constraint. Magma enters the conduit from the top of the chamber at an initial temperature T_0, pressure p_0 and water concentration N_o. Values for each of these three parameters as well as the conduit height H have been constrained by petrologic studies of samples erupted during 2004-2006 (e.g., Pallister et al., 2009). Values for all parameters used are listed in Table 4.1 and a discussion on the influence of the parameters appears in Chapter 5.

Conservation of momentum of magma

Because flow is laminar and the conduit is a vertical cylinder with a fixed radius, the conservation of momentum takes the form of a Poiseuille flow law. The vertical pressure gradient dp/dz minus the local magmastatic pressure gradient ρg drives flow of magma at velocity V, where ρ is the bulk magma density and g is the gravitational acceleration. Flow is resisted by viscous interactions with the conduit wall, represented by the bulk magma viscosity η, and also depends on the conduit radius and a geometric factor, which, for a cylinder, is 8. The magma velocity represents a radially-averaged value, as the conduit walls require a no-slip boundary condition and the resulting velocity profile across the entire conduit width is parabolic. The momentum equation is used to solve for the local pressure gradient and takes the form:

$$dp/dz = -\rho g - (8\eta V)/R^2. \tag{4.1}$$

Variable	Description	Units	Nominal value	Range	Reference(s) / comments
g	Acceleration due to gravity	m/s^2	9.81	-	Typical value at Earth's surface
R	Conduit radius	m	100	22.5 - 150	Schilling et al., 2009
H	Conduit height	km	5.4	4.5 - 6.5	Pallister et al., 2009; Rutherford et al., 2009
p_0	Pressure at conduit base	MPa	130	105 - 145	Pallister et al., 2009; Rutherford et al., 2009
T_0	Temperature at conduit base	°C	850	775 - 900	Pallister et al., 2009; Rutherford et al., 2009
N	Water concentration of source magma	kg/kg	0.05	0.03 - 0.07	Pallister et al., 2009; Rutherford et al., 2009
ρ_{xl}	Solid density	kg/m^3	2,625	-	Cashman et al., 2009
ρ_l	Melt density	kg/m^3	2,300	-	Results from pMELTS experiments
v_{exit}	Linear extrusion velocity	m/s	6.7 x 10-5	-	Schilling et al., 2009
Composition	Average for spines 3-7	[ ]	(see reference)	-	Pallister et al., 2009
η_{max}	Maximum viscosity	Pa s	1 x 10^{12}	-	Costa, 2005; Cashman et al., 2009
α_{exit}	Porosity of dome material	[ ]	0.05	-	Cashman et al., 2009; measurements made herein
η_g	Solubility exponent	Pa $^{-1/2}$	0.5	-	Burnham, 1975
R_{gas}	Gas constant for water	J/kg °K	461	-	
C_f	Solubility coefficient	[ ]	4.1 x 10^{-6}	-	
s	Viscosity of gas	Pa s	1.5 x 10^{-5}	-	
k_{lat}	Lateral permeability	m^2	0	0 - 10^{-14}	
k_{vert}	Vertical permeability	m^2	0	0 - 10^{-12}	
α_{cr}	Bubble connectivity threshold	[ ]	0.6	0.3 - 0.7	

Table 4.1. List of properties for magma, dome rock and conduit. Constants are assigned with a given value as listed. Variables are assigned a nominal value and a range is given that corresponds to sensitivity tests, for which the results are introduced in Chapter 5.

Conservation of momentum of gas

In the base case the conduit is sealed to lateral gas loss and gas ascends at the

magma velocity V. Here, gas exsolution and bubble expansion are accommodated by a

decrease in magma density and increase in ascent velocity. To consider the effects of

both lateral and vertical gas flux, the conservation of momentum of gas takes the form of

Darcy's flow law where a local pressure gradient ∇p drives flow, which is also controlled

by the permeability k of the porous medium and the viscous resistance of the gas η_g.

Because $\rho_g g$ is much smaller than ∇p, the buoyancy effects on gas transport are

negligible and the momentum equation, when solving for gas velocity u, takes the form:

$$u = -(k/\eta_g)\,\nabla p \tag{4.2}$$

Lateral gas flux is driven only by a lateral pressure gradient dp/dx. Gas

exsolution is taken to be instantaneous and therefore always in equilibrium. Because

surface tension is neglected, gas pressure is accordingly equal to local magma pressure p.

A threshold gas volume fraction for bubble connectivity α_{cr} must be met for lateral gas

flux to occur; below this value lateral gas flux q_{lat} is taken to be 0. Because gas can travel

only through the liquid phase of magma, the threshold volume fraction refers to the

volume of gas per unit volume of gas and liquid, or $\alpha_{cr} = \alpha/(1-\beta)$, where β is the solid

volume fraction of magma. Once the critical gas volume fraction has been met bubbles

are considered to remain connected.

At the magma-conduit wall interface, gas can flow only where bubbles occupy that interface, and so the flux term must be scaled by the gas volume fraction. Once the gas has left the conduit it may take one of two general paths. First, it may travel vertically as vapor through a permeable network of fractures at elevated temperatures adjacent to the conduit and escape at the surface as steam, consistent with observations (Schneider et al., 2009). Secondly, gas that does not immediately rise vertically is taken to migrate further from the conduit, encounter cooler temperatures, condense, and flow through the saturated fracture network towards the surface. This is consistent with the detection of magmatic isotopic signatures in water samples collected in 2005 at Step Canyon and Loowit Creek (Bergfeld et al., 2009). Regardless of the path a particular parcel of water takes, this physical framework suggests that local hydrostatic pressure p_{hyd} should be used as a minimum pressure of the water outside of the conduit. The lateral pressure gradient is approximated as the difference between gas pressure inside the conduit p and the water pressure outside the conduit p_{hyd} scaled by characteristic length scale, R. This is similar to the approach used by Jaupart and Allegre (1991) and Diller et al. (2006), although those models define the pressure outside the conduit as lithostatic. Here, the hydrostatic pressure is used because water outside the conduit probably does not reach lithostatic values. The permeability of the fracture network k_{lat} controls the rate of gas flux from the conduit to the wall rock. Finally, the flux term is scaled by the local

gas density ρ_g so that a mass flux is calculated. The lateral gas momentum equation therefore takes the approximate form:

$$q_{lat} = -(\alpha\rho_g k_{lat}/\eta_g)\ (p-p_{hyd})/R \tag{4.3}$$

Vertical gas flux is driven by the vertical gas pressure gradient, which is equivalent to the vertical magma pressure gradient dp/dz defined by equation 4.1. As with lateral gas flux, bubble connectivity is a requirement for gas flux, and so only when $\alpha/(1-\beta) > \alpha_{cr}$ is vertical flow considered. Vertical gas flux is limited by the vertical permeability of the magma k_{vert}, which is permitted to vary from k_{lat} for the purposes of investigating the influence of anisotropic system permeability. Vertical gas flux takes place at some velocity V_α that is in excess of the magma ascent velocity V. The vertical gas momentum equation therefore takes the form:

$$V_\alpha-V = -(k_{vert}/\eta_g)\ dp/dz. \tag{4.4}$$

Conservation of mass flux of magma and water

Defining a conduit control volume of height dz and radius R helps in identifying appropriate mass flux equations. The mass flux of magma and gas leaving the top of the control volume is equal that entering the base minus any mass of gas lost laterally. The mass flux of magma and vertical mass flux of gas operate over the cross section of the

control volume, an area equal to πR^2, whereas the lateral gas flux operates over the outer area of the control volume, $2\pi R dz$. Therefore, it is useful to introduce a modified lateral flux term $Q = 2q/R$. The general magma mass flux equation takes the form:

$$d/dz \ [\rho V + \rho_g(V_\alpha - V)] = Q \qquad (4.5)$$

Mass flux of water is also conserved over the height of the control volume where the mass flux of water leaving is balanced by the lateral and vertical fluxes of gas. To conserve gas mass flux the term ρ_{H2O} is introduced, which represents the sum of the mass of bubbles $\rho_g\alpha$ and the exsolved gas ρc_g in a unit volume of magma, where c_g is the mass concentration of dissolved water in the magma and is described in section 4.3.5. The water mass flux equation takes the form:

$$d/dz \ [\rho_{H2O}V + \rho_g(V_\alpha - V)] = Q \qquad (4.6)$$

Equations (1), (4), (5) and (6) may be combined to provide expressions for dV/dz and $d\rho_{H2O}/dz$ that take the form:

$$dV/dz = [\rho + 8\rho_g k_{vert}\eta/(\eta_g R^2)-(\partial\rho/\partial\rho_{H2O})(\rho_g k_{vert}g+V)(\rho_{H2O} + 8\rho_g k_{vert}\eta/\eta_g R^2)/(V+(\rho_g g k_{vert}/\eta_g)\partial\rho/\partial\rho_{H2O})]^{-1}$$

$$\cdot [\, Q - (\partial\rho/\partial\rho_{H2O})(V +\rho_g kg/\eta_g)(V+(\rho_g g k/\eta_g)\partial\rho/\partial\rho_{H2O})^{-1} [\, Q - (8\rho_g kV/\eta_g R^2)\, \partial\eta/\partial z -$$

$$(\rho g + 8\eta V/R^2)(k_{vert}/\eta_g)\, \partial\rho_g/\partial p - (\rho_g g k_{vert}/\eta_g)\, \partial\rho/\partial z\,] - (V+\rho_g g k_{vert}/\eta_g)\, \partial\rho/dz -$$

$$(\rho g + 8\eta V/R^2)(k_{vert}/\eta_g)\, \partial\rho_g/\partial p - (8\rho_g kV/\eta_g R^2)\, \partial\eta/\partial z\,] \qquad (4.7)$$

$$d\rho_{H2O}/dz = [V +(\rho_g g k/\eta_g)\partial\rho/\partial\rho_{H2O})\,]^{-1} [\, Q - (8\rho_g kV/\eta_g R^2)\, \partial\eta/\partial z - (\rho g + 8\eta V/R^2)(k_{vert}/\eta_g)\, \partial\rho_g/\partial p -$$

$$(\rho_g g k_{vert}/\eta_g)\, \partial\rho/\partial z - dV/dZ\, (\rho_{H2O} + \rho_g k\eta/\eta_g R^2)\,] \qquad (4.8)$$

Equations (4.1), (4.7) and (4.8) represent the governing equations of the model.

Exsolution of gas

Water is the only volatile considered here because of its relative abundance compared to other volatiles such as CO_2 and its relative importance at shallow depths (e.g., Eichelberger, 1995). The concentration of dissolved water depends on magma pressure p, the solubility coefficient s and an empirically-derived exponent m. Because gas dissolves only in the melt phase, the solubility law is scaled by a factor of $(1-\chi-n)$, where χ and n represent the mass fraction of crystals and bubbles, respectively. The

crystal mass fraction χ is related to the crystal volume fraction β by the magma density ρ and the crystal density ρ_{xl} in the following relationship: $\rho_{xl}\beta = \rho X$. Similarly, the gas volume fraction α and the mass fraction of exsolved gas are related by: $\rho_g\alpha = \rho n$. The mass concentration of dissolved gas c_g then takes the form:

$$c_g = (1-\chi-n)sp^m \tag{4.9}$$

Burnham (1975) found that $m = \frac{1}{2}$ is appropriate for water dissolved in silicate melts. The solubility coefficient s depends only on temperature. Crystallization is driven by decompression; s is therefore taken to be constant. The saturation pressure is that necessary to dissolve the total mass of water present in the magma. Exsolution begins when the saturation pressure exceeds the local magma pressure. The density of the gas inside bubbles ρ_g is governed by the ideal gas law and depends on the magma pressure p, the magma temperature in degrees Kelvin T and the gas constant divided by the molecular weight of water R_{gas}. It takes the form:

$$\rho_g = p/R_{gas}T. \tag{4.10}$$

As magma decompresses there are three processes that strongly influence the bulk density, especially at shallow depths, if no gas is permitted to escape the conduit. First, decompression decreases the amount of water that can dissolve in the melt, driving the

exsolution of bubbles, which have a much lower density than the magma. Secondly, decompression induces expansion of existing bubbles, which further decreases the bulk density. Finally, the exsolution of water raises the solidus of the melt, inducing crystallization. This results in an increase in crystal mass fraction, which, together with the increase in bubble mass fraction, decreases the amount of melt available for water dissolution, thus driving further exsolution.

Quantifying decompression crystallization

Prior models have treated decompression crystallization differently. Diller et al. (2006), assume an isocrystalline magma; viscosity increases result from exsolution of dissolved water in the melt. Melnik and Sparks (1999) use an empirical expression for crystallization that produces pressure gradients capable of explaining the observed dome growth at Soufrière Hills. Melnik and Sparks (2005) used empirical fits to laboratory decompression experiments. Here the evolution of crystallization is constrained from thermodynamic modeling results using the pMELTS software package (Ghiorso et al., 2002). Isentropic decompression experiments were conducted using the chemical composition published in Pallister et al. (2009), which represents an average composition for dacite samples collected from spines 4-7, with an appropriate amount of water added. Imposing an isentropic constraint allows determination of the temperature increase resulting from latent heat release. The experiments found a ~2 °C increase in temperature for each 1% increase in crystal mass fraction. This is consistent with the ratios of latent heat to specific heat for the major minerals found in dacite samples.

As a comparison to the results of modeling with pMELTS, the results of slow decompression experiments on dacite samples at temperatures of interest from Couch et al. (2003a; 2003b) and Rutherford and Hammer (2002) are used to quantify decompression crystallization. A discussion of this appears in Chapter 5.

Liquid and bulk magma viscosity

The viscosity of the melt is calculated according to the model of Hui and Zhang (2007). According to this model, the viscosity of the liquid phase is dependent on temperature, relative amounts of oxides, and dissolved water concentration. As crystal volume fraction increases it begins to have a strong influence on bulk magma viscosity because of interactions between crystals. Roscoe (1952) proposed that the relative effect of crystals should depend on some critical volume fraction β_{cr}, above which the magma is locked up and does not flow, and an empirical exponent, in the form:

$$\eta = \eta_{melt} \ (1 - \beta/\beta_{cr})^b \qquad\qquad (4.11)$$

Lejeune and Richet (1995) found the best fits to their experimental data with $\beta_{cr} = 0.6$ and $b = -2.5$. My model initially explored the use of this parameterization but encountered problems with viscosities approaching infinity at high crystal volume fractions. In the case of plug extrusion at Mount St. Helens it is contextually impractical to have no limit on the bulk viscosity because once crystals become sufficiently locked up, the stress is transmitted to the plug - conduit wall margin, and, even if after some

pause, the motion of the magma continues. The structure of the material changes from that of a crystal-rich fluid to a crystal framework with interstitial melt but similar driving stresses result in motion in both cases. For this reason I used the model of Costa (2007) to calculate bulk viscosity. The model is consistent with experimental observations that a limit on bulk viscosity exists and occurs when strain is accommodated by brittle failure instead of by viscous flow. The model takes an Error function form with respect to crystal content and results in three regimes. At low crystal volume fractions the increase in viscosity is nearly linear. At values closer to the critical volume fraction the increase in viscosity becomes exponential, resembling the model and fitting the data of Lejeune and Richet (1995). At crystal volume fractions in excess of β_{cr} the viscosity is constant and equal to η_{max}. This form is similar to the empirical viscosity equation derived by Melnik and Sparks (1999), who use an inverse tangent form to account for the rheological transition from viscous magma flow to dome building. Costa (2007) suggests that for brittle failure, η_{max} represents an effective viscosity, which can be approximated by the ratio of the differential stress and the strain rate.

CHAPTER V

MODELING RESULTS

The properties of magma at the base of the plug can influence the eruptive behavior. This chapter presents the results of modeling the evolution of magma properties over the height of the conduit. Section 5.1 examines sensitivity of model predictions based on various magma and conduit parameters using a simple degassing law, in which the lateral permeability is bimodal (zero or non-zero, depending on whether the bubble connectivity threshold has been met). Section 2 introduces the effect of vertical gas flux, which is not considered in Section 1. Finally, Section 3 discusses implications for extrusive behavior, and, more specifically, the potential for plug extrusion to generate seismicity, as suggested by SPASM.

Results with a simple degassing model

To test the conduit model, I initially consider a base case in which the conduit is sealed to gas flux (*klat* = 0). Petrologic analyses of dome samples suggest the pressure, water concentration and temperature at the top of the magma chamber were 130 MPa, 5% and 850 °C, respectively (Pallister et al., 2009; Rutherford et al., 2009). These are treated as nominal initial magma conditions. Measurements reported by Cashman et al. (2009) and made independently on different samples during this project constrain porosity at the top of the conduit to less than 10%, though the latter samples tended to originate from the gouge zone and the intact dome rock likely has a lower porosity still, probably of a few percent. SPASM requires a magma pressure of about 13 MPa at the base of the 500 m-

thick plug. While this constraint is specific to SPASM, I recognize that magma pressure at the top of the conduit cannot substantially exceed lithostatic values (11.5 MPa for a 500 m thick plug with 10% porosity). Nominal values for the conduit height H, and conduit radius R are 5.4 km and 100 m, respectively. Figure 5.1 displays the results of the base case.

The gas volume fraction becomes substantial (> 10s of per cent) near the top of the conduit owing to accelerating exsolution and expansion of existing bubbles. The elevated gas volume fraction over the entire height of the conduit results in a lower bulk magma density ρ and, therefore, a diminished pressure gradient. These processes result in a final magma porosity of 50% and a pressure of 49.0 MPa, both of which are substantially higher than the constraints for those values (a few per cent and ~12 MPa, respectively).

The base case results confirm that degassing must be an important process in the conduit.

To evaluate its effect I employ a simple degassing model in which lateral permeability k_{lat} is constant once the bubble connectivity threshold α_{crit} is met. The nominal value used for this threshold is 60%. (Below this threshold the permeability is 0.) Permeability values range from 0 to 10^{-14} m^2. Figures 5.2 and 5.3 show the results for the lateral permeabilities of 10^{-15} m^2, 10^{-16} m^2 and 10^{-17} m^2. The plots of pressure and gas volume fraction resemble those of the base case until the connectivity threshold is met and degassing begins at a depth of approximately 1500 m. The gas volume fraction begins to drop off at a rate controlled by the lateral permeability. At a permeability of 10^{-17} m^2
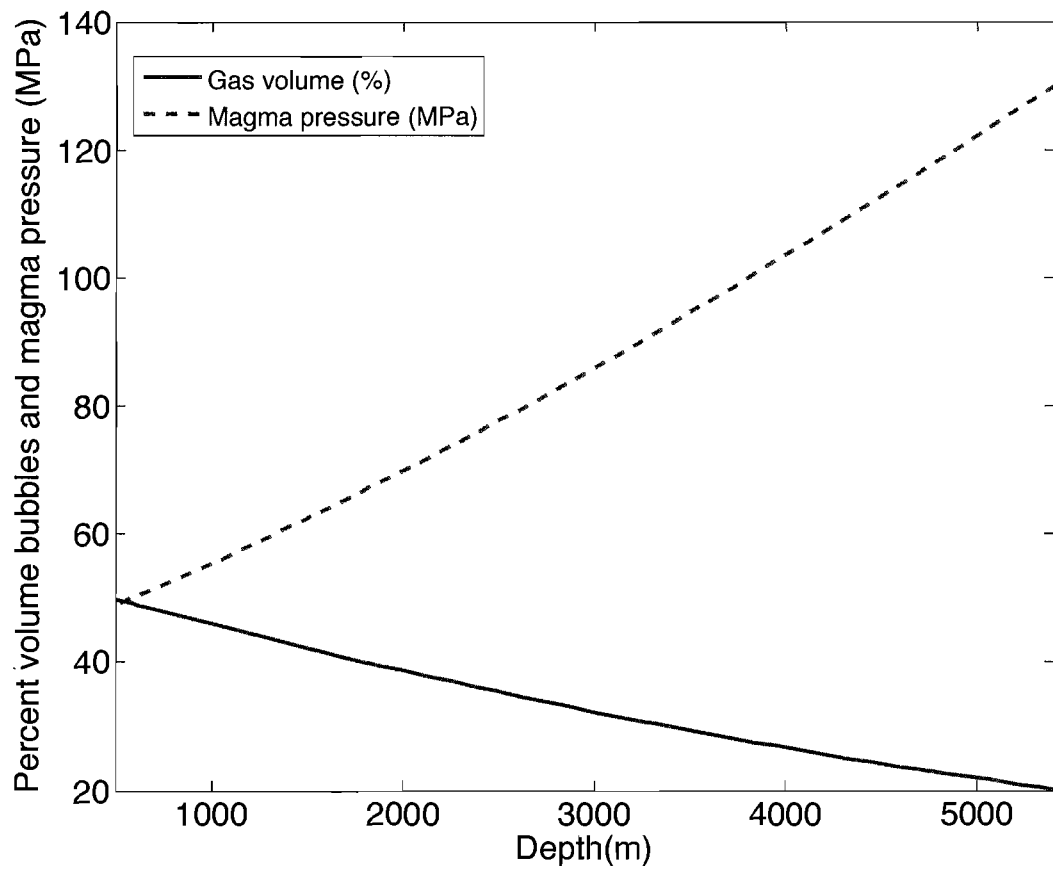
Figure 5.1 The model predicts that for the base case, in which the conduit is sealed and

no degassing occurs, the resulting plug base pressure and porosity are ~50 MPa and
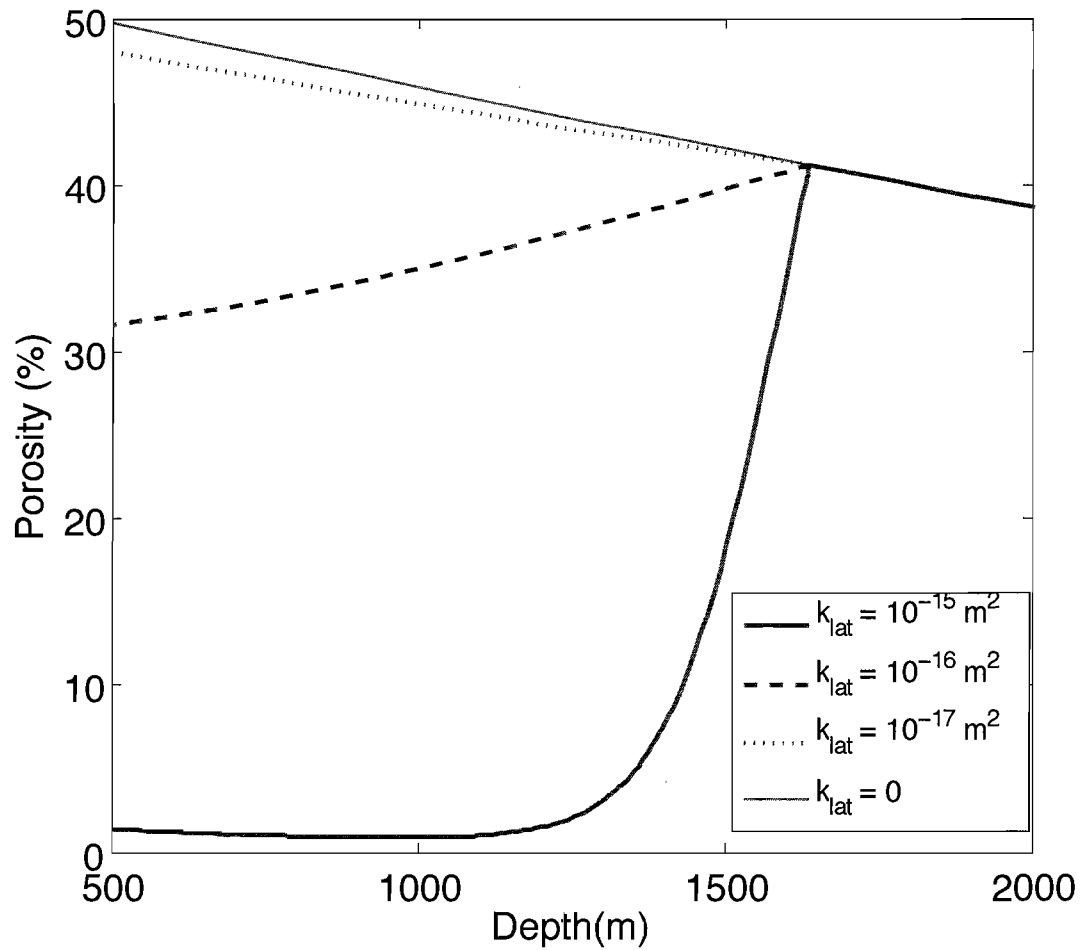
~50% by volume.

Figure 5.2 Degassing becomes more influential as the lateral permeability increases. The range in effect is large for a range in permeabilities between 10-17 m2 and 10-15 m2. Note the x-axis extends only to a depth of 2000 m (the conduit base is at 5.4 km).
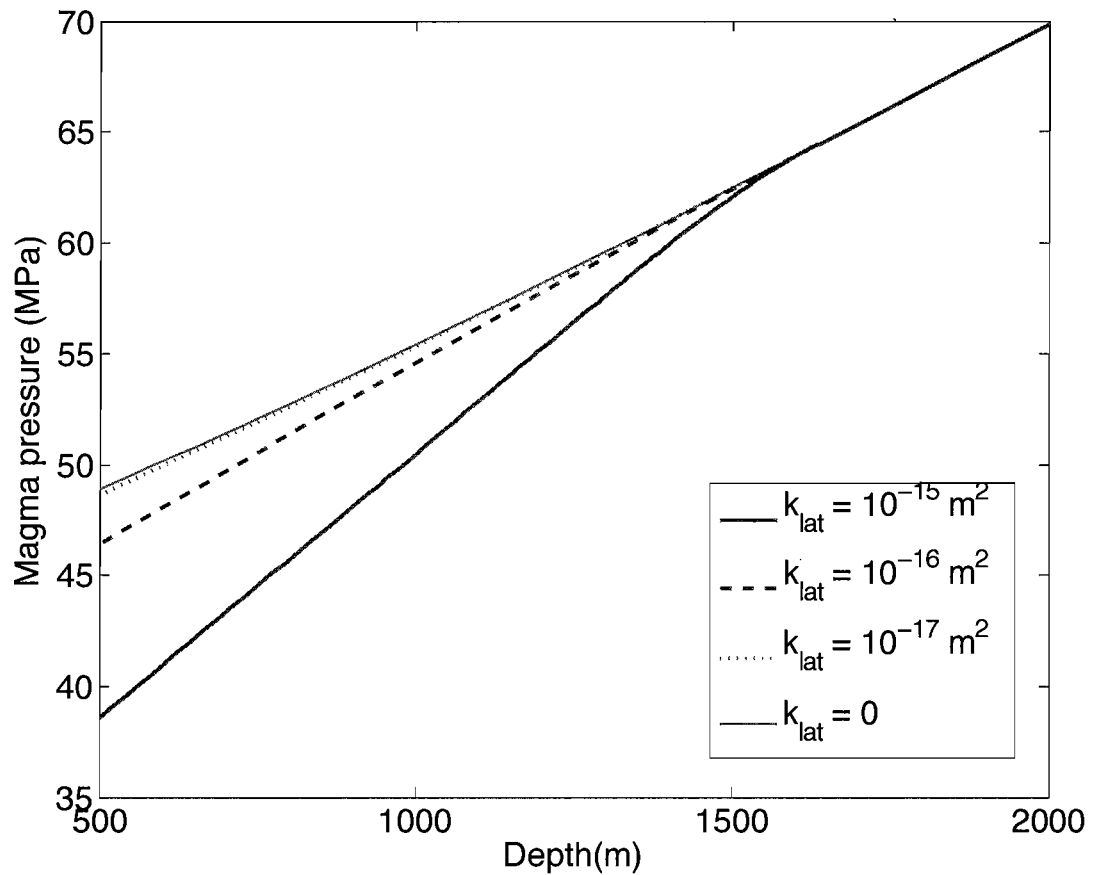
Figure 5.3 Degassing influences the plug base magma pressure by influencing the

pressure gradient magnitude. More porous magma is less dense. The resulting pressure

gradient is lower and the plug base pressure is elevated.

there is almost no effect on the gas volume fraction, and the final porosity is 48%, almost the same as the base case. At a permeability of 10^{-16} m^2 degassing has a small effect on the gas volume fraction and the final porosity is 32%. At a permeability of 10^{-15} m^2 there is a more pronounced effect and degassing effectively removes almost all gas from the magma for the remaining portion of the conduit. While the gas volume fraction plot suggests that permeability values between 10^{-15} m^2 and 10^{-16} m^2 would yield the measured porosity values of < 10%, the resulting final pressure value from any of the three cases is at least 25 MPa higher than expected values. Lateral permeability values of 10^{-15} m^2, 10^{-16} m^2 and 10^{-17} m^2 result in pressures at a depth of 500 m of 38 MPa, 47 MPa and 48.5 MPa, respectively.

Next, I address the sensitivity of the simple degassing model to variations in initial magma pressure, water concentration, temperature, vertical permeability, bubble connectivity threshold and conduit geometry. As discussed below, a bimodal permeability condition (where it is either zero or non-zero) cannot adequately model both the final porosity and pressure values using independently- constrained values for conduit and magma parameters. This suggests a more complex degassing model is necessary. All sensitivity tests described below use the nominal values listed in Table 4.1 with the exception of the parameter being tested. Each parameter test involves several runs, each corresponding to a different lateral permeability value.
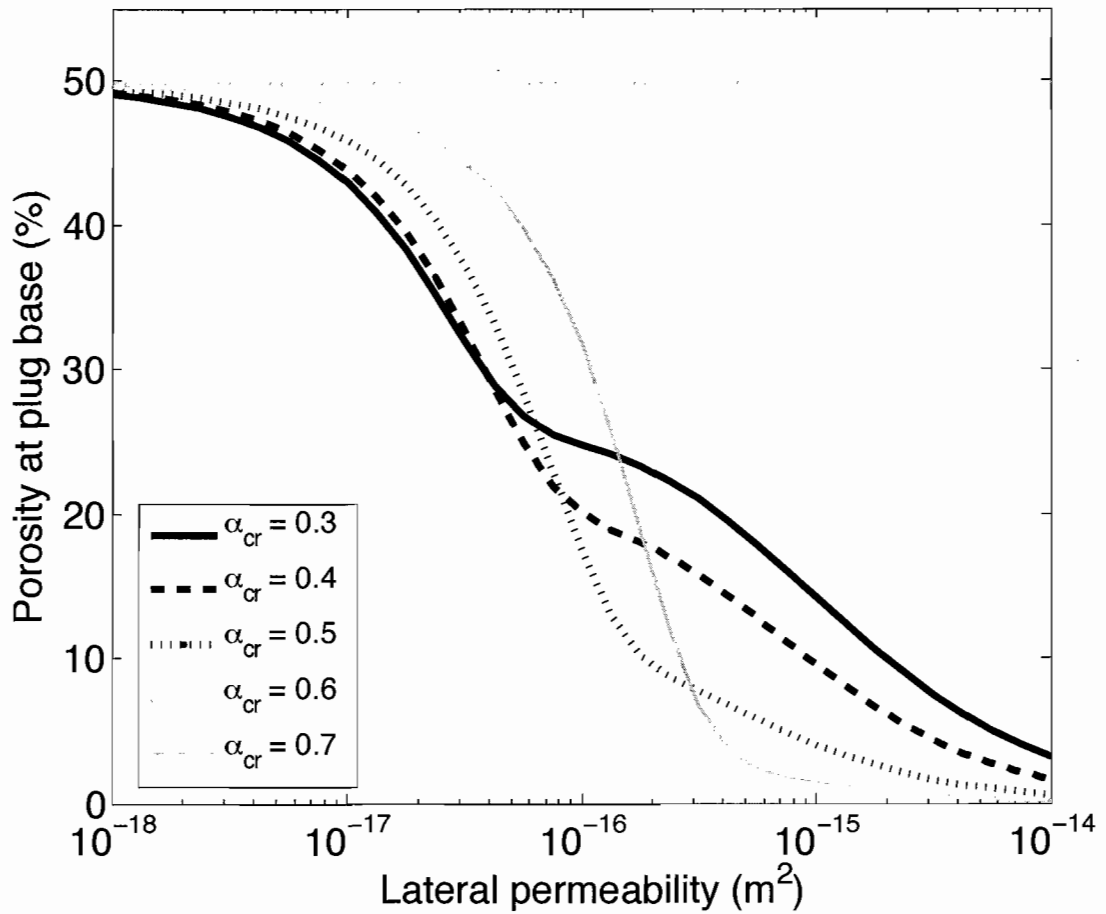
Figure 5.4 The bubble connectivity threshold is not attained under nominal conditions

when it is at or above 70%. For lesser values of the threshold, the effect is subtle when

degassing is either strong or weak, but for intermediate values the exact effect depends on

the specific value of the lateral permeability.

The effect of the bubble connectivity threshold

Figure 5.4 shows the sensitivity of the final porosity to the bubble connectivity threshold over a range from 30% to 70% (recall that this threshold is the ratio of gas volume to the volume of gas and melt). The depth at which degassing begins is largely dependent on this value. The effect is varied because, for a given lateral permeability, the rate of degassing Q is scaled by the local gas volume fraction. For example, a lateral permeability of 10^{-15} m^2 that results in efficient degassing over much of the conduit yields a lower degassing rate when the magma is 3% gas by volume than does a lateral permeability of 10^{-16} m^2 with magma of 40% porosity. (Recall that once bubble connectivity is established it is assumed to be maintained even if α drops below α_{crit}.) For lateral permeabilties lower than about 10^{-17} m^2, and for permeabilities greater than about 4×10^{-15} m^2, the effect of the critical bubble connectivity threshold is subtle. Generally, when degassing is weak, the final magma porosity is high and when it is prominent, the porosity is low regardless of the threshold. An exception occurs when the threshold is at or above 70%. The plug base magma porosity is unaffected by degassing, indicating the volume of gas never exceeds 70% of the combined volume of gas and melt under the nominal conditions. For intermediate values of lateral permeability, however, the effect of the connectivity threshold depends on the specific value of permeability. Figure 5.4 illustrates this point by showing that the lowest plug base porosity is attained with a threshold of 30%, 40%, 50% and 60% when the lateral permeability is 2×10^{-17} m^2, 6×10^{-17} m^2, 2×10^{-16} m^2 and 6×10^{-16} m^2, respectively.
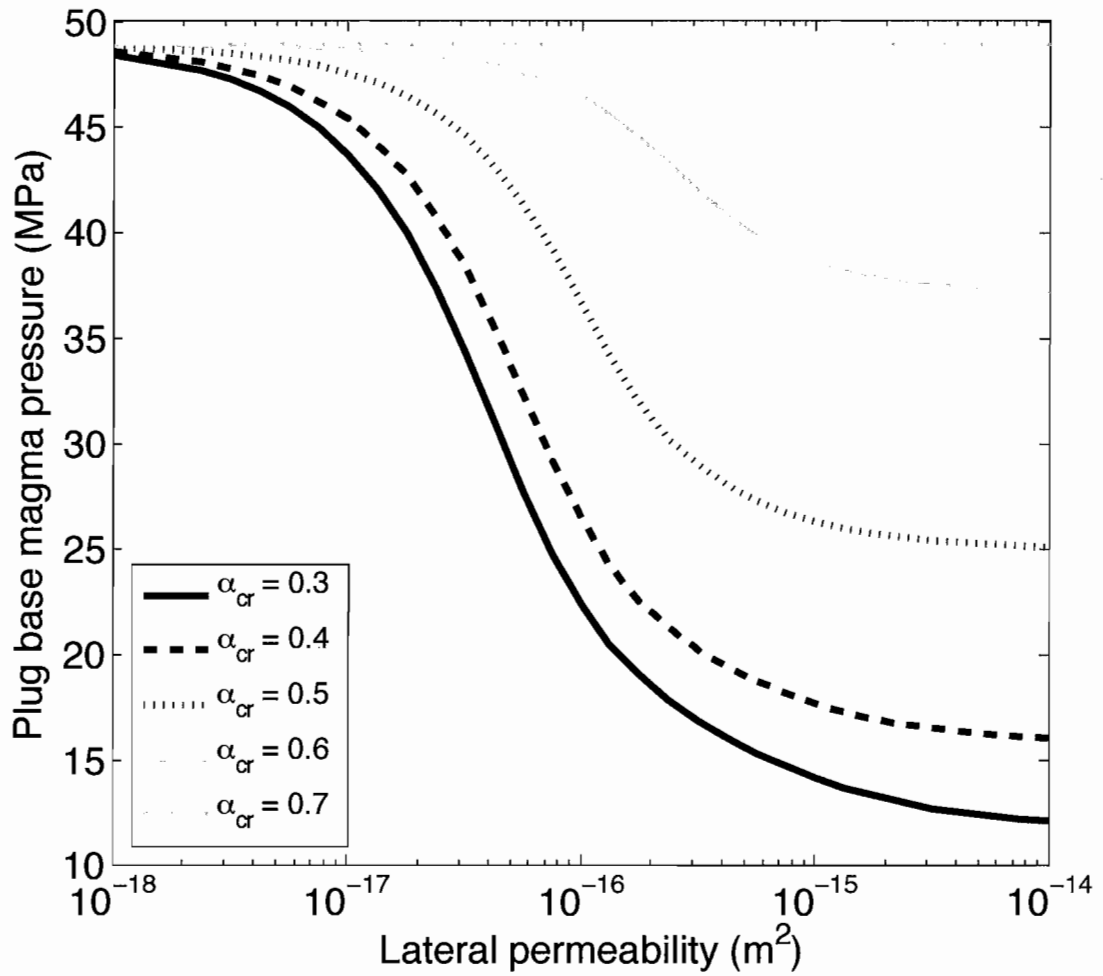
Figure 5.5 Degassing decreases the plug base magma pressure. The effect is more pronounced when the connectivity threshold is lower.

Figure 5.5 shows the effect of bubble connectivity threshold on the plug base magma pressure. When the threshold is at or above 70% the threshold is not met, and the resulting pressure at the top of the conduit is unaffected. For values between 30% and 60%, however, lower thresholds yield lower plug base pressures for a given lateral permeability. Magma attains lower connectivity thresholds at deeper depths in the conduit. This increases the depth range over which dense magma occupies the conduit, and the elevated pressure gradient magnitude accordingly acts over this increased depth range, yielding diminished basal plug pressures. For example, the difference in pressure between the weak degassing limit ($k_{lat} = 10^{-18}$ m^2) and the strong degassing limit ($k_{lat} = 10^{-14}$ m^2) is 35 MPa for a threshold of 30% whereas the difference is only 10 MPa for a threshold of 60%.

The effect of initial magma pressure

At low lateral permeabilites, less than about 3×10^{-17} m^2, degassing is negligible and variations in initial magma pressure at the conduit base yield a predictable trend (Figure 5.6). Lower initial magma pressures result in higher plug base magma porosities. This results from the fact that when the magma pressure is lower crystallization is more advanced and there is less melt available for dissolution relative to magma at higher pressure. Moreover, gas solubility is lower at lower pressures, and these two processes act in concert to generate higher porosity magma at the conduit base. Because degassing is negligible the gas volume fraction evolves only by increasing. As the lateral permeability increases degassing becomes more influential and when the initial magma
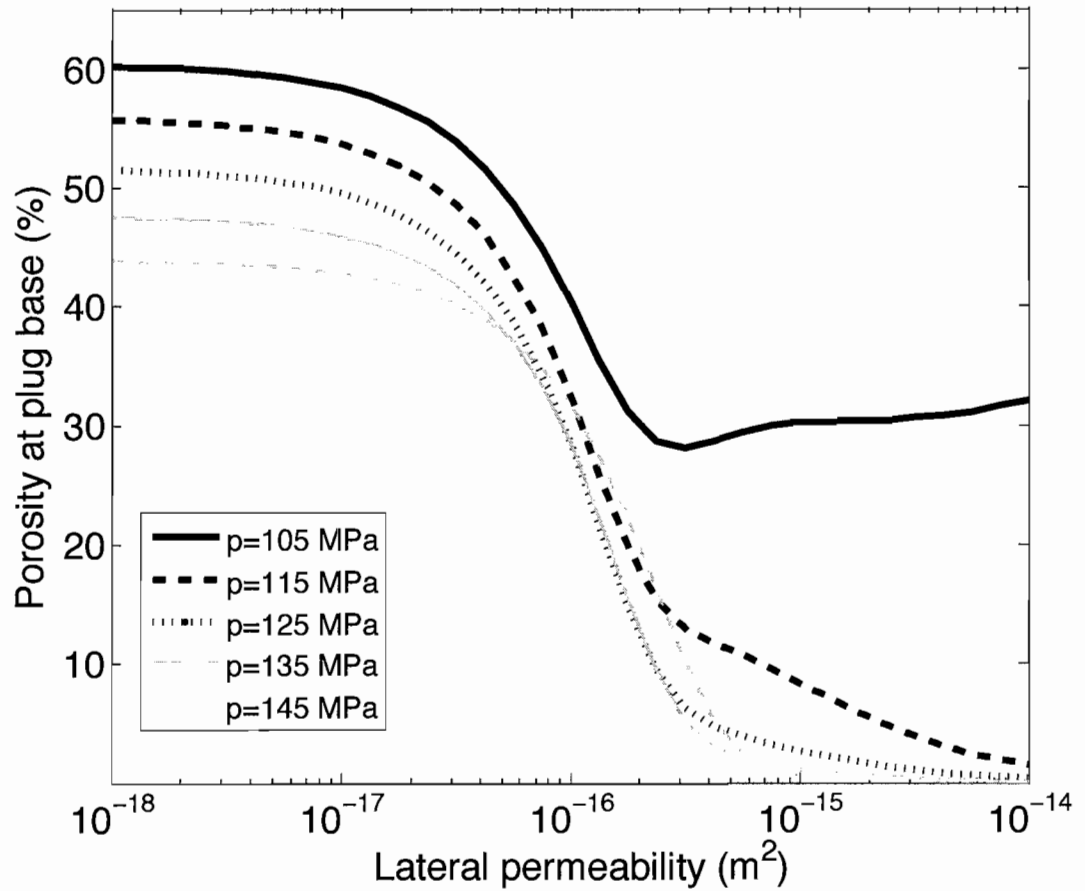
Figure 5.6 Variations in initial magma pressure have a minimal effect on plug porosity when the lateral permeability is above about 10^{-15} m², except when the initial magma pressure is low (~105 MPa). At lower lateral permeability values increased initial pressures steadily increase the plug base magma porosity.

pressure is at or above 115 MPa the resulting plug base magma porosity predictably approaches zero. Interestingly, the model predicts that for an initial magma pressure of 105 MPa, the gas volume fraction at the plug base increases slightly for permeability values higher than 3×10^{-16} m^2. Because of the elevated gas volume fraction at the conduit base when the pressure is this low the bubble connectivity is attained at a lower depth, and when the lateral permeability is high degassing is initially efficient, but then inefficient once the conduit has been degassed. The processes that increase gas volume fraction at shallow depths then dominate over the inefficient degassing, and the resulting plug base porosity is elevated. At low initial magma pressures but otherwise nominal values this indicates that a lateral permeability of 3×10^{-16} m^2 is most efficient at degassing the conduit.

Variations in initial magma pressure have a relatively simple effect on plug base magma pressure (Figure 5.7). The effect of increasing the lateral permeability tends to decrease the final pressure because degassing densifies magma and increase the pressure gradient magnitude. This effect is most pronounced when the initial magma pressure is lower. For example, an initial magma pressure of 145 MPa yields plug base pressures of about 59 MPa and about 53 MPa when degassing is respectively minimal ($k_{lat} = 10^{-18}$ m^2) or prominent ($k_{lat} = 10^{-14}$ m^2). On the other hand, when the initial magma pressure is 105 MPa, the final magma pressure ranges from about 35 MPa when degassing is negligible to about 5 MPa when it is prominent. This results from lower pressure magmas attaining
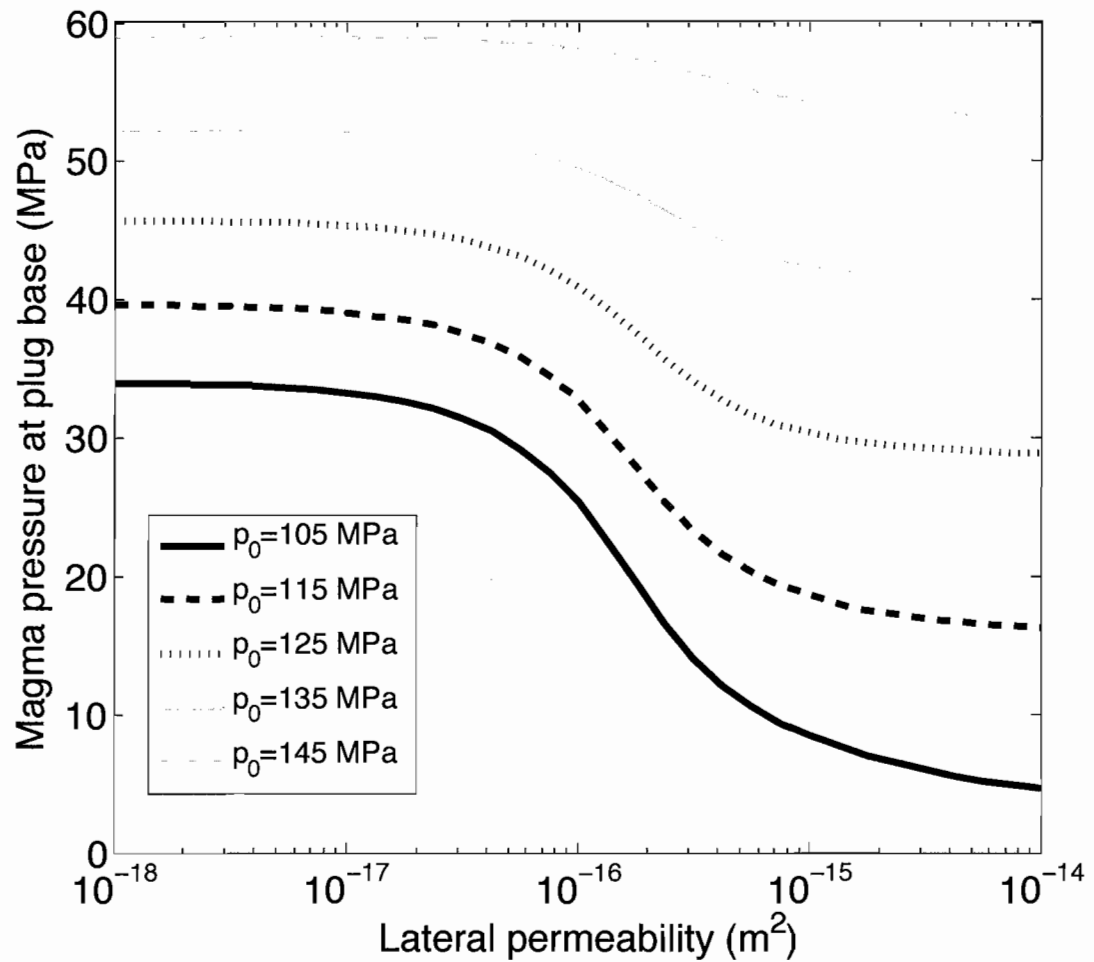
Figure 5.7 As lateral permeability increases and degassing becomes more influential the effect on the plug base pressure becomes more pronounced for lower initial magma pressures.

the bubble connectivity threshold at depth, thereby increasing the depth range over which the elevated pressure gradient magnitude acts.

The effect of conduit height

Figure 5.8 illustrates the effects of conduit height (i.e., chamber depth) on the plug base magma porosity. For low lateral permeabilities degassing is weak and variations in conduit height are more influential than effects from degassing. While the conduit height varies from 4500 m to 6500 m, the initial magma pressure is constant at the nominal value, and so the magma contains the same volume fraction of bubbles in each case. Because degassing is negligible, a taller conduit represents a longer path length for gas volume fraction to increase. As lateral permeability increases, however, the effect of degassing is varied and depends in each case on the conduit height. For a conduit height of 4500 m degassing begins to affect the plug base magma porosity only when the lateral permeability exceeds 2×10^{-16} m^2. At higher permeabilties the final porosity diminishes and approaches zero for permeabilities in excess of about 6×10^{-15} m^2. When the conduit height is 5500 m degassing becomes influential at permeability values above 10^{-17} m^2. The resulting final magma porosity diminishes until it is near zero for permeabilities greater than 10^{-15} m^2. The prediction that a conduit of 5500 m height is more sensitive to smaller permeabilities arises from the increased depth range over which degassing takes place relative to a conduit with a height of only 4500 m. At a conduit height of 6500 m the effect of degassing is similar (although it yields higher final porosities because of the longer path length) for lateral permeabilities between 2×10^{-17} m^2 and 3×10^{-16} m^2. At
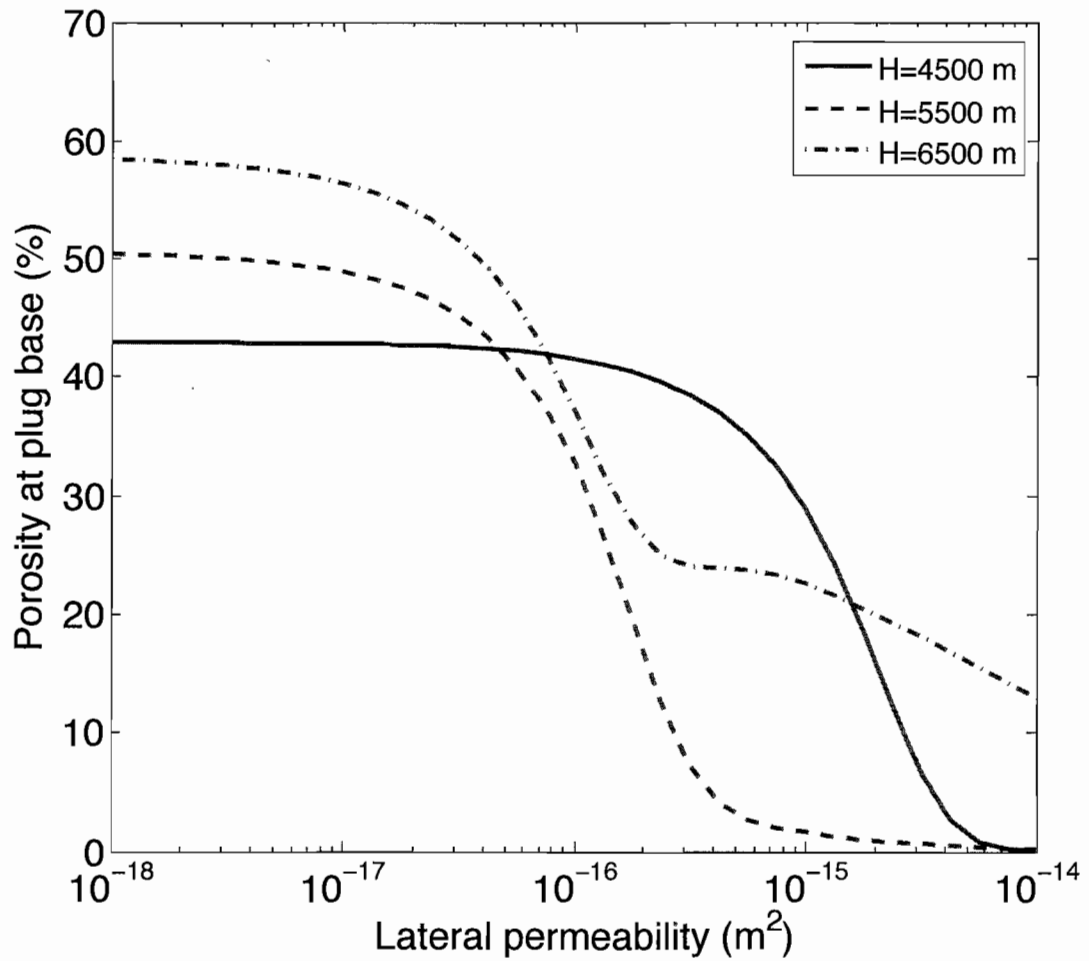
Figure 5.8 When degassing is weak an in crease in conduit height yields elevated plug base magma porosities. For permeabilities greater than about 3×10^{-17} m^2, however, a conduit height of 5500 m is the most efficient at producing low porosity magma beneath the plug.

values higher than 3×10^{-16} m^2 the final magma porosity continues to decrease, though the effect much smaller. This stems from the fact that the most efficient degassing occurring at some depth from the plug base and less efficient degassing must compete with processes tending to increase the gas volume fraction. This indicates that for the three conduit heights tested and under the nominal conditions degassing is most efficient for a height of 5500 m and yields low porosity magma in the upper conduit because efficient degassing occurs just below the plug base.

Figure 5.9 shows the predicted plug base magma pressure for the same three values of conduit height. For a height of 4500 m the base pressure is essentially unaffected for any value of lateral permeability. This indicates that the depth range over which degassing occurs is much less than the depth range over which it does not. When degassing is weak, the plug base pressure decreases owing to the longer path length over which the pressure gradient acts. At higher permeabilities, degassing yields lower plug base pressures with the effect of increasing with conduit height. This is direct consequence of the linear increase in the depth range of degassing with an increase in conduit height.

The effect of conduit radius

Changing the conduit radius has two competing influences on gas transport. A smaller radius results in larger lateral pressure gradients because the radius is the characteristic distance used to scale the difference between magmatic and hydrostatic pressures. Geometric relationships also introduce a radius term, making the degassing
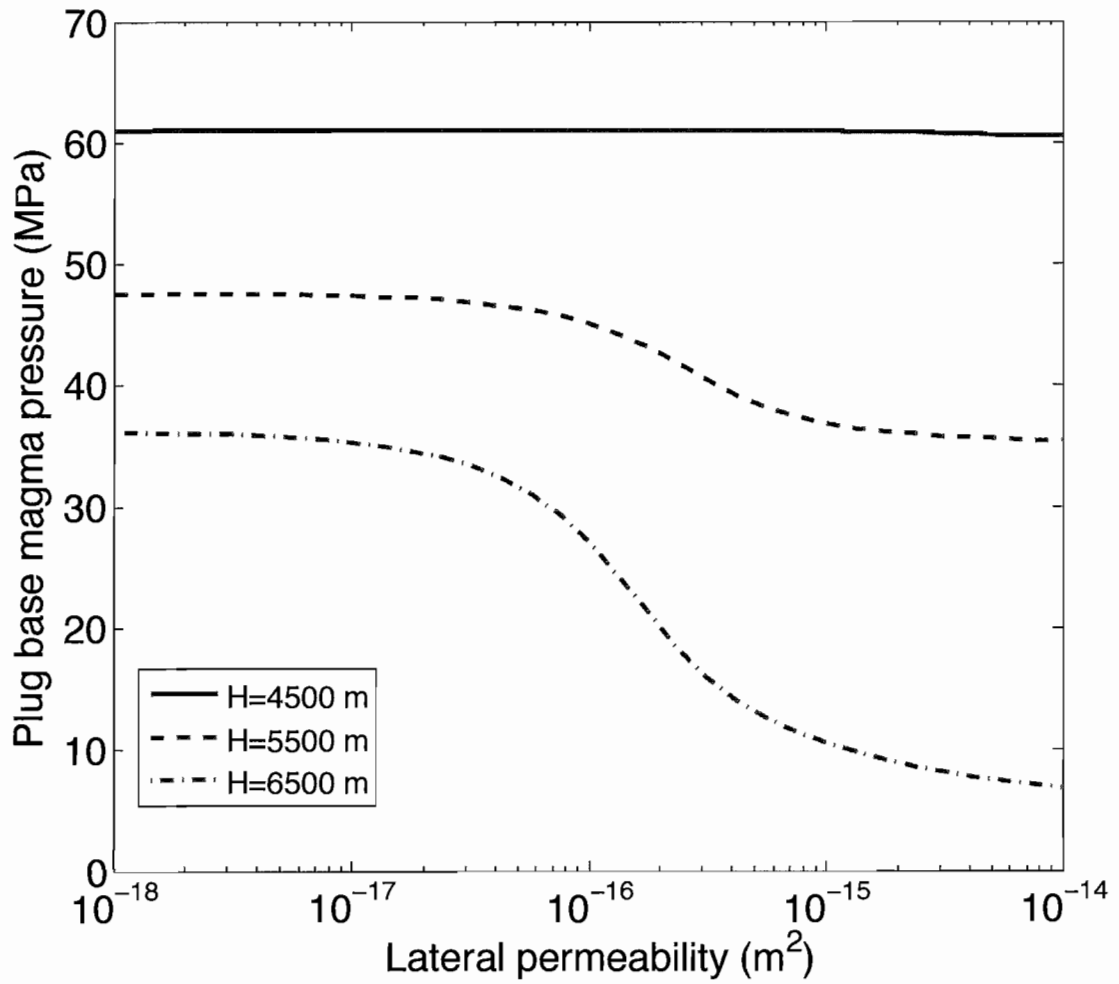
Figure 5.9 At higher permeabilities and conduit heights greater than 4500 m degassing

yields lower plug base magma pressures.

rate inversely proportional to R^2. On the other hand, to maintain a constant volumetric output of 2 m³/s, the linear magma velocity must increase to compensate for the decrease in cross sectional area, and therefore the velocity is also inversely proportional to R^2. An increased lateral pressure gradient directly increases the rate of degassing while higher magma velocities limit the time scale to degas a parcel of magma at a given depth z.

Figure 5.10 shows that these two processes tend to have equal but opposite effects on gas volume fractions because the final porosity is largely insensitive to the conduit radius for a given lateral permeability. Figure 5.11 shows a weak dependence of plug base pressure on conduit radius, but only for lateral permeabilities greater than 10^{-16} m² and for conduit radii less than 50 m. At higher permeability values and smaller radii the effect arises from the viscous term of the pressure gradient equation becoming substantial. For a constant volumetric output rate the viscous term is inversely proportional to R^4. For the nominal radius value of 100 m, the resulting linear magma velocity is of order 10^{-5} m/s. Therefore, assuming a bulk viscosity of 10^{10} Pa s, the viscous term is of order 100 Pa/m. The density term, on the other hand, is of order 10^4 Pa/m. Smaller radii (in this case, less than a few tens of meters) result in significant values of the viscous term. Higher permeabilties yield higher crystal volume fractions, which affects bulk viscosity. This suggests that for eruptions with small volumetric outputs (~1 m³/s), viscous resistance is significant only for small radii and/or high lateral permeability. This is illustrated in Figure 5.12, which shows the ratio between viscous effects and density effects on the pressure gradient. The ratio between these terms
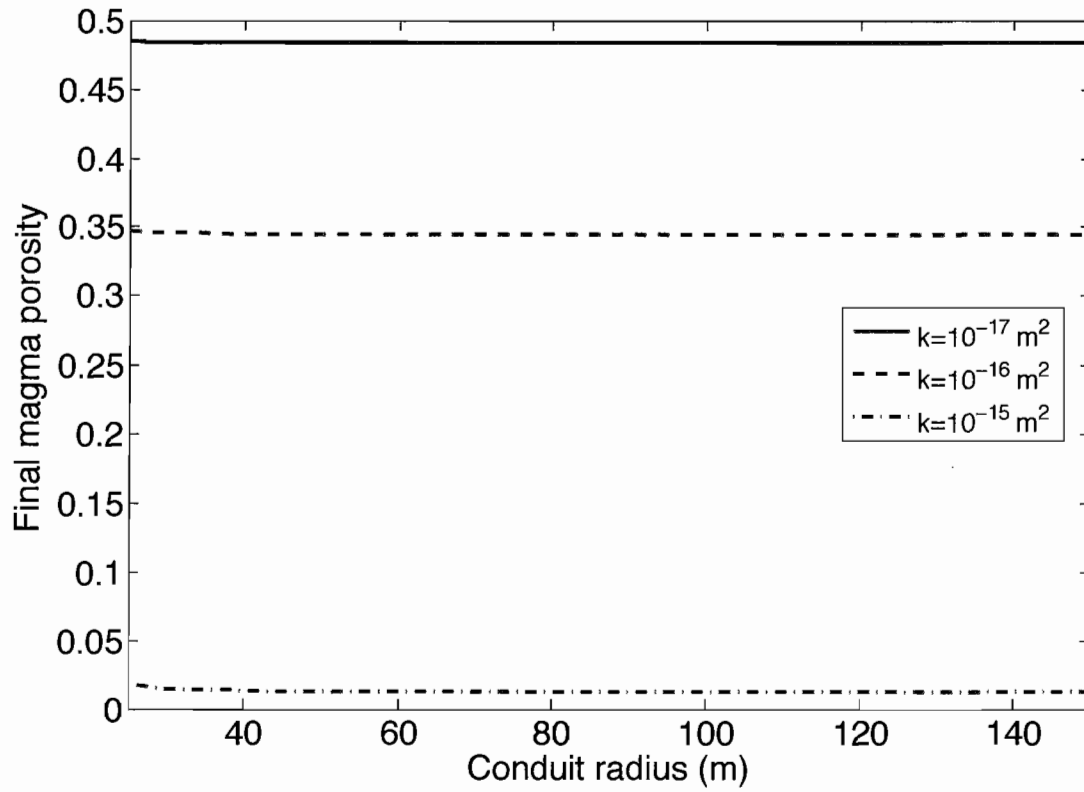
Figure 5.10 The plug base magma porosity is insensitive to variations in conduit radius

down to a value of 25 m.
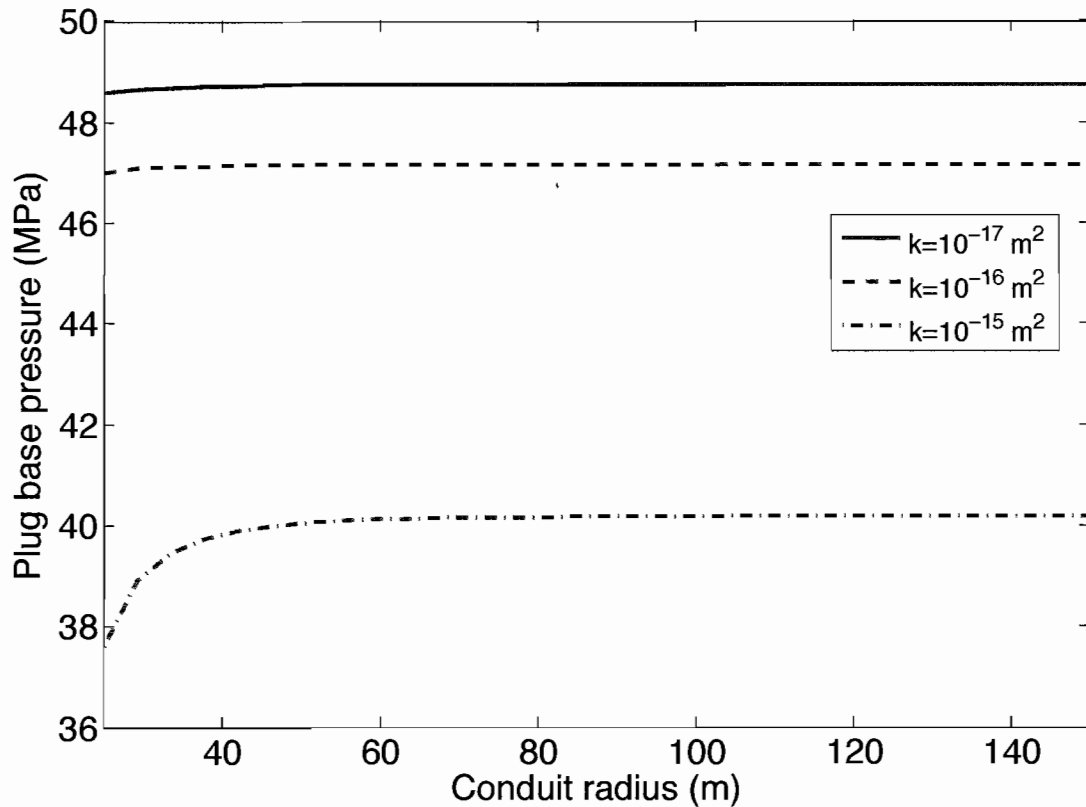
Figure 5.11 The effect of conduit radius is only significant when a combination of high lateral permeability and a small conduit radius are sufficient to generate enough viscous resistance to influence the pressure gradient magnitude. Viscous resistance is inversely proportional to R^4, and higher permeabilities yield increased crystal volume fractions.

reaches unity near the top of the conduit only when the conduit radius is about 10 m.

One interpretation of this is that steady effusive eruptions with low volumetric output

rates have some combination of conduit radius and permeabiltity values that generate the

minimum viscous resistance, which is itself dependent on velocity and therefore rate

limiting. Conduit radius is not expected to change appreciably over time when the

magma flux is low, and so this implies that time dependent changes in degassing behavior

are more likely the cause for eruptions to either halt (depressurization) or increase in flux

(repressurization) when all other properties remain the same.

The effect of initial water concentration

Figure 5.13 shows that for low lateral permeability values ($< 10^{-17}$ m^2), the

effect of degassing is small and that there is a direct relationship between higher initial

water concentrations and higher magma porosities at the plug base. When the lateral

permeability is greater than about 4 x 10^{-15} m^2 the plug base magma porosity is near zero

for any initial concentration of water between 3% and 7% by weight. For intermediate

values, however, higher water concentrations result in lower final magma porosities.

This is slightly counterintuitive, but results from variations in the depth at which the

bubble connectivity threshold is attained. For example, a melt with 3-7% water is

saturated at the base of the conduit. Any water in excess must be present as bubbles, and

so a melt with 7% water has more exsolved gas by volume at the conduit base. This

effect is illustrated in Figure 5.14, which shows that source magmas with 3% and 7%

water by weight have conduit base porosities of 5% and 32%, respectively. A higher
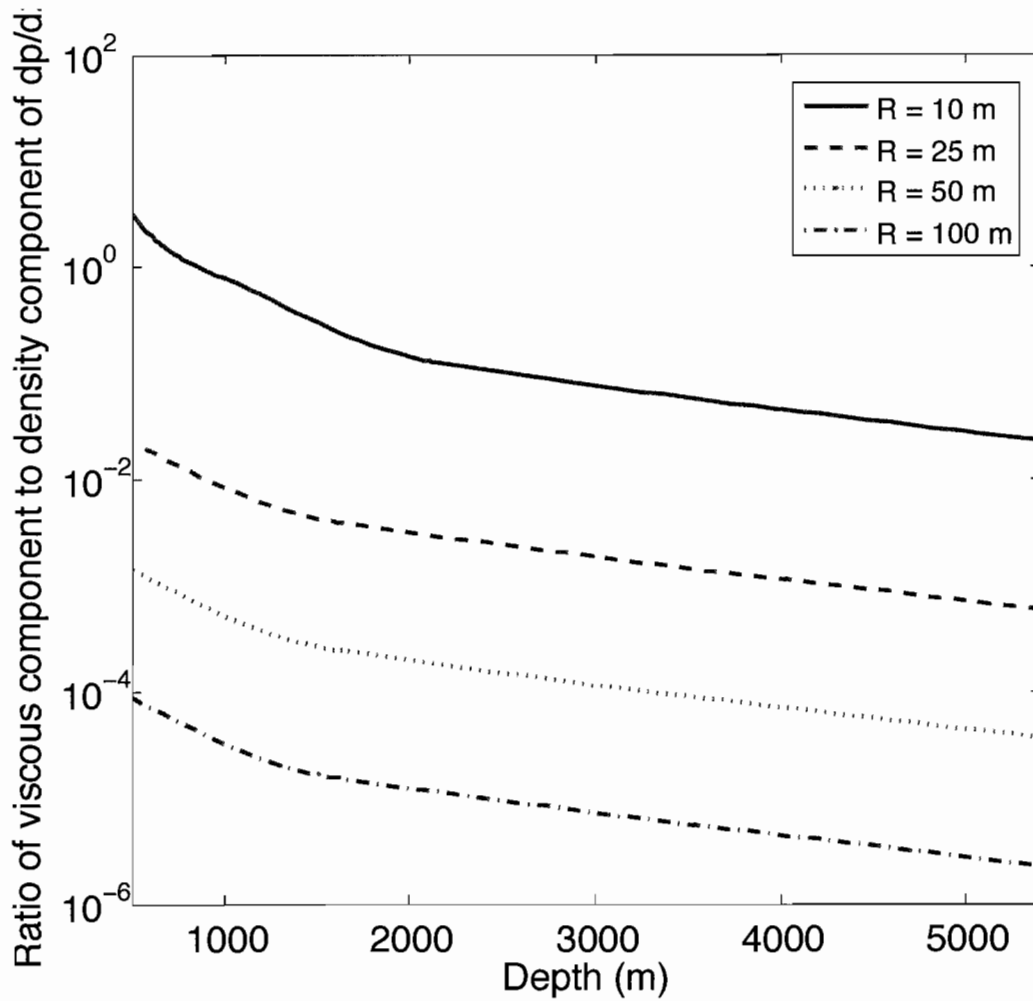
Figure 5.12 The ratio of viscous to density terms of the pressure gradient equation for a lateral permeability of 10^{-16} m². The viscous term is of the same order as the density term only when the conduit is about 10 m in radius and when the magma is less than ~500 m below the plug base.
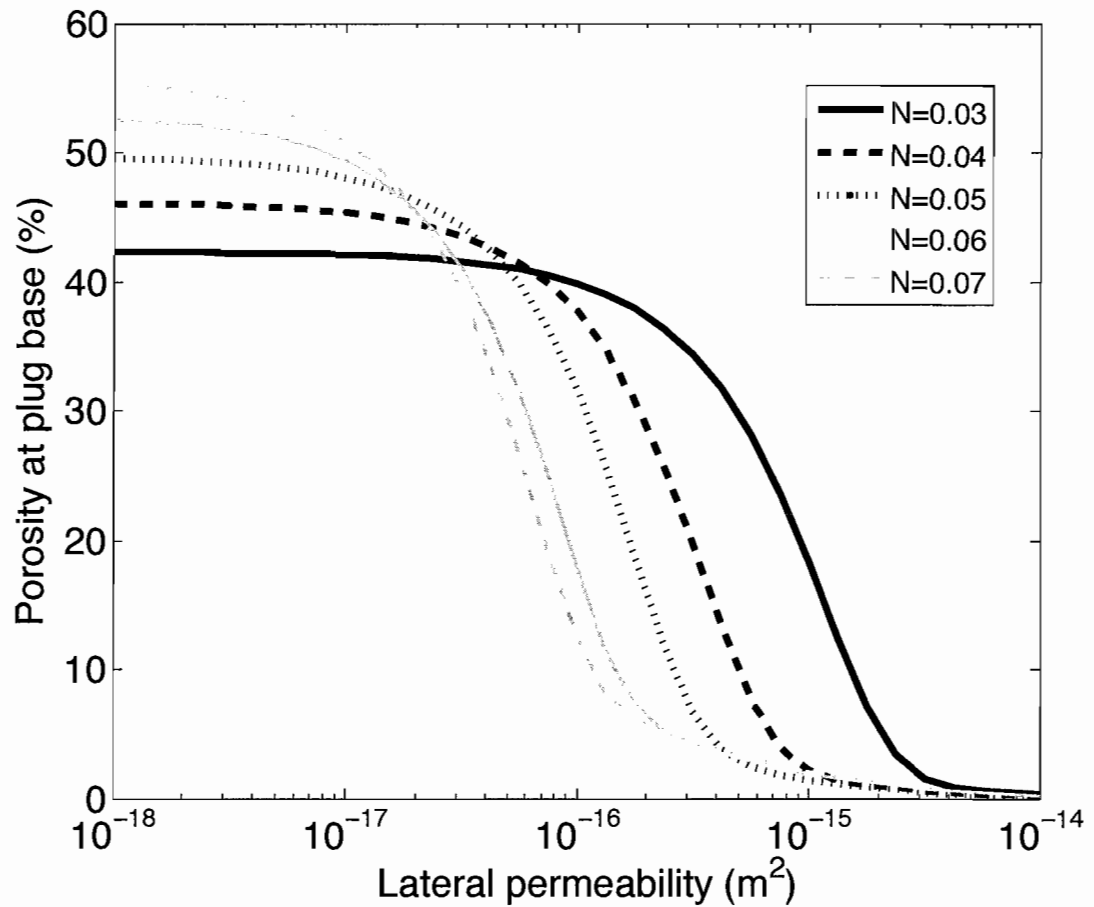
Figure 5.13 The effect of source magma water concentration on plug base magma porosity. For lateral permeability values greater than about 10^{-16} m^2 higher intitial water concentrations yield lower final porosities.
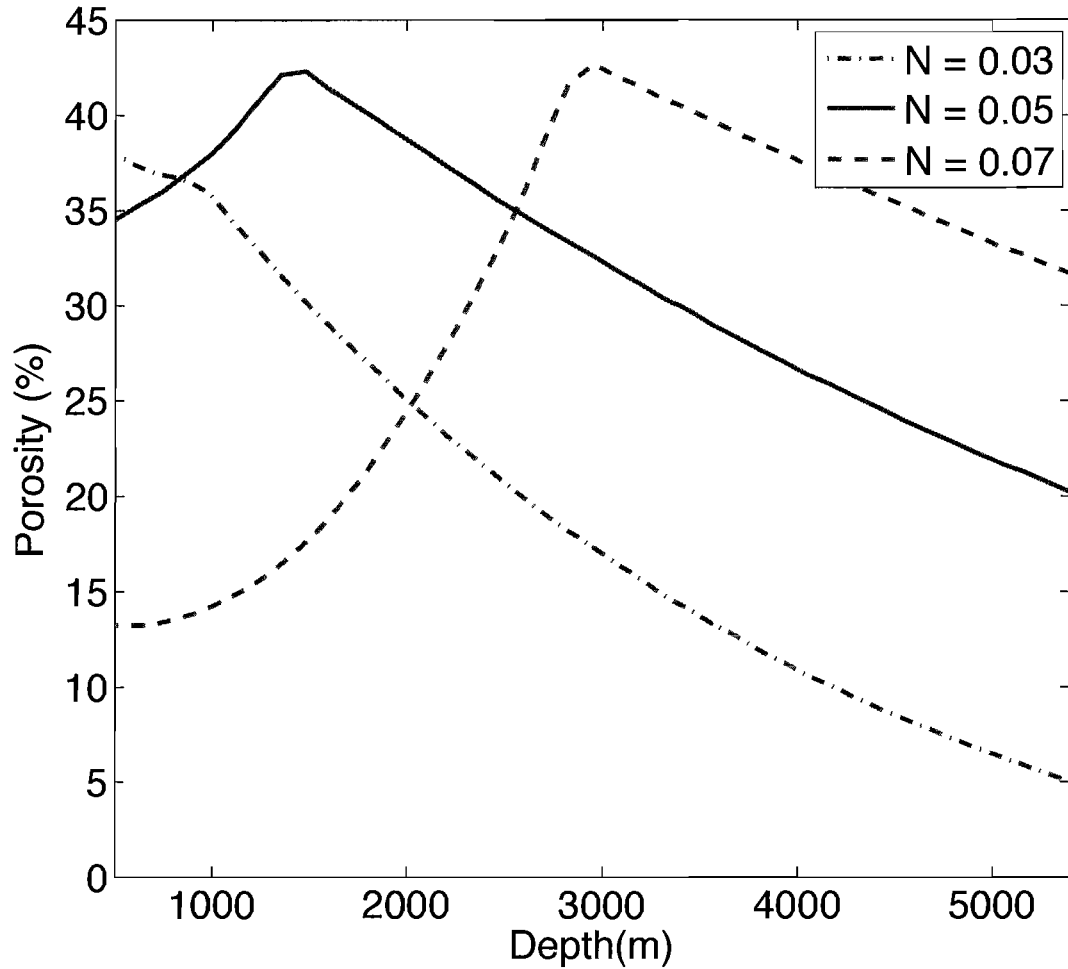
Figure 5.14 The evolution of gas volume fraction over the conduit height for three different initial water conditions. The lateral permeability is 10^{-16} m^2. Higher initial water concentrations attain the bubble connectivity threshold at a lower depth, and so degassing acts over a longer depth range resulting in diminished final porosity values.

initial porosity results in a deeper degassing depth; and diminished final porosities; this is also illustrated in figure 5.14. For lateral permeabilities less than about 10^{-17} m^2 there is little effect of degassing, and the plug base pressure increases as water concentration increases (by about 5 MPa for each 1% water by weight; Figure 5.15). For larger lateral permeability values, however, the effects ultimately depend on the average gas volume fraction over the conduit height. Lower average values produce dense magmas, increased pressure gradients and lower plug base pressures. Higher average porosity values result in elevated plug base pressures. The highest plug base pressure is attained when the magma initially contains 5% water and lower pressures result for higher or lower concentrations. The degassing depth affects the conduit height-averaged gas volume fraction. Although lower gas volume fractions would be expected to generate larger bulk viscosities and increase the magnitude of the pressure gradient, for a radius of 100 m and the slow magma ascent velocity, the density term is typically orders of magnitude larger than the viscous term. This is illustrated in Figure 5.16, which shows that the ratio of the viscous term to the density term of the pressure gradient is less than 10^{-4}.

The effect of the pressure-crystallization relationship

Figure 5.17 illustrates the effect of the pressure-crystallization relationship on the plug base porosity. The series includes thermodynamic modeling results using pMELTS (Ghiorso et al, 2002) as well as results from several slow decompression crystallization experiments conducted on dacites (Hammer and Rutherford, 2002; Couch et al., 2003a; Couch et al. 2003b). Thermodynamic modeling with pMELTS was conducted at 775 °C,
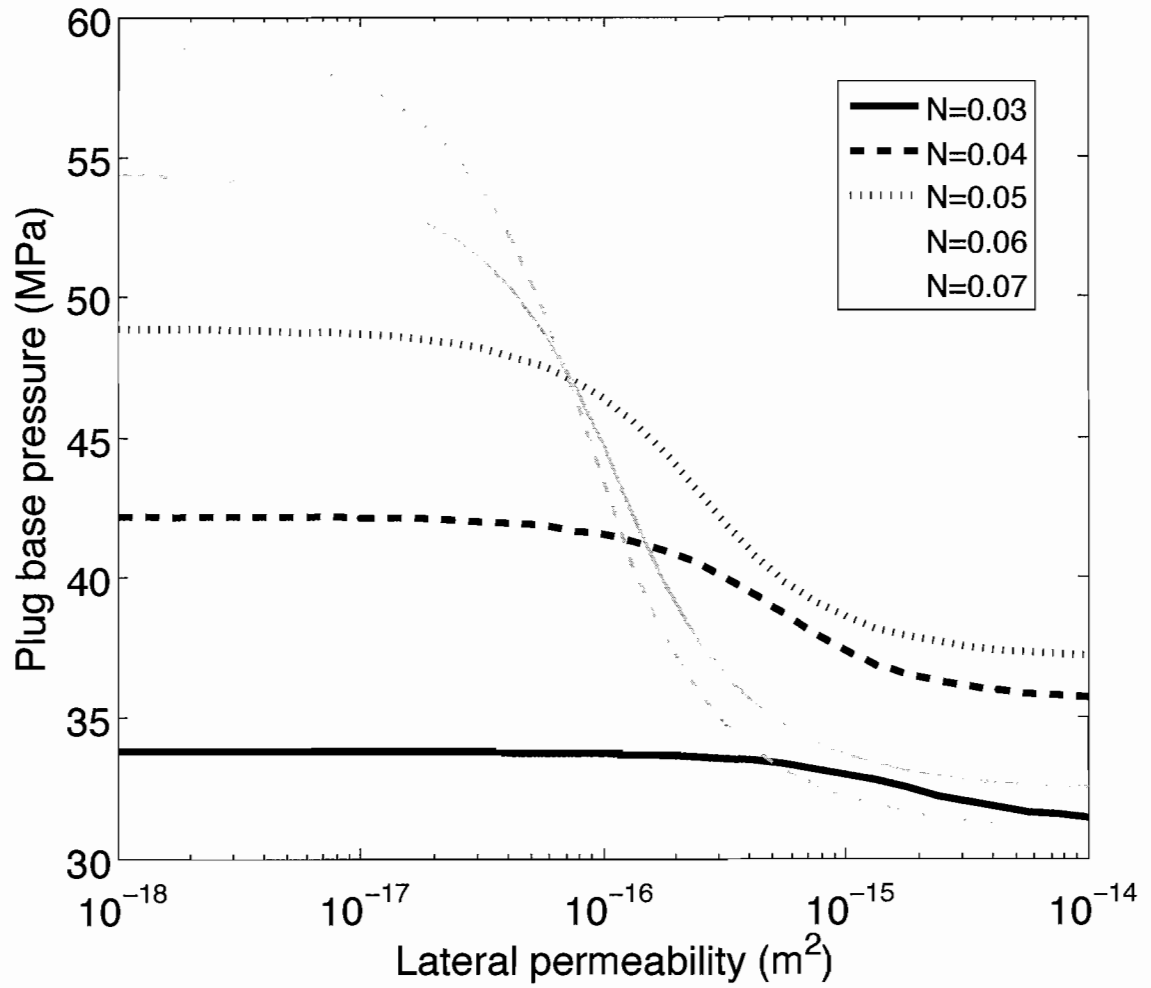
Figure 5.15 The resulting plug base pressure for a range of source magma water

concentrations by weight. A concentration of 5% yields the highest final magma

pressure.
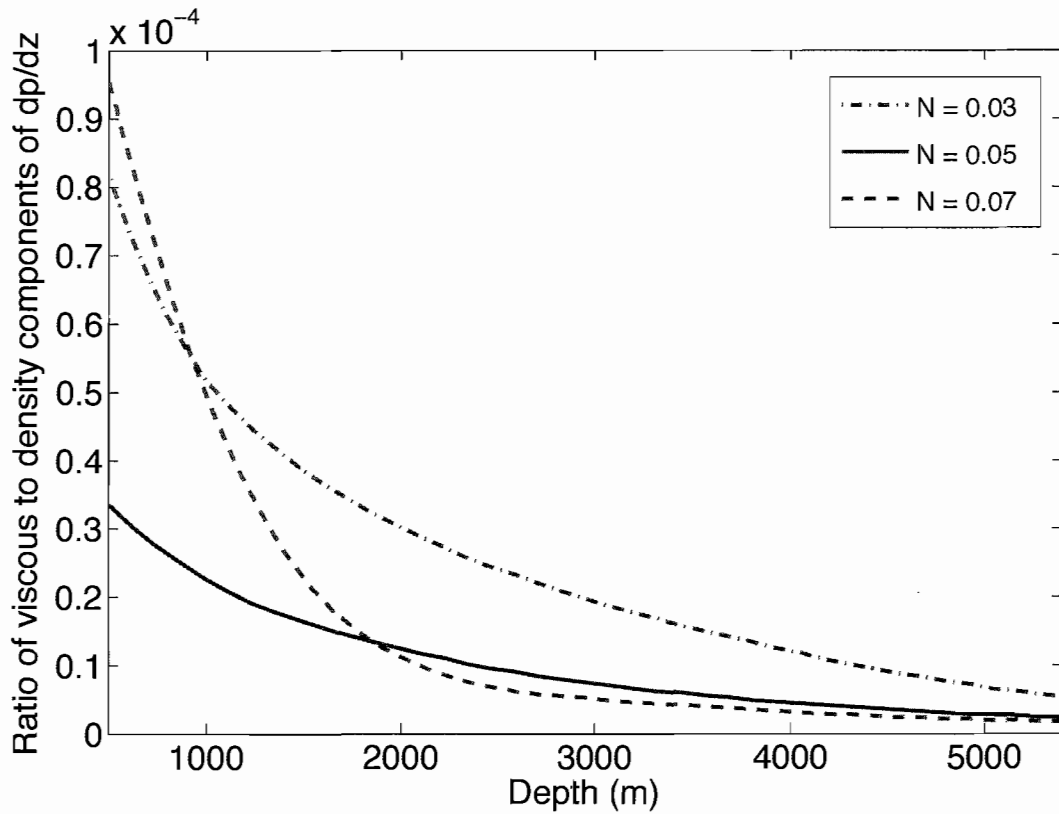
Figure 5.16 The ratio of density and viscous effects on the magma pressure gradient when the lateral permeability is intermediate, in this case 10^{-16} m^2. The density term dominates.
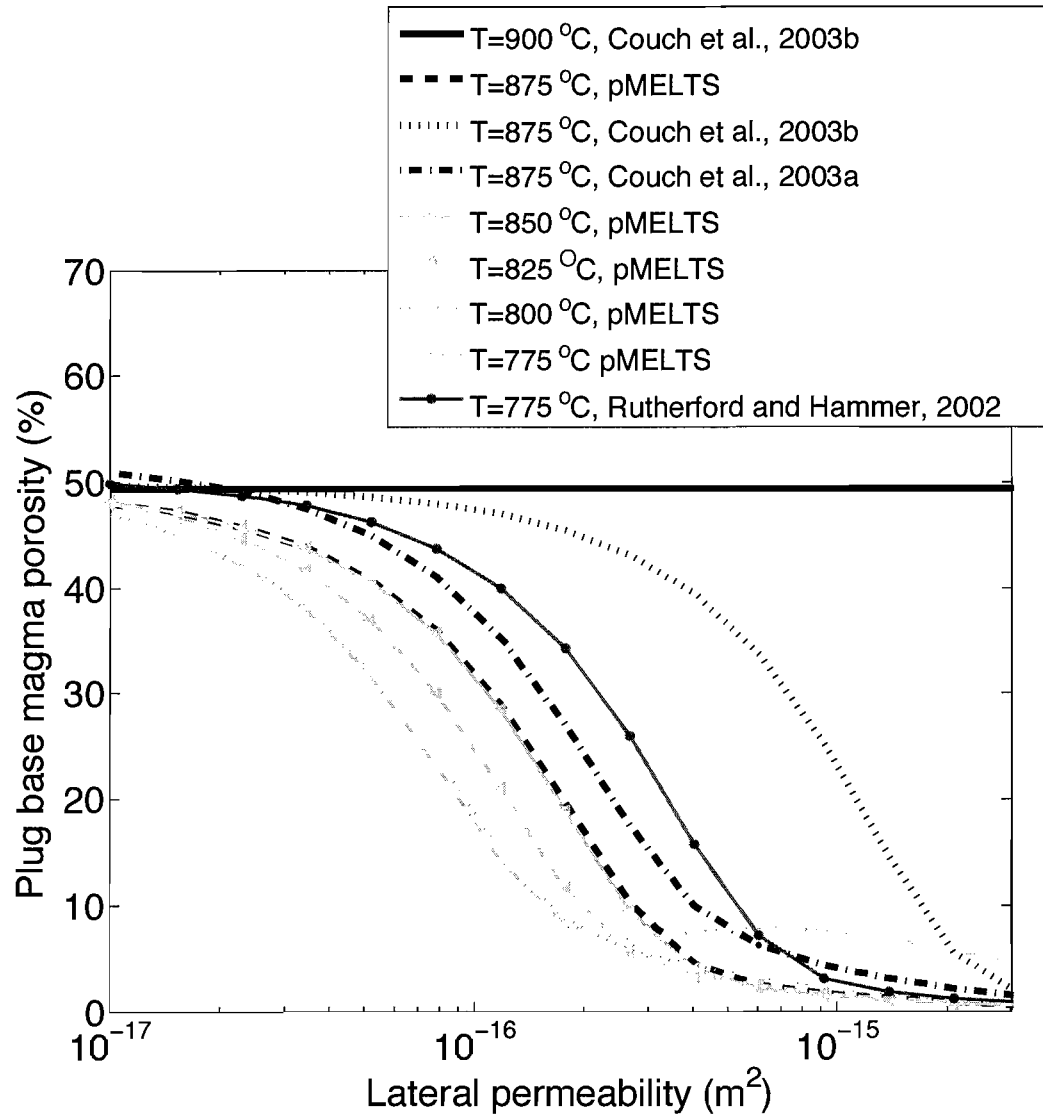
Figure 5.17 Excluding the results from Couch et al. (2003b) at 900 °C, the effect of the

pressure-crystallization relationship is small compared to the effect of degassing.

800 °C, 825 °C, 850 °C and 875 °C with a composition published by Pallister et al. (2009) that represents the average of samples collected from spines 3-7 (~65% SiO_2). Slow decompression experimental results from Couch et al. (2003a) (71-78% SiO_2, 1-7% H_2O, 875 °C), Couch et al. (2003b) (71-79% SiO_2, 3-8% H_2O, 900 and 875 °C) and Hammer and Rutherford (2002) (71-76% SiO_2, 1-8% H_2O, 775 °C) were also used for comparison.

Modeling results from pMELTS predicts that higher temperatures delay crystallization until lower pressures, and the relative abundance of melt has implications for degassing behavior. For example, using the pressure-crystallinity relationship from Couch et al. (2003b), which were conducted at 900 °C, lateral permeability has no effect on the plug base porosity. This occurs because the critical bubble connectivity threshold is the ratio of the volume of bubbles to the volume of bubbles and melt, and the increased amount of melt at high temperatures prevents the system from reaching the threshold of 60%. For all temperatures below 900 °C, however, the plug base porosity decreases as lateral permeability increases. Model runs at higher temperatures tend to elevate plug base porosities, though the effect of variations in lateral permeability is at least as important. Modeling with pMELTS was conducted with identical compositions. The range in behavior from 775 °C and 875 °C is small and degassing is more influential. This underscores the importance of the role of degassing compared to temperature changes when composition is constant.

Figure 5.18 illustrates the effect of temperature on the plug base pressure. For the 900 °C results from Couch et al. (2003b), lateral permeability has no influence on the
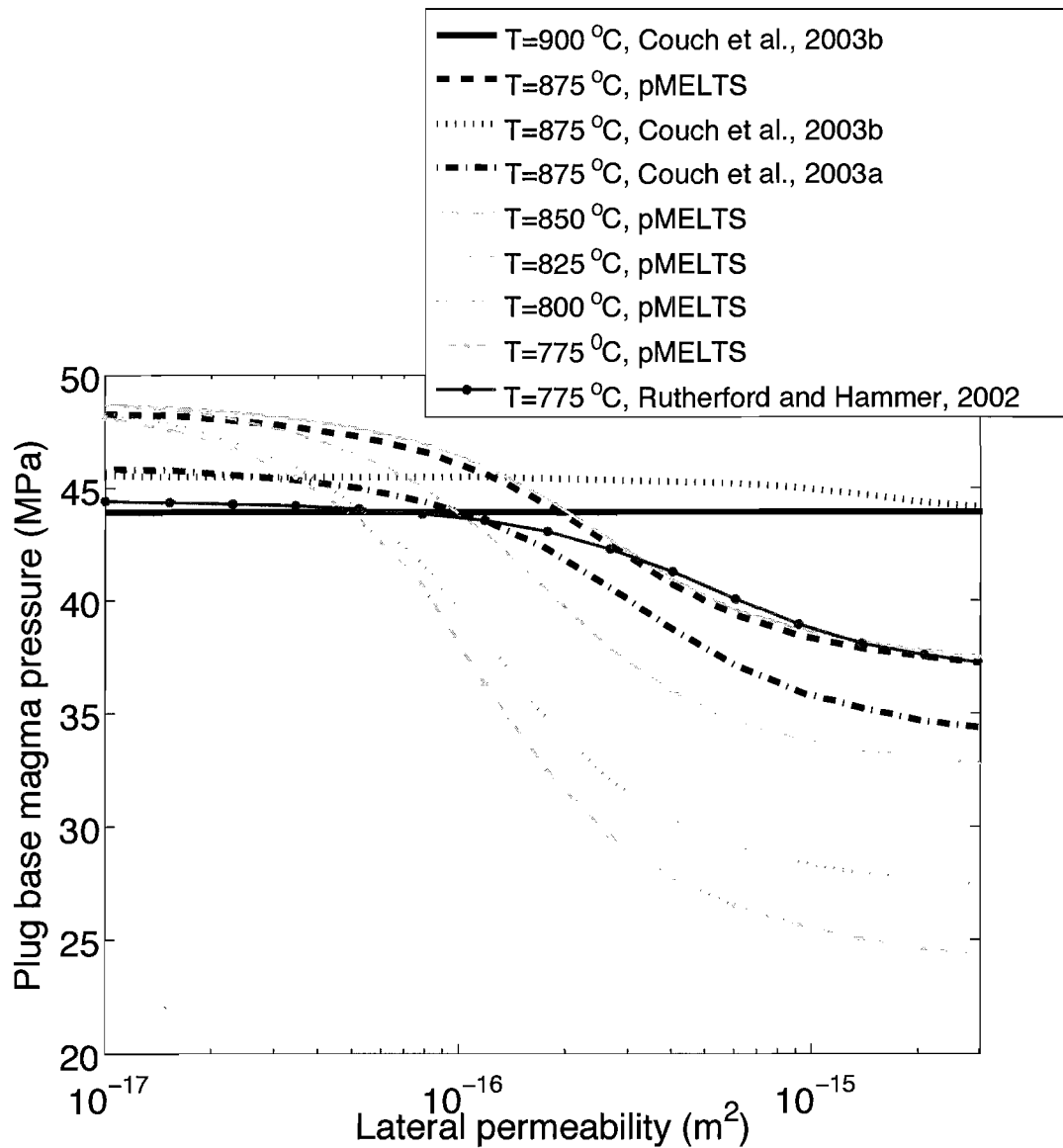
Figure 5.18 When degassing is weak at low lateral permeabilities the pressure-crystallization relationship has little effect in the magma pressure at the top of the conduit. At higher permeabilities, however, the relationships from lower temperatures tend to have a pronounced effect on pressure over the high temperature relationships. At lower temperatures the crystal content is higher for a given pressure and this increases the pressure gradient magnitude.

plug base pressure because of the lack of degassing. The pressure-crystallinity relationships from lower temperatures result in diminished plug base pressures with increased permeabiltity because of advanced crystallization. While the effect on plug base porosity is about the same for all temperatures at high lateral permeabilties, the effect on pressure is more pronounced for lower temperatures.

<u>The effect of vertical gas flux</u>

Prior sensitivity studies have not addressed vertical flow of gas in the magma. Vertical flux requires that the bubble connectivity threshold be met, just as this requirement exists for lateral flow to occur. Gas pathways are similarly expected to remain open once established, even if porosity levels subsequently fall below the connectivity threshold. The local magma pressure gradient drives gas flow, and this driving pressure gradient is more reliably constrained than the lateral gradient driving lateral flow. The model has no vertical boundary condition for vertical gas flow and so to be physically consistent it must act in concert with lateral degassing in order to prevent the buildup of free gas at the plug base that would otherwise occur. This section addresses a series of model runs with a range of vertical permeabilities. The values listed are expected to represent the maximum vertical permeability over a given cross section of conduit because the vertical pathways act in parallel. This contrasts with lateral degassing, which occurs in series so that the value listed represents the minimum, limiting permeability. Local vertical permeability is expected to depend on bubble aspect ratios, with vertically elongated bubbles tending to favor vertical gas flow. The bubble

aspect ratio is dependent on shear rate and is highest near the conduit wall for a parabolic velocity profile.

Figure 5.19 illustrates the influence of vertical gas flux at intermediate lateral permeability values of 10^{-16} m^2. When the lateral permeability is low the effect of vertical gas flux is also small. At high lateral permeabilities the vertical flux of gas has no discernible effect on degassing since it already does so efficiently. Vertical permeabilties must be greater than about 10^{-15} m^2 to produce an effect. Although this value would be considered large for lateral gas flux, the vertical pressure gradient driving vertical gas flow is of order 10^4 Pa/m, whereas the lateral pressure gradient is of order 10^5 Pa/m and therefore a relatively higher vertical permeability is necessary to generate comparable gas velocities. The plot shows that vertical gas flux can have a large effect on the porosity profile once degassing initiates. The final porosity when the vertical permeability is 10^{-15} m^2 is 30% (slightly less than when vertical permeability is zero). By increasing the vertical permeability slightly more than an order of magnitude, to 2×10^{-14} m^2, the resulting plug base porosity is zero (because vertical gas flux is not dependent on local porosity vertical gas flux can completely degas a section of conduit).

<u>Consistency with plug base pressure and porosity constraints</u>

The prior two sections have addressed the system response to independent changes in magma or conduit parameters. For some parameters, like conduit height, the nominal values tends to be the most efficient at yielding dense magma at the top of the conduit. Changes in the initial water concentration do not yield results consistent with
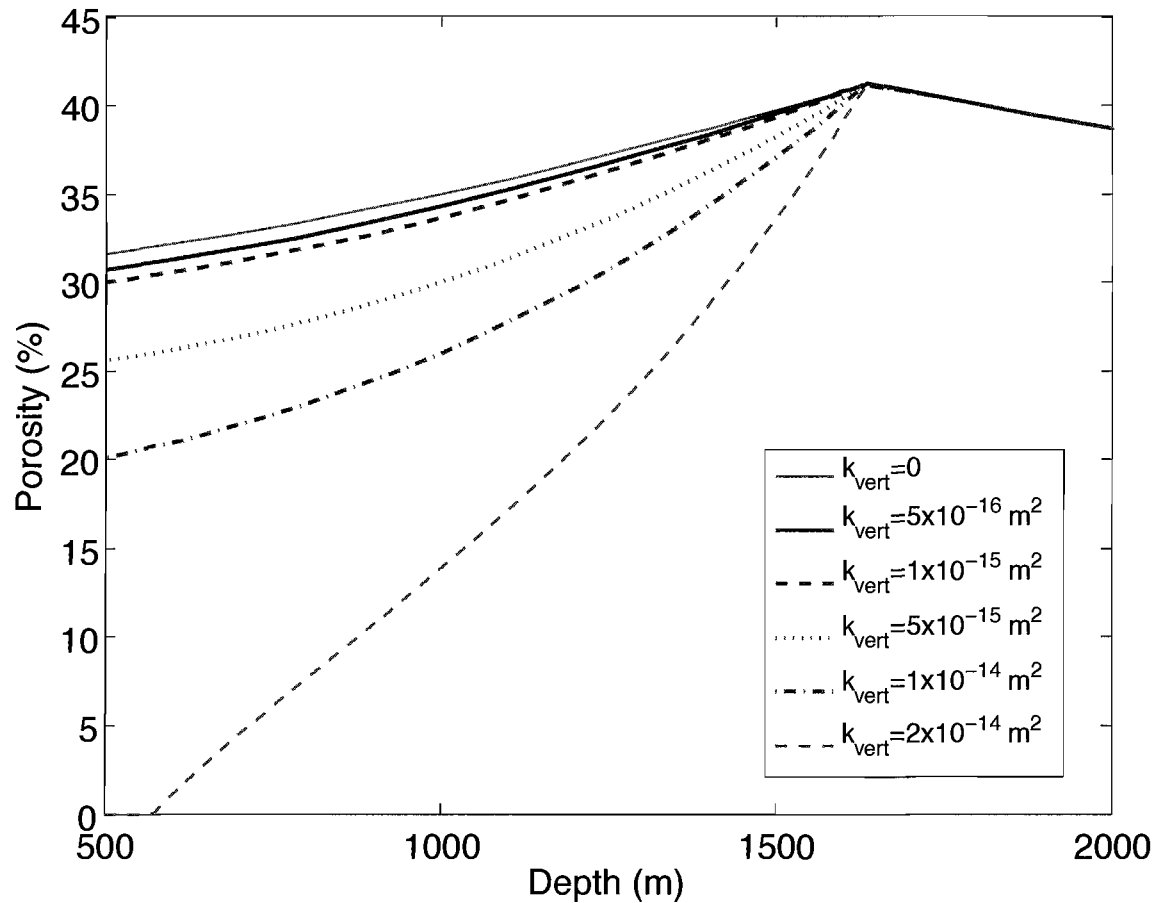
Figure 5.19 The porosity profile for a series of values of vertical permeability. The

lateral permeability is set to 10^{-16} m^2 in all cases. The vertical permeability not influential

when it is below about 10^{-15} m^2, but between that value and 2×10^{-14} m^2 it can have a

strong effect on the magma porosity.

the pressure constraint. For other parameters, like initial pressure and bubble connectivity threshold, the nominal values do not yield results consistent with the known constraints. For example, a decrease in the initial magma pressure from 130 MPa to 115 MPa will result in upper conduit magma with a few percent porosity at about 18 MPa when the lateral permeability is 10^{-14} m^2. Similarly, decreasing the bubble connectivity threshold to 30% will yield similar results at the same lateral permeability. In the high permeability limit the lowest pressure possible at the plug base is about 30 MPa, representing an overpressure of almost 20 MPa that would likely produce eruptive behavior much different than slow and steady spine extrusion. This is an interesting result because although the process of degassing exerts considerable control over conduit and eruptive dynamics, it indicates the system is largely insensitive to changes in the amount of water in the initial magma. Temperature can have a moderate affect on the plug base pressure and porosity but is unable to match the constraints at the top of the conduit. The thermodynamic modeling results from running pMELTS at 775 °C yields a plug base pressure of 24 MPa in the high lateral permeability limit. While the trend suggests a lower temperature would generate favorable results, 775 °C is likely near the solidus and so assuming a lower temperature is probably physically unrealistic. For the nominal conduit radius of 100 m the viscous effects are very small relative to density effects and so deviation from the nominal value must be large in order to yield a substantial effect. It was established in the prior section that conduit radii of about 10-15 m are capable of generating pressure gradients several times that of larger conduits.

There likely exist many combinations of small changes to the system parameters capable of yielding results consistent with the shallow constraints. Figures 5.20, 5.21 and 5.22 illustrate examples chosen to frame a discussion. Figure 5.20 illustrates the resulting conduit pressure and porosity profile when the critical connectivity threshold is reduced to 30%, the lateral permeability is set at 10^{-14} m^2, and there is no vertical degassing. Degassing begins at a depth of about 3200 m and the conduit is essentially devoid of free gas at any shallower depth. Degassing is abrupt and the conduit is emptied of its ~20% gas over a very small depth range. The pressure gradient is nearly constant over the conduit height at roughly magmastatic values because the conduit is large and viscous resistance is small. The deep degassing depth is necessary to sufficiently densify overlying magma and increase the pressure gradient magnitude. Figure 5.21 shows the effect of decreasing the initial magma pressure to 115 MPa, also with a lateral permeability set to 10^{-14} m^2. Degassing begins at a depth of about 2200 m and is also abrupt as in the previous case. The conduit is effectively empty of gas for the 1700 m beneath the plug. The pressure gradient is also approximately constant in this case, although there is a small change in slope when the conduit degasses. These two cases attain the upper conduit constraints with either a small change in a well-constrained parameter (chamber pressure) or a large change in a relatively free parameter (connectivity threshold). Both cases, however, take advantage of the requirement that connected bubbles stay connected at porosities below the threshold. It is physically
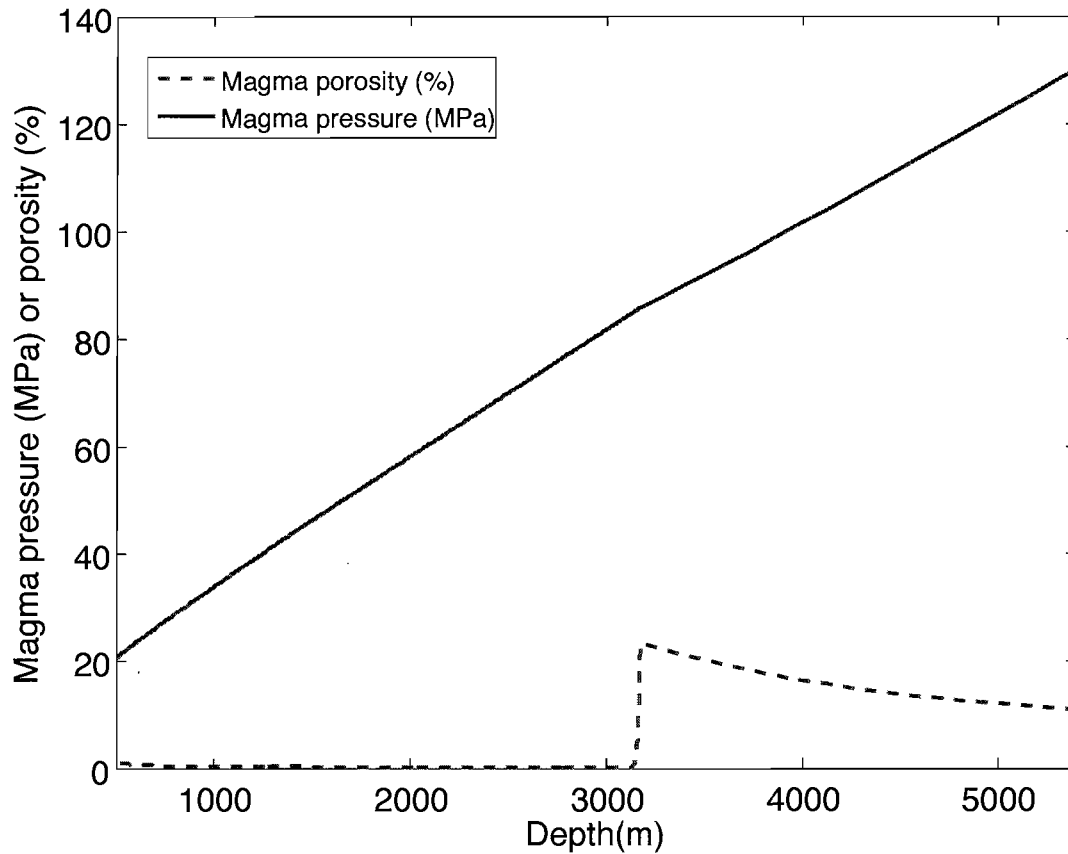
Figure 5.20 A simulation yielding upper conduit magma pressure and porosity values

matching the constraints imposed by the presence of a dense, 500-m thick plug. The

bubble connectivity threshold is set to 30% and degassing begins at about 3200 m depth.

The lateral permeability is set to 10^{-14} m^2, and all other parameters are set to nominal
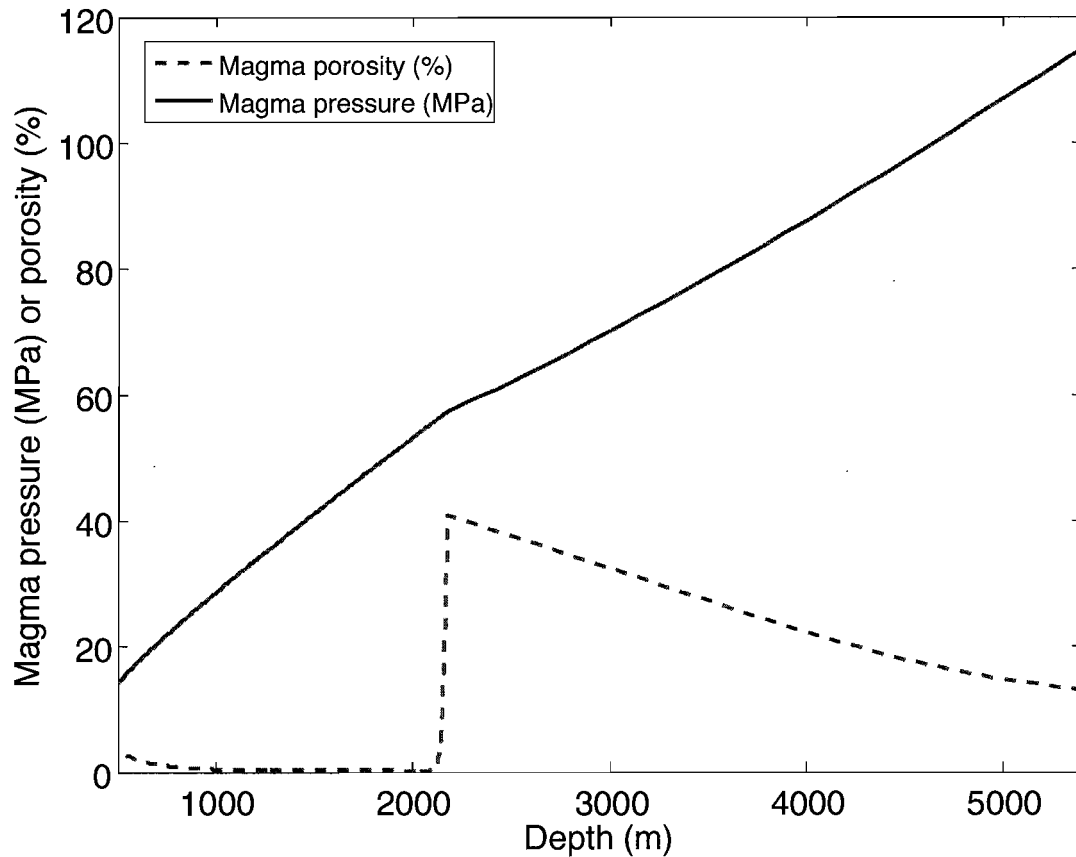
values.

Figure 5.21 A second simulation yielding results consistent with the upper conduit

constraints. The initial magma pressure was set to 115 MPa, the lateral permeability to

10^{-14} m^2. All other parameters are set to their nominal value. The lower initial magma

pressure results in a lower amount of gas dissolved in the melt, which results in a high

initial gas volume fraction. The connectivity threshold is reached at a depth of 2200 m.
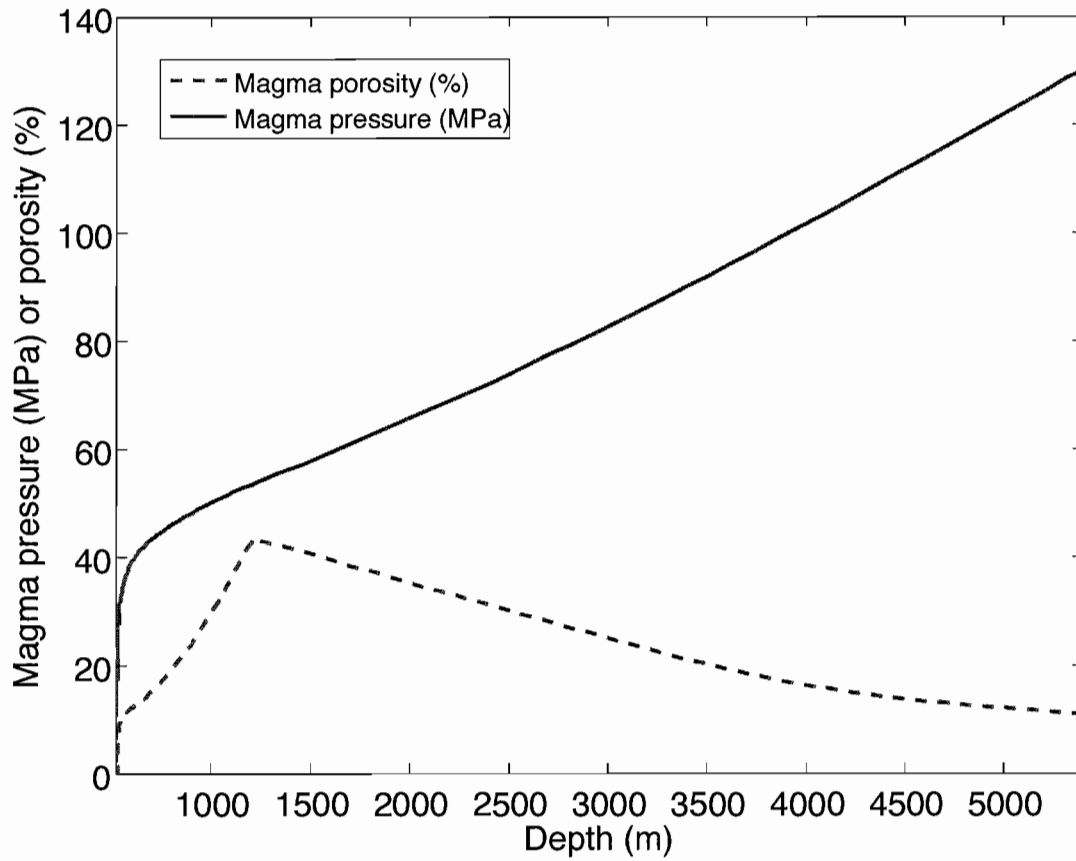
Figure 5.22 This simulation uses intermediate values for both lateral permeablity

$(5 \times 10^{-16} \text{ m}^2)$ and vertical permeability $(4 \times 10^{-15} \text{ m}^2)$ and degassing is accordingly gradual.

The conduit radius is set at 22.5 m, resulting in the large magnitude pressure gradient at

shallow depths. All other parameters are set to nominal values.

questionable to assume that the conduit is capable of suddenly degassing and that any additional bubbles exsolved are immediately removed from the conduit.

Based on the sensitivity studies the only remaining parameter change that can provide favorable results is a constriction in conduit radius. Figure 5.22 shows the results of setting the conduit radius to 22.5 m, the lateral permeability to 5×10^{-16} m^2, the vertical permeability to 4×10^{-15} m^2 but all other parameters to their nominal values. The constriction of radius requires that the magma flow rate increase to maintain volumetric output at 2 m^3/s. The increase is by nearly a factor of 20 over the flow rate when the conduit is of radius 100 m. This has implications for the assumption of equilibrium crystallization. The published decompression experiments were conducted at a range of decompression rates but the slowest were still conducted at rates at least one order of magnitude faster than typical conditions in the conduit at Mount St. Helens. Therefore, while the vertical magma flow rate for a conduit 22.5 m in radius is about 1 mm/s, when scaled by the pressure gradient this is still slow for considerations about crystallization kinetics. For the constricted-radius case degassing begins at a depth of about 1200 m and takes place gradually until the base of the plug. The steady degassing increases the crystal volume fraction, and the increase in viscosity generates a large magnitude pressure gradient. The viscous effects, rather than the effects from a dense, gas-free magma, yield a plug base pressure near the upper conduit constraint. This represents a process that might be more physically realistic. It does not require sudden degassing but

instead gas slowly flows out of the magma and porosity steadily declines until low values

are reached at the plug base.

<div align="center">Implications for SPASM and generating seismicity</div>

SPASM requires a lumped magma and wall rock compressibility of 10^{-7} Pa^{-1} to

accommodate sufficient elastic strain to generate slip events separated by about 100 s.

Unless it is completely gas-free, the magma is expected to be much more compressible

than the wall rock. Therefore, the magma compressibility will largely control the system.

Lower compressibility values (more incompressible materials) result in more frequent

slip events (earthquakes). The interval between slip events is proportional to the square

root of the lumped compressibility $\Delta t \sim (\beta_1 + \beta_2)^{1/2}$. Iverson (2009) indicates that

modeling the magma properties using Conflow (Mastin and Ghiorso, 2000) yields a

magma compressibility of 10^{-7} Pa^{-1} when the depth averaged porosity below the plug is

about 12%. Conflow calculates the bulk magma compressibility as the sum of the

compressibility of each component scaled by the corresponding volume fraction so that β

$_{magma} = \alpha\beta_{gas} + \chi\beta_{solid} + \phi\beta_{liq}$, where ϕ is the volume fraction of liquid. The

compressibility of the solid component is taken as 10^{-11} Pa^{-1}, and the compressibility of

the liquid phase depends on the composition of the melt but is expected to be comparable

to that of the solid. The gas compressibility is calculated in Conflow using ideal gas

relations: $\beta_{gas} = (A/\rho)(\partial\rho_{gas}/\partial p)$. The term A is equal to one in the isoentropic case and

in the isothermal case is equal to the ratio between specific heats under constant pressure

and those under constant volume. For water vapor in the isothermal case the ratio A is

approximately 4/3. Therefore, the gas component compressibility β_{gas} is constrained to lie between p^{-1} and $(4/3)p^{-1}$. Scaling the gas compressibility by the gas volume fraction yields an expression for the bulk magma compressibility because of the relative incompressibility of the melt and crystal phases. The depth range of the conduit over which the compressibility influences plug dynamics is a characteristic length scale - the conduit radius in the nominal case (100 m). The average magma pressure over this range is about 14 MPa. Therefore, if the average porosity over this range were 12%, the magma compressibility is approximately 1.1×10^{-8} Pa^{-1} in the isothermal case. This represents nearly an order of magnitude lower than the value reported in Iverson (2009) and would result in stick times of about 30 s.

Neither of the end member cases for my conduit modeling discussed in the last section is likely to generate favorable magma compressibility values. In either case the conduit is essentially devoid of bubbles in the 100 m beneath the plug. If the depth range over which the compressibility has influence on plug mechanics is taken to be larger, however, the small radius case of rapid and shallow degassing generates more compressible magma over that range than does the case where degassing is deep. If the active depth range is assumed to extend to the depth where gas volume fraction is largest, i.e. just when it reaches the connectivity threshold, an average gas volume fraction of 20% results. With an approximate average magma pressure of 20 MPa the resulting magma compressibility is 1.3×10^{-8} Pa^{-1}, still almost an order of magnitude smaller than

that necessary for SPASM. In fact, attaining a magma compressibility of 10^{-7} Pa^{-1} at 13 MPa in the isothermal case requires a porosity of ~98%.

The above calculations assume that pressure changes are fast relative to time scales for gas exsolution. While plug slip events are short-lived, if exsolution is taken to be in equilibrium with changes in pressure the result is a more compressible magma. In the case of slow pressure changes the magma compressibility is also governed by the bulk magma density, the gas density, and the dissolved water concentration. The governing equation becomes $\beta_{magma} = (\alpha/p) [1+(\rho_{magma} c_g/\rho_{gas})]$. The resulting magma compressibility increases by about 60% under slow pressure changes case, yielding a value of 2.1×10^{-8} Pa^{-1} and stick times of 45 s. The stick time is also proportional to the 1/2 power of conduit height h, the plug thickness $H-h$ and the dome rock density ρ_{dome}. In order to regain original stick times these three terms need to collectively increase by a factor of five. These constraints are sufficiently constrained such that this does not seem possible.

The modeling results suggest that the magma beneath the extruding plug at Mount St. Helens was too incompressible to yield stick times longer than about 45 s. Elastic strain must be accommodated by another process. The spine is subaerial, and therefore the walls of the plug and its mantle of gouge represent the only remaining plug surface. The elastic properties of the gouge, therefore, are highly influential to plug extrusion. A more complete model would involve slip in discrete patches, as is commonly observed on tectonic faults and has been described using the concepts of rate and state friction (e.g.,

Rice and Ruina, 1983). If the idealized treatment of SPASM is assumed and if fault gouge can accommodate strain with an equivalent modulus equivalent to $\sim 8 \times 10^{-8}$ Pa^{-1}, then the slip periods predicted by SPASM can be achieved by wholesale seismogenic plug slip. This value is likely too high for the fault gouge, however, in which case slip can only occur on smaller, discrete patches.

CHAPTER VI

CONCLUSIONS

This project introduced a steady-state conduit model to investigate magma property

dynamics and the implications for extrusive behavior. This work draws on prior models

in assuming Poiseuille flow of magma and a lumped-parameter Darcy flux of gas radially

out of the conduit. This model improves on prior models with regard to how certain

parameters are calculated, in part by drawing on recently published research. The bulk

viscosity parameterization of Costa (2005), for example, defines a maximum viscosity

and captures the transition from viscous flow to brittle bulk extrusion. Other ingredients

of this model are novel, such as the use of thermodynamic modeling to represent the

evolution of decompression crystallization and the assumption that water pressure should

diminish to hydrostatic pressure rather than lithostatic pressure.

The model predictions are highly dependent on degassing behavior. As a

consequence, the system is highly sensitive to the permeability, especially in the lateral

direction. When lateral permeability is at intermediate values between about 10^{-17} m^2 and

10^{-15} m^2, the geometry of the conduit and the initial conditions at the magma chamber

become important. The influence exerted by changes in parameter values can be

attributed to alterations in degassing behavior. This is true for changes in conduit height,

the bubble connectivity threshold, the initial water concentration, the initial magma

pressure and, to a certain extent, the pressure-crystallization relationship. Changes in

conduit radius also influence degassing, but the changes more strongly control the

magnitude of the pressure gradient. The nominal value for the conduit radius is large and the known volumetric output rate is low, so that the pressure gradient is close to magmastatic under nominal conditions. At values of the conduit radius below about 30 m, however, viscous effects are increasingly influential on magma pressure for smaller radii.

The model was able to predict near lithostatic pressure and dense, low porosity magma with ~60% crystals at the top of the conduit, consistent with conditions necessary for the transition to a solid plug and low extrusion rates. The effects of degassing alone predicted these constraints with either a ~12% decrease in initial magma pressure or 50% decease in bubble connectivity threshold relative to nominal initial values of 130 MPa and 60%, respectively. In either case a lateral permeability of 10^{-14} m^2 is necessary to drive off gas rapidly and to continually drive away gas as it exsolves from the melt. On the other hand, a decrease in conduit radius to 22.5 m also yields predictions consistent with plug base constraints. In this case intermediate values of both lateral and vertical permeability result in gradual degassing and viscous resistance becomes large in the upper conduit and increases the local magma pressure gradient magnitude. In either case degassing plays an important role and the model is able to capture this behavior with a relatively simple degassing governing law. A more physically accurate model might treat magma permeability as a function of the velocity gradient dV/dz, such that in portions of the conduit where magma velocity is increasing, it augments the vertical permeability, and where it is decreasing, it increases the lateral permeability. The results of this model,

however, do not necessarily require such a treatment. In the context of SPASM, my model calculated the compressibility of magma below the plug at about 20% of the value required to generate stick durations comparable with drumbeat earthquake periods. The other variables on which the stick time depends in SPASM are unlikely to increase magma compressibility substantially. Although the fault gouge accommodates some amount of elastic strain according to its moduli, an equivalent value of 8×10^{-8} Pa^{-1} is implausibly large. Therefore, if plug extrusion is the source of the drumbeat earthquakes, fault slip must occur on discrete patches rather than along the entire plug bounding fault. This interpretation is supported by the general understanding that seismic slip patches are smaller than total surface area of the plug bounding fault ($\sim$300,000 m^2).

The rich data set arising from the extensive monitoring and research of Mount St. Helens in recent years assisted in assigning parameter values. The model, however, is not specific to this volcano or even to solid spine extrusions. Eruptions of lava lobes or endogenous domes are characterized by higher volumetric output rates. Their viscous behavior requires that magma at the vent be below the viscous-brittle crystal volume fraction. The only parameterization of the model that would require adjustment to model this behavior is the pressure-crystallization relationship. The increased magma ascent rates imply that crystallization occurs in disequilibrium. Results from laboratory experiments at comparable decompression rates are more likely to reflect the relationship between crystallization and pressure than thermodynamic modeling. Otherwise, employing surface constraints of appropriate magma pressure and low bulk viscosity in

the model should be useful in constraining the conduit dynamics of that system.

This project also introduced a novel method for characterizing roughness of fault surfaces. I've shown that combining standard digital images with MeX software is capable of producing DEMs from hand samples with a resolution of 10s of microns. The power spectra for profiles both parallel and normal to fault slip follow a power law. This result seems to contradict the conclusions of prior work, which has found a power law relationship only on small-slip faults (<1 m). The striated outer surface of the Mount St. Helens gouge is laterally continuous and the amount of total slip is well constrained from petrologic and physical considerations. One possible explanation for the discrepancy is that Sagy et al. (2007) and Sagy and Brodsky (2009) investigated tectonic normal faults where conditions are considerably different from those in the volcanic environment studied here. Sagy et al. (2007) and Sagy and Brodsky (2009) investigated faults they inferred to have been exhumed from shallow (<5 km) depths, where temperatures are expected to be much lower than those in the volcanic setting of the conduit fault. Moreover, because of the rheological transition it is not clear how much of the ~500 m of extrusion to the surface was characterized by purely brittle failure. Microscopic analysis of gouge samples seems to capture evidence of a combination of plastic and brittle deformation. This project also determined the permeability of gouge samples to be relatively high, implying that gas flux through the gouge is an important process with the potential to diminish the normal stress and maintain elevated temperatures by advecting heat from depth.

Those factors aside, however, the power law behavior of the surface roughness is well documented over a range of orders of magnitude, owing to the high resolution of the DEMs. This suggests that purely brittle slip may have initiated shallower than the depth to crystallization of 500 m and that some deformation took place near the brittle-ductile transition where viscous deformation is also important. This seems to be evidenced in thin section (Figures 3.8 and 3.9) and in meter-scale cross sections of spine 4 (Figure 3.2). If viscous deformation were important over some depth range this limits the depth range over which purely brittle failure of completely crystallized gouge can generate seismicity. Viscous deformation along the bounding fault is also consistent with thermal considerations. The time scale for spine extrusion is short compared to the time scale for heat to diffuse away from the spine. This, combined with surface temperature measurements of spine material >700 °C (Schneider et al., 2009), suggests that the bounding fault was at elevated temperatures, increasing the likelihood of behavior near the brittle-ductile transition. Recent laboratory experiments have found that shear of highly viscous silicate magmas is capable of producing seismic signals at sufficiently high strain rates (Tuffen et al., 2008; Lavallee et al., 2008). This implies that magma fracture may be a source of drumbeat seismicity. Moreover, the features depicted in Figures 3.2, 3.8 and 3.9 are extensional in nature. Shear fracturing of highly viscous magma that generates extensional features is to first order compatible with the seemingly contradictory seismic evidence: dilatational first motions and moment magnitude-frequency scaling consistent with brittle faulting.

REFERENCES

Barmin, A., Melnik, O, and Sparks, R.S.J. (2002). Periodic behavior in lava dome eruptions. *Earth and Planetary Science Letters, 199,* 173-184.

Bergfeld, D., Evans, W.C., McGee, K.A., and K.R. Spicer. (2009). Pre- and post-eruptive investigations of gas and water samples from Mount St. Helens, Washington, 2002-2005. In Sherrod, D.R., Scott, W.E. and Stauffer, P.H. (eds.), *A volcano rekindled: the renewed eruption of Mount St. Helens, 2004-2006* (pp. 523-542). U.S. Geological Survey Professional Paper 2009-1750.

Blanpied, M.L., Lockner, D.A., and Byerlee, J.D. (1991). Fault stability inferred from granite sliding experiments at hydrothermal conditions. *Geophysical Research Letters, 18,* 609-612.

Burnham, C.W. (1975). Water and magma – mixing model. *Geochimica et Chosmochimica Acta, 39,* 1077-1084.

Cashman, K.V., Thornber, C.R., and Pallister, J.S. (2009). From dome to dust; shallow crystallization and fragmentation of conduit magma during the 2004-2006 dome extrusion of Mount St. Helens, Washington. In Sherrod, D.R., Scott, W.E. and Stauffer, P.H. (eds.), *A volcano rekindled: the renewed eruption of Mount St. Helens, 2004-2006* (pp. 387-414). U.S. Geological Survey Professional Paper 2009-1750.

Clynne, M.A., Calvert, A.T., Wolf, E.W., Evarts, R.C., Fleck, R.J., and Lanphere, M.A. (2009). The Pleistocene Eruptive history of Mount St. Helens, Washington, from 300,000 to 12,800 years before present. In Sherrod, D.R., Scott, W.E. and Stauffer, P.H. (eds.), *A volcano rekindled: the renewed eruption of Mount St. Helens, 2004-2006* (pp. 593-628). U.S. Geological Survey Professional Paper 2009-1750.

Costa, A. (2005). Viscosity of high crystal content melts: dependence on solid fraction. *Geophysical Research Letters, 32,* 22,308-22,313.

Couch, S., Sparks, R.S.J., and Carroll, M.R. (2003a). The kinetics of degassing-induced crystallization at Soufrière Hills Volcano, Monserrat. *Journal of Petrology, 44,* 1477-1502.

Couch, S., Harford, C.L., Sparks, R.S.J., and Carroll, M.R. (2003b). Experimental constraints on the conditions of formation of highly calcic plagioclase microlites at the Soufrière Hills Volcano, Montserrat. *Journal of Petrology,* (44), 1455-1475.

Diller, K., Clarke, A.B., Voight, B., and Neri, A. (2006). Mechanics for conduit plug formation: Implications for vulcanian eruptions. *Geophysical Research Letters, 33,* 20,302-20,308   .

Eichelberger, J.C. (1995). Silicic volcanism: Ascent of viscous magmas from crustal reservoirs," *Annual Review of Earth and Planetary Science, 23,* 41-63.

Ghiorso, M.S., Hirschmann, M.M., Reiners, P.W., and Kress, V.C. (2002). The pMELTS: A revision of MELTS aimed at improving calculation of phase relations and major element partitioning involved in partial melting of the mantle at pressures up to 3 GPa. *Geochemistry Geophysics Geosystems, 3,* 1030.

Hammer, J.E. and Rutherford, M.J. (2002). An experimental study of the kinetics of decompression-induced crystallization in silicic melt. *Journal of Geophysical Research, 107,* 2021-2045.

Harrington, R.M. and E.E. Brodsky, 2007, "Volcanic hybrid earthquakes that are brittle-failure events," Geophysical Research Letters, vol. 34, L06308.

He, C.R., Wang, Z.L., and Yao, W.M. (2007). Frictional sliding of gabbro gouge under hydrothermal conditions. *Tectonophysics, 445,* 353-362.

Hui, H. and Zhang, Y. (2007). Toward a general viscosity equation for natural hydrous and anhydrous silicate melts. *Geochimica et Cosmochimica Acta, 71,* 403-416.

Iverson, R.M. (2009). Dynamics of seismogenic volcanic extrusion resisted by a solid surface plug, Mount St. Helens, 2004-2005. In Sherrod, D.R., Scott, W.E. and Stauffer, P.H. (eds.), *A volcano rekindled: the renewed eruption of Mount St. Helens, 2004-2006* (pp. 425-460). U.S. Geological Survey Professional Paper 2009-1750.

Iverson, R.M., Dzurisin, D., Gardner, C.A., Gerlach, T.M., LaHusen, R.G., Lisowski, M., Major, J.J., Malone, S.D., Messerich, J.A., Moran, S.C., Pallister, J.S., Qamar, A.I., Schlling, S.P., and Vallance, J.W. (2006). Dynamics of seismogenic volcanic extrusion at Mount St. Helens in 2004-05. *Nature, 444,* 439-443.

Jaupart, C. and Allegre, C.J. (1991). Gas content, eruption rate and instabilities of eruption regime in silicic volcanoes. *Earth and Planetary Science Letters, 102,* 413-429.

Lavallee, Y., Meredith, P.G., Dingwell, D.B., Hess, K.U., Wassermann, J., Cordonnier, B. Gerik, A., and Kruhl, J.H. (2008). Seismogenic lavas and explosive eruption forecasting. *Nature, 453*, 507-510.

Lejeune A. and Richet, P. (1995). Rheology of crystal-bearing silcate melts: An experimental study at high viscosities. *Journal of Geophysical Research, 100*, 4215-4229.

Lensky, N.G., Sparks, R.S.J., Navon, O., and Lyakhovsky, V. (2008). Cyclic activity at Soufrière Hills Volcano, Montserrat: degassing-induced pressurization and stick-slip extrusion. In Lane, S.J. and Gilbert, J.S. (eds.) *Fluid Mechanics in Volcanic Conduits: A source of Seismic and Acoustic signals* (pp. 169-188). Geological Society of London Special Publications, *307*.

Mastin, L.G. and Ghiorso, M.S. (2000). A numerical program for steady-state flow of magma-gas mixtures through vertical eruptive conduits. *U.S. Geological Survey Open-File Report 00-209*.

Matoza, R.S., Graces, M.A., Chouet, B.A., D'Auria, L., Hedlin, M.A.H., Groot-Hedlin, C.D., and Waite, G.P. (2009). The source of infrasound associated with long-period events at Mount St. Helens. *Journal of Geophysical Research, 114*, 4305-4343.

Melnik, O. and Sparks, R.S.J. (1999). Nonlinear dynamics of lava dome extrusion. *Nature, 402*, 37-41.

Melnik, O. and Sparks, R.S.J. (2005). Controls on conduit magma flow dynamics during lava dome building eruptions. *Journal of Geophysical Research, 110*, 2209.

Michaut, C., Bercovici, D., Sparks, R.S.J. (2009). Ascent and compaction of gas rich magma and the effects of hysteretic permeability. *Earth and Planetary Science Letters, 282*, 258-267.

Moore, P.L., Iverson, N.R., and Iverson, R.M. (2009). Frictional properties of the Mount St. Helens gouge. In Sherrod, D.R., Scott, W.E. and Stauffer, P.H. (eds.), *A volcano rekindled: the renewed eruption of Mount St. Helens, 2004-2006* (pp. 415-424). U.S. Geological Survey Professional Paper 2009-1750.

Moran, S.C., Malone, S.D., Qamar, A.I., Thelen, W., Wright, A.K., and Caplan-Auerbach, J. (2009). Seismicity associated with renewed dome-building at Mount St. Helens, 2004-2005. In Sherrod, D.R., Scott, W.E. and Stauffer, P.H. (eds.), *A volcano rekindled: the renewed eruption of Mount St. Helens, 2004-2006* (pp. 27-60). U.S. Geological Survey Professional Paper 2009-1750.

Neuberg, J.W. (2006). The trigger mechanism of low-frequency earthquakes on Montserrat. *Journal of Volcanology and Geothermal Research, 153,* 37-50.

Neuberg, J.W., Luckett, R., Baptie, B., and Olsen, K. (2006). Models of tremor and low-frequency earthquake swarms on Monserrat. *Journal of Volcanology and Geothermal Research, 101,* 83-104.

Pallister, J.S., Thornber, C.R., Cashman, K.V., Clynne, M.A., Lowers, H.A., Mandeville, C.W., Brownfield, I.K., and Meeker, G.P. (2009). Petrology of the 2004-2006 Mount St. Helens lava dome - implications for magmatic plumbing and eruption triggering. In Sherrod, D.R., Scott, W.E. and Stauffer, P.H. (eds.), *A volcano rekindled: the renewed eruption of Mount St. Helens, 2004-2006* (pp. 647-702). U.S. Geological Survey Professional Paper 2009-1750.

Poland, M.P., Dzurisin, D., LaHusen, R.G., Major, J.J., Lapcewich, D., Endo, E.T., Gooding, D.J., Schilling, S.P., and Janda, C.G. (2009). Remote camera observations of lava dome growth at Mount St. Helens, Washington, October 2004 to February 2006. In Sherrod, D.R., Scott, W.E. and Stauffer, P.H. (eds.), *A volcano rekindled: the renewed eruption of Mount St. Helens, 2004-2006* (pp. 225-236). U.S. Geological Survey Professional Paper 2009-1750.

Rice, J.R. and Ruina, A.L. (1983). Stability of Steady Frictional Slipping. *Journal of Applied Mechanics, 50,* 343-349.

Roscoe, R. (1952). The viscosity of suspensions of rigid spheres. *British Journal of Applied Physics, 3,* 267-269.

Rust, A.C. and Cashman, K.V. (2004). Permeability of vesicular silicic magma: inertial and hysterises effects. *Earth and Planetary Science Letters, 228,* 93-107.

Rutherford, M.J. and Devine, J.D., III, (2009). Magmatic conditions and processes in the storage zone of the 2004-2006 Mount St. Helens dacite. In Sherrod, D.R., Scott, W.E. and Stauffer, P.H. (eds.), *A volcano rekindled: the renewed eruption of Mount St. Helens, 2004-2006* (pp. 703-726). U.S. Geological Survey Professional Paper 2009-1750.

Sagy, A., and Brodsky, E.E. (2009). Geometric and rheological asperieties in an exposed fault zone. *Journal of Geophysical Research, 114*, 2301-2316.

Sagy, A., Brodsky, E.E., and Axen, G.J. (2007). Evolution of fault-surface soughness with slip. *Geology, 35*, 283-286.

Schilling, S.P., Thompson, R.A., Messerich, J.A. and Iwatsubo, E.Y. (2009). Use of digital aerophotogrammetry to determine rates of lava dome growth, Mount St. Helens, Washington, 2004-2005. In Sherrod, D.R., Scott, W.E. and Stauffer, P.H. (eds.), *A volcano rekindled: the renewed eruption of Mount St. Helens, 2004-2006* (pp. 145-168). U.S. Geological Survey Professional Paper 2009-1750.

Schneider, D.J., Vallance, J.W., Wessels, R.L. and Logan, M. (2009). Use of thermal infrared imaging for monitoring renewed dome growth at Mount St. Helens, 2004. In Sherrod, D.R., Scott, W.E. and Stauffer, P.H. (eds.), *A volcano rekindled: the renewed eruption of Mount St. Helens, 2004-2006* (pp. 347-360). U.S. Geological Survey Professional Paper 2009-1750.

Scott, W.E., Sherrod, D.R., and Gardner, C.A. (2009). Overview of the 2005 to 2006, and continuing, eruption of Mount St. Helens, Washington. In Sherrod, D.R., Scott, W.E. and Stauffer, P.H. (eds.), *A volcano rekindled: the renewed eruption of Mount St. Helens, 2004-2006* (pp. 3-26). U.S. Geological Survey Professional Paper 2009-1750.

Sparks, R.S.J., Sigurdsson, H., and Wilson, L. (1977). Magma mixing – mechanism for triggering acid explosive eruptions. *Nature, 267,* 315-318.

Taisne, B. and Japuart, C. (2008). Magma degassing and intermittent lava dome growth. *Geophysical Research Letters, 35*, 20,310-20,315.

Tuffen, H., Smith, R., and Sammonds, P.R. (2008). Evidence for seismogenic fracture of silicic magma. *Nature, 453*, 511-514.

Vallance, J.W., Schneider, D.J., and Schilling, S.P. (2009). Growth of the 2004-2006 lava-dome complex at Mount St. Helens, Washington. In Sherrod, D.R., Scott, W.E. and Stauffer, P.H. (eds.), *A volcano rekindled: the renewed eruption of Mount St. Helens, 2004-2006* (pp. 169-208). U.S. Geological Survey Professional Paper 2009-1750.

Vitturi, M.M., Clarke, A.B., Neri, A., and Voight, B. (2008). Effects of conduit geometry on magma ascent dynamics in dome-forming eruptions. *Earth and Planetary Science Letters, 272,* 567-578.

Waite, G.P., Chouet, B.A., and Dawson, P.B. (2008). Eruption dynamics at Mount St. Helens imaged from broadband seismic waveforms: Interaction of the shallow magmatic and hydrothermal systems. *Journal of Geophysical Research, 113,* 2305-2327.

Watts, R.B., Herd, R.A., Sparks, R.S.J., and Young, S.R. (2002). Growth patterns and emplacement of the andesite lava dome at Soufrière Hills Volcano, Montserrat. *Geological Society of London Memoir, 21,* 115–152.

Whitney, J.A. (1988). The origin of granite: the role and source of water in the evolution of granitic magmas. *Geological Society of America Bulletin, 100,* 1886-1897.